THE DEVELOPMENT OF AN EXPERIMENTAL TEST FACILITY TO MEASURE LEAKAGE THROUGH LABYRINTH SEALS

by
Mark A. Rodarte

A thesis submitted in partial fulfillment of
the requirements for the degree of

Master of Science
(Mechanical Engineering)

at the
UNIVERSITY OF WISCONSIN-MADISON
2011

Approved:

Professor Gregory Nellis

Department of Mechanical Engineering

University of Wisconsin – Madison

Doctor Mark Anderson

Department of Nuclear Engineering

University of Wisconsin – Madison

Professor Sanford Klein

Department of Mechanical Engineering

University of Wisconsin – Madison

Abstract

The Supercritical Carbon Dioxide (SCO_2) Brayton has been identified by Dostal (2004) and others to offer significant benefits in terms of efficiency over other cycle alternatives when operating at moderate temperatures. Furthermore, due to the non-ideal gas behavior of CO_2 when operating above the critical point, turbomachinery components can be made smaller and substantially reduce initial plant costs.

An effective design methodology is crucial in the construction of turbomachinery where even the slightest deviations in scale, form, or assembly can substantially limit the peak performance of an overall system. The primary focus of this research is to assess the magnitude of one such drawback identified in the SCO_2 Brayton cycle related to cavity region losses due to shaft seal leakage.

This thesis discusses an experimental test facility that is used to perform leakage measurements through shaft seals subject to upstream conditions in the vicinity of the supercritical point. The test facility has been constructed to limit pressure and density fluctuations during the rapid expansion of a supercritical fluid as it proceeds into the vapor dome. Pressure modulation is governed by a Proportional-Integral (PI) controller back pressure regulation system implemented in LabView. A downstream recovery heating system also implemented with Proportional-Integral (PI) control in LabView allows the recovered two-phase fluid to be cycled back through the system.

Table of Contents

List of Figures

Formatted: Hyperlink, Do not check spelling or grammar

Formatted: Hyperlink, Do not check spelling or grammar

Formatted: Hyperlink, Do not check spelling or grammar

List of Tables

1 Introduction

Power production continues to be a major concern to the longevity of our global prosperity. The current rate of consumption of traditional fossil fuels has placed increased stress on an already overdrawn finite fuel source and economic vitality dictates that both overall plant efficiency as well as net power output must continue to increase while simultaneously minimizing capital expenditures. The concept of maximizing plant output is nothing new. Nonetheless, the supercritical carbon dioxide Brayton (S-CO_2) cycle does exhibit novel characteristics which make it a potential candidate for the next generation power production cycle of choice.

This chapter is divided into four sections. The first section provides a conceptual explanation of how a supercritical fluid differs from a traditional gas- or liquid- phase substance. The second section extends the concepts to a cycle description of the S-CO_2 Brayton cycle and discusses how such a cycle differs from alternative cycle technology. The third section examines some of the more subtle secondary losses related to windage and pumping that are associated with the S-CO_2 cycle that motivate this research. The final section provides a short synopsis of the approach taken in this research.

1.1 Supercritical Fluid Property Variation and Traditional Power Cycles

According to Klein and Nellis (2011) the term “critical point” is defined by the mathematical relationship shown in equation (1.1)

$$\left(\frac{\partial P}{\partial v}\right)_T = 0 \quad \textit{Critical Point} \tag{1.1}$$

where P is pressure, v is specific volume, and T is temperature. The critical point is located on the boundary of the two-phase region at the top of the vapor-dome, as shown in Figure 1.1 for carbon dioxide. At this point, the phase boundary separating liquids and gases vanishes.

A supercritical fluid is a substance whose temperature and pressure lie above the critical point – i.e above the vapor dome in Figure 1.1. The properties in this region are neither that of a liquid nor a gas and exhibit unusual behavior, particularly close to the critical point. Physical properties such as density, specific heat, and viscosity show large gradients in this region. Note the drastic changes in specific volume for modest temperature changes along each isobar in Figure 1.1. Also plotted is a grouping of points that when drawn together is commonly referred to as the pseudocritical line, defined by equation (1.2).

$$\left(\frac{\partial^2 P}{\partial v^2}\right)_T = 0 \qquad \textit{at the Pseudocritical Line} \tag{1.2}$$

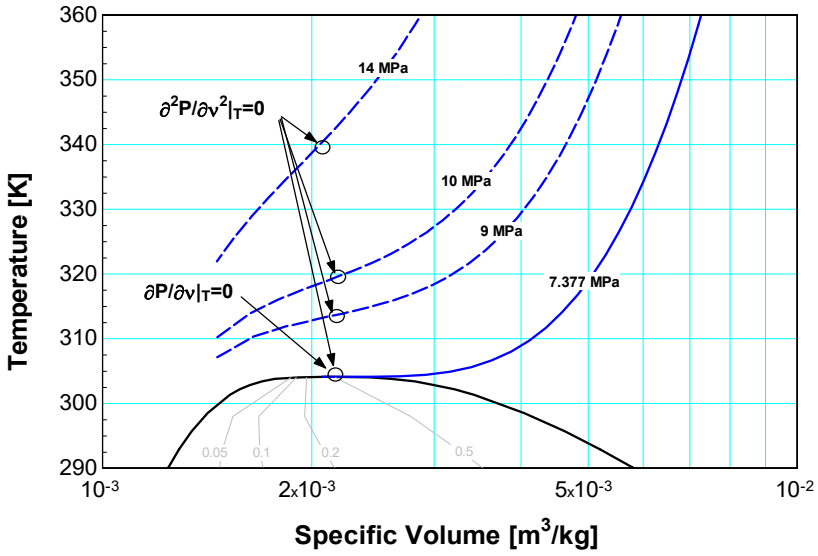

Figure 1.1 Temperature as a function of specific volume for carbon dioxide; the critical point and approximate location of points on the pseudocritical line are shown.

Researchers dating back to Sulzer (1949) have investigated possible uses the observed supercritical property variations for power production. The advantage of using a supercritical fluid in a power cycle is that power output and efficiency may be increased due to the reduced shaft work required in the compression region. An efficient cycle is one in which the compressor input work is low relative to the turbine output work – equation (1.3) defines the back work ratio:

$$BWR = \frac{\dot{W}_{compressor}}{\dot{W}_{turbine}} \tag{1.3}$$

Compressing a low density fluid is disadvantageous as the required compressor work will consume a large portion of the turbine output, thereby decreasing both power output as well as cycle efficiency. In a supercritical Brayton cycle, the compression can occur in the region very close to the critical point which leads to high density fluid and low compressor work.

The Rankine cycle inherently takes advantage of density variations by compressing fluid in the liquid phase to decrease shaft work. The disadvantage of the Rankine cycle, however, is that it requires phase transition through evaporative and condenser stages. This transition requires more support equipment to minimize problems related to cavitation in the compressor region and high inertia droplet impingement during turbine expansion as was noted by Kruizenga (2010).

1.2 The Supercritical Carbon Dioxide Brayton Cycle and Competitors

Three cycles have been identified for near-future power production. The benefits and disadvantages of each cycle are related to the operating conditions where each technology presents distinct engineering challenges. Critical properties for the three cycles are shown in Table 1.1. Note that Helium has a much lower critical point than either of the other working fluids considered but attains high cycle efficiency as a byproduct of the high capacitance rate and multi-staging approximating the ideal cycle.

Table 1-1: Critical Fluid Properties

Fluid	Critical Temperature [C]	Critical Pressure [MPa]
CO_2	30.95	7.377
He	-267.95	0.227
H_20	373.95	22.06

Dostal (2004) notes that the concept of a "supercritical cycle" is rather ambiguous as it encompasses all cycles where the working fluid passes through the supercritical region at one point or another. In this respect, there is a huge difference between the cycles such as the supercritical water cycle (commonly referred to as SCWR) and the S-CO_2 Brayton cycle.

The SCWR cycle is a Rankine cycle where the high pressure side operates above the critical point. The cycle removes the complications related to phase transition on the high pressure side, as noted by Licht (2007). The overall result is an increase in efficiency from roughly 33% in the current nuclear power cycle to 44% according to Licht (2004). In order to achieve this increase in efficiency, the proposed turbine temperature and pressure for this cycle are 500°C and 25 MPa.

The S-CO_2 cycle, in contrast, operates entirely above the critical point of carbon dioxide and therefore avoids phase transition altogether. The major benefit is that the cycle operates entirely above the critical point and the working fluid does not undergo a phase change. Note that the critical temperature is approximately ambient conditions and the critical pressure is significantly lower than that of water. The S-CO_2 cycle was predicted to achieve efficiencies as high as 42%, as was noted by Dostal (2009).

The Helium Brayton cycle, by comparison, achieves efficiencies higher than those of the SCWR and S-CO_2 cycles but requires a much higher turbine inlet temperature (800-900°C), as was noted by Wright (2006). This cycle is a long-term area of research.

The S-CO_2 Brayton cycle is the subject of the current investigation and is illustrated conceptually in Figure 1.2 and Figure 1.3. The states referenced in Figure 1.3 are shown in Figure 1.2.

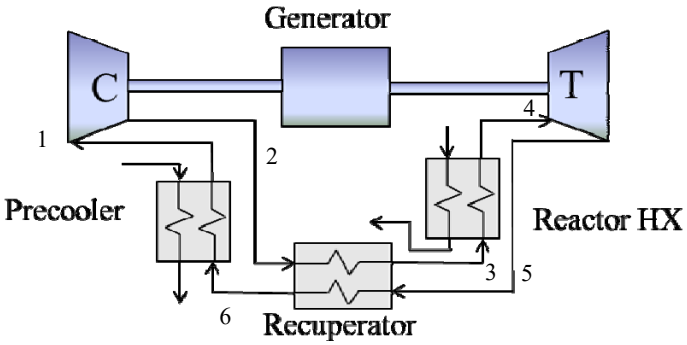

Figure 1.2 Schematic of S-CO_2 Brayton cycle

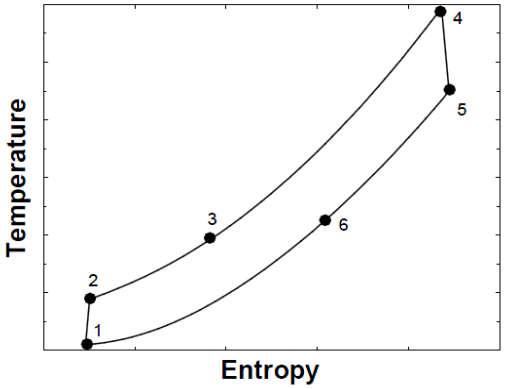

Figure 1.3 Simple diagram of Brayton cycle

1.3 Windage Losses

Proper turbomachinery design is crucial to meeting the performance targets associated with the S-CO_2 Brayton cycle. The objective of the current investigation is to examine the problem of leakage through the shaft seals implemented in the S-CO_2 Brayton cycle. The primary problem is that shaft seals cannot create a hermetic seal about a rotating mechanism across a large pressure gradient. As a result, the working fluid will leak out of the compressor and into the cavity region. Figure 1.4 provides a very simplified diagram of this situation.

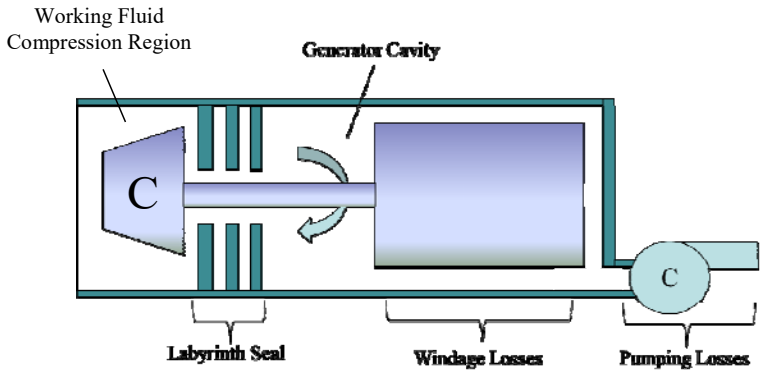

Figure 1.4 S-CO_2 compressor-generator assembly

The primary problem exists in the generator section, where frictional windage losses on the magnetic rotor are highly dependent on density as is shown in equation (1.13). Figure 1.4 shows the primary compressor isolated from the generator cavity by labyrinth seals. Again, labyrinth seals do not provide a perfect seal so, by virtue of the natural pressure gradient from the working

fluid compression region to the generator cavity region, a certain amount of leakage is expected. If the leakage issue is not addressed then the pressure will quickly increase in the generator cavity region to match the pressure in the working fluid compression region. In this situation, the density increases to such levels as to make the windage losses unmanageable.

In an effort to circumvent the windage losses, one idea for decreasing the density in the generator cavity has been to incorporate a secondary system to draw out the residual working fluid from the cavity region. An offsetting performance penalty is related to the pumping losses that have been introduced into the overall system energy balance.

A natural tradeoff exists in this situation, where windage losses are inversely correlated to pumping losses as a function of cavity pressure. Figure 1.5 provides a conceptual interpretation of this idea.

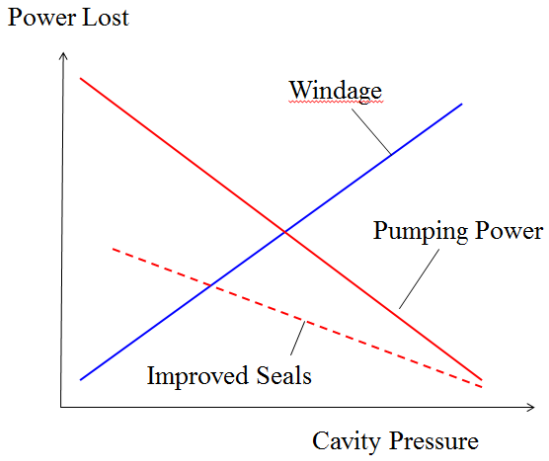

Figure 1.5 Conceptual interpretation of natural tradeoff in system demonstrating the effect of cavity pressure on overall power reduction

Figure 1.6 illustrates the power lost due to windage predicted using the dimensions of the turbine-compressor assembly at Sandia National Laboratories together with the design criteria shown in Table 1-2. Note that windage losses are particularly important to consider in smaller facilities with power input less than 1 MW because the surface area to volume ratio of such machines tends to be high.

Table 1-2 Design values of the turbine-compressor assembly at Sandia National Laboratories used in initial windage loss estimation

Desired Facility Parameters	Variable:	Value:
Thermal power input	W_{in}	390 KW
Electrical power output	W_{out}	150 kW_e
Comp upstream pressure	$P_{upstream}$	13.8 MPa
Rotor Cavity Property	Variable:	Value:
Rotor radius	R_{rotor}	25.4 mm
Rotor length	L_{rotor}	168 mm
Gap thickness	t_{gap}	3.175mm
Rotor speed	ω	75000

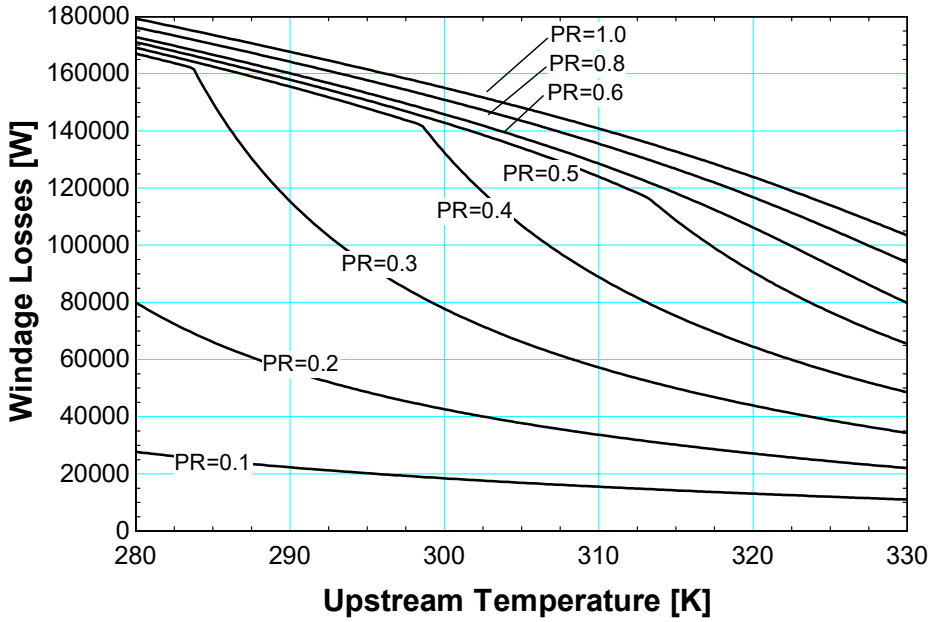

Figure 1.6 Calculated windage losses as a function of inlet temperature at different pressure ratios for the geometry shown in Table 1-2. The pressure ratio relates the cavity pressure to the compressor upstream pressure.

Figure 1.6 shows that the windage losses as a function of upstream temperature based on the design parameters identified in Table 1-2 for the SNL brayton cycle shown in Figure 1.7. The analysis used to construct this graph is discussed below and takes advantage of the Engineering Equation Solver (EES) software package.

The model developed for this analysis allows the user to define the thermodynamic condition directly upstream of the shaft seals as demonstrated by equation (1.4). The specific enthalpy is then calculated from the property database integrated in EES, as shown in equation (1.5).

$$Model\ Upstream\ Inputs:\ P_{upstream}, T_{upstream} \tag{1.4}$$

$$h_{upstream} = Enthalpy\left(Carbon\ Dioxide, P = P_{upstream}, T = T_{upstream}\right) \tag{1.5}$$

A pressure ratio of interest is then selected which can be used to solve for the cavity pressure P_{cavity} as shown in equation (1.6).

$$PR = \frac{P_{cavity}}{P_{upstream}} \tag{1.6}$$

The flow is then assumed to throttle isenthalpically through the shaft seal to a cavity pressure of interest as shown in equation (1.7).

$$h_{cavity} = h_{upstream} \tag{1.7}$$

The density in this "cavity region" is then calculated according to equation (1.8) again using EES integrated property data.

$$\rho_{cavity} = Density\left(Carbon\ Dioxide, P = P_{cavity}, h = h_{cavity}\right) \tag{1.8}$$

The viscosity in the cavity region is calculated in one of two ways. As long as the thermodynamic state is outside the vapor dome, the viscosity is calculated based on equation (1.9).

$$\mu_{cavity} = Viscosity\left(Carbon\ Dioxide, P = P_{cavity}, h = h_{cavity}\right) \tag{1.9}$$

However, if the thermodynamic state lies inside the vapor dome, the following model proposed by Isbin et al. (1958) is used.

$$\mu_{2\phi,cavity} = \left[\frac{x}{\mu_g} + \frac{1-x}{\mu_l}\right]^{-1} \tag{1.10}$$

where x is the quality. The Vrancik (1986) model is traditionally used to estimate windage losses and is shown below as equation (1.13). Also shown is the definition for the skin friction coefficient $C_{d,fric}$ in equation (1.12) for turbulent flow between two parallel plates.

$$\mathrm{Re} = \frac{r_{rotor}\, t_{gap}\, \varpi\, \rho}{\mu} \tag{1.11}$$

$$\frac{1}{\sqrt{C_{d,fric}}} = 2.04 + 1.768 \ln\left(\mathrm{Re}\sqrt{C_{d,fric}}\right) \tag{1.12}$$

$$\dot{W}_{windage} = \pi C_{d,fric} \rho_{cavity} r_{rotor}^4 \varpi^3 L_{rotor} \tag{1.13}$$

In summary, it is clear that the cavity pressure (shown in Figure 1.6 as a function of PR) must be reduced in order to minimize excessive windage losses. With no pressure reduction (i.e., PR =1), the windage loss is on the same order as the output of the cycle.

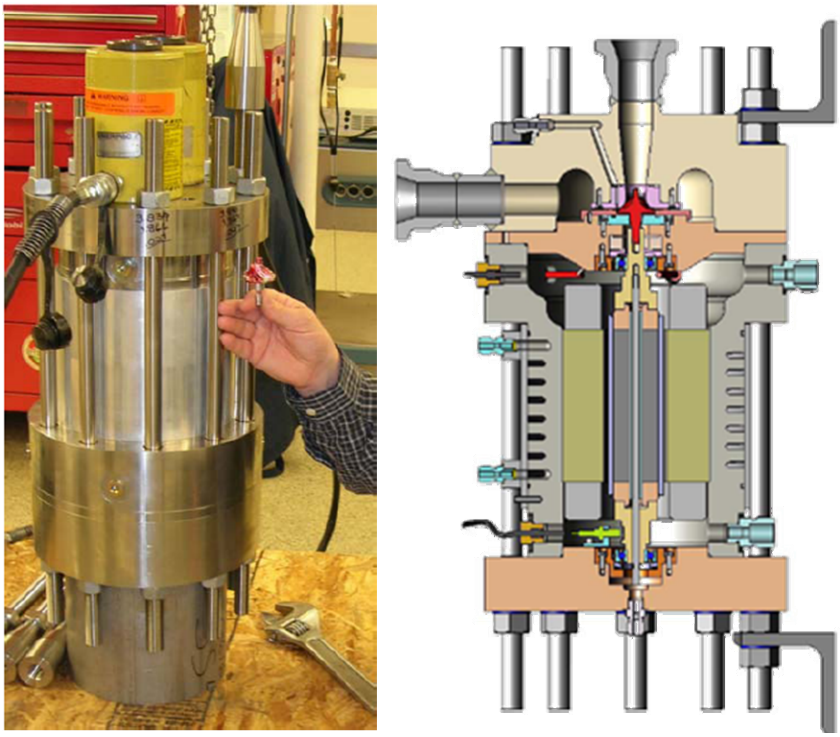

(a) (b)

Figure 1.7 Supercritical carbon dioxide brayton cycle developed by Sandia National Laboratory and Barber-Nichols. (a) Assembled version of S-CO2 cycle (b)

As a point of reference, Figure 1.7 shows the supercritical carbon dioxide brayton cycle at Sandia National Laboratories which corresponds to the physical system discussed in this section. Note the diminutive physical size of the compressor wheel shown in Figure 1.7 for this 150 kW_e output facility.

1.4 Experimental Approach to measuring Seal Leakage

The price for reducing windage loss is pump power. In order to design a system correctly it is necessary to know the pump power and therefore the effectiveness of the seals used to isolate the working fluid from the cavity region. The seals dictate the leakage rate into the cavity region and therefore dictate the pumping power.

The approach taken in the current investigation is to measure the leakage rate through shaft seals driven by large pressure gradients.

Supercritical fluids present an interesting challenge in terms of construction methodology as the sizing of turbomachinery is largely dictated by the operating conditions that are desired. Stability and reliability then becomes a problem as minor deviations in temperature and pressure result in large density and other property variations. The test facility conceived for this investigation is conceptually simple. The thermodynamic state is set directly preceding the test section near the supercritical point. The fluid is then throttled through a reconfigurable shaft seal test section to a desired pressure. The flow rate is measured through the test section.

Operating and control of a flow loop near the critical point is difficult as small changes in temperature result in large changes in density along an isobar. For this reason, the facility employs an active control system of the working fluid in order to regulate the pressure into the test section.

References

Dostal, V., Driscoll, M.J., and Hejzlar, P., 2004, “A Supercritical Carbon Dioxide Cycle for Next Generation Nuclear Reactors”. MIT-ANP-Series, MIT-ANP-TR-100.

Isbin, H.S., Moy, J.E., and DaCruz, J.R., 1958, “Two-phase steam water critical flow”, AICHE Journal, 3, pp. 361-365.

Klein, S.A., Engineering Equation Solver (EES), 1992-2011. ver. 8.957.

Klein, S.A., and Nellis, G.F, 2011, *Thermodynamics,* UW-Madison DoIT bookstore..

Kruizenga, A., 2010, Ph.D. dissertation. “Heat Transfer and Pressure Drop Measurements in Prototypic Heat Exchangers for the Supercritical Carbon Dioxide Brayton Power Cycles”.

Licht, J., Anderson, M., Corradini, M., and Bonazza, R., 2007, “Heat Transfer Phenomena in Supercritical Water Nuclear Reactors”.

Mignot, G., 2007, Ph.D. dissertation. “Critical Flow Experiment and Analysis for Supercritical Fluid”

Vrancik, J.E., “Prediction of windage power loss in alternators”, 1986.

Wright, S.A. Vernon, M.E., Pickard, P.S., 2006, “Concept Design for a High Temperature Helium Brayton Cycle with Interstage Heating and Cooling”, SAND2006-4147.

2 Literature Review: Pressure Drop

The objective of this chapter is to provide an understanding of the pressure drop associated with flows through passages similar to those for labyrinth seals. The pressure drop is an engineering quantity of interest that is readily measured based on the pressure loss between two axial locations. The observed pressure drop is a compilation of the contributing pressure losses that occur along a streamline of a fluid element. In general, the overall pressure drop can be dissected and recast in terms of major pipe flow losses and minor form loss pressure drops, as is denoted in equation (2.1).

$$\Delta P_{total} = \underbrace{\Delta P_{pipe-flow}}_{major\ losses} + \underbrace{\sum_{i}^{n}\left(\Delta P_{flow-disturbances}\right)_{i}}_{form\ losses} \tag{2.1}$$

This chapter is divided into two sections. The first section describes the form losses that occur in pipe flow due to a sudden contraction or expansion of the working fluid. The second section gives a detailed explanation of the major pressure losses that are typical in pipe flow and documents the different models that are available to account for each term.

2.1 Form Losses

Form losses are encountered in any pipe network where anything from pipe-elbows to orifice-plate metering devices will result in a sudden drop in pressure that is driven by a local disturbance of the flow. These form losses are typically referred to as “minor losses”, but in reference to an orifice, nozzle, or flow metering device these losses can be particularly large.

2.1.1 Single Phase One-Dimensional Isentropic Expansion

In the context of shaft seals, the maximum pressure drop associated with a given flow rate is desired. The following analysis is based on the isentropic expansion of a single-phase fluid through an orifice. The model used for this purpose is based on previous work done by Gamal et al. (2006, 2008). This model is based on the St. Venant equations that are used to calculate the isentropic mass flow rate through an orifice based on the pressure difference between the upstream and downstream conditions. The derivation considers one-dimensional effects and applies to inviscid flow of an ideal gas.

Mass and energy balances for the orifice as a control volume are written in equations (2.2) and (2.3).

$$\cancel{\frac{dm}{dt}} = \dot{m}_{in} - \dot{m}_{out} \tag{2.2}$$

$$\dot{m}_{in}\left(h_{in} + \frac{\tilde{V}_{in}^2}{2} + \cancel{g Z_{in}}\right) - \dot{m}_{out}\left(h_{out} + \frac{\tilde{V}_{out}^2}{2} + \cancel{g Z_{out}}\right) + \cancel{\dot{Q}_{cv}} - \cancel{\dot{W}_{cv}} = \cancel{\frac{dU_{cv}}{dt}} \tag{2.3}$$

The system is assumed to be at steady state with negligible change in potential energy. The system also is assumed to be well insulated with no shaft work being done. Equations (2.2) and (2.3) can be combined to result in equation (2.4).

$$h_{in} - h_{out} = \frac{\tilde{V}_{out}^2 - \tilde{V}_{in}^2}{2} \tag{2.4}$$

The process is regarded as internally reversible. Application of the fundamental property relation provides a relationship between the enthalpy difference and the pressure difference, as indicated in equation (2.5).

$$\cancel{T\,ds} = dh - v\,dp \rightarrow dh = v\,dp \rightarrow h_{out} - h_{in} = \int_{P_{in}}^{P_{out}} v\,dp \tag{2.5}$$

By direct substitution of equation (2.5) into (2.4), the following relationship is derived as shown here in equation (2.6).

$$\frac{\tilde{V}_{out}^2 - \tilde{V}_{in}^2}{2} = \int_{P_{out}}^{P_{in}} v\,dp \tag{2.6}$$

The integrand is evaluated by considering the isentropic state equation. The isentropic state equation considers the differential of $p = p(\rho, s)$, shown here as equation (2.7). In an isentropic process, however, the second term drops out of the pressure so that the pressure can be

considered to become a function of density alone. Klein and Nellis (2011) present the following argument.

$$dp = \left(\frac{\partial p}{\partial \rho}\right)_s d\rho + \cancel{\left(\frac{\partial p}{\partial s}\right)_\rho} ds \rightarrow \frac{dp}{d\rho} = \left(\frac{\partial p}{\partial \rho}\right)_s \tag{2.7}$$

The differential specific entropy of a pure fluid is defined by equation (2.8).

$$ds = \frac{du}{T} + \frac{P}{T} dv \tag{2.8}$$

Modifying this equation in terms of the ideal gas law in combination with the specific enthalpy of an ideal gas leads to equation (2.9)

.

$$ds = \frac{C_v\, dT}{T} - \frac{R}{v} dv \tag{2.9}$$

Equation (2.9) can be integrated to obtain equation (2.11).

$$\int_{s_1}^{s_2} ds = \int_{T_1}^{T_2} \frac{C_v(T)}{T} dT + R \int_{v_1}^{v_2} \frac{dv}{v} \tag{2.10}$$

$$s_2 - s_1 = \int_{T_1}^{T_2} \frac{C_v(T)}{T} dT + R \ln\left(\frac{v_2}{v_1}\right) \quad \textit{for an ideal gas} \tag{2.11}$$

For an ideal gas, the appropriate assumption is that $C_v(T)$ is a weak function of temperature and can be taken as a constant $C_v(T) \rightarrow C_v = const$. This recasts equation (2.11) as equation (2.12).

$$s_2 - s_1 = C_v \ln\left(\frac{T_2}{T_1}\right) + R \ln\left(\frac{v_2}{v_1}\right) \quad \textit{for an ideal gas with constant } C_v \tag{2.12}$$

For an ideal gas:

$$C_p - C_v = R \tag{2.13}$$

Substituting the ideal gas law and invoking the specific enthalpy for an ideal gas into equation (2.12) yields (2.14).

$$s_2 - s_1 = C_v \ln\left(\frac{P_2}{P_1}\right) + C_P\left(\frac{v_2}{v_1}\right) \quad \textit{for an ideal gas with constant } C_p \textit{ and } C_v \tag{2.14}$$

For an isentropic process, this leads to the following:

$$C_v \ln\left(\frac{P_2}{P_1}\right) = -C_P \ln\left(\frac{v_2}{v_1}\right) \tag{2.15}$$

The specific heat ratio defined by equation (2.16) is commonly used to model the isentropic expansion of an ideal gas.

$$k = \frac{C_p}{C_v} \tag{2.16}$$

The final form of the expansion of an ideal gas undergoing an isentropic process is presented in equation (2.17).

$$p_{in} v_{in}^k = p\, v^k = const \rightarrow v = \left(\frac{p_{in} v_{in}^k}{p} \right)^{\frac{1}{k}} \tag{2.17}$$

The relationship shown in equation (2.17) is then substituted into equation (2.6) and integrated, as shown in equation (2.18), which results in equation (2.19).

$$\begin{aligned} \frac{\tilde{V}_{out}^2 - \tilde{V}_{in}^2}{2} &= \int_{P_{out}}^{P_{in}} \left(\frac{P_{in} v^k}{p} \right)^{\frac{1}{k}} dp \\ \frac{\tilde{V}_{out}^2 - \tilde{V}_{in}^2}{2} &= \left(\frac{k}{k-1} \right) P_{in}^{\frac{1}{k}} v_{in} \left[p^{\frac{k-1}{k}} \right]_{p_{out}}^{p_{in}} \end{aligned} \tag{2.18}$$

$$\frac{\tilde{V}_{out}^2 - \tilde{V}_{in}^2}{2} = \left(\frac{k}{k-1} \right) P_{in} v_{in} \left[1 - \left(\frac{P_{out}}{P_{in}} \right)^{\frac{k-1}{k}} \right] \tag{2.19}$$

The continuity equation is invoked once again according to equation (2.20) in order to solve for the velocity at the inlet relative to the outlet velocity.

$$\dot{m}_{in} = \dot{m}_{out} \rightarrow \frac{\tilde{V}_{in} A_{c,in}}{v_{in}} = \frac{\tilde{V}_{out} A_{c,out}}{v_{out}}$$
$$\tilde{V}_{in} = \tilde{V}_{out} \left[\frac{A_{c,out}}{A_{c,in}} \right] \left[\frac{v_{in}}{v_{out}} \right] \tag{2.20}$$

The relationship presented in equation (2.17) is then substituted into equation (2.20) to arrive at equation (2.21).

$$\tilde{V}_{in} = \tilde{V}_{out} \left[\frac{A_{c,out}}{A_{c,in}} \right] \left[\frac{v_{in}}{\left(\frac{P_{in} v_{in}^{k}}{P_{out}} \right)^{\frac{1}{k}}} \right] \rightarrow \tilde{V}_{in} = \tilde{V}_{out} \left[\frac{A_{c,out}}{A_{c,in}} \right] \left[\frac{P_{out}}{P_{in}} \right]^{\frac{1}{k}} \tag{2.21}$$

Equation (2.21) is substituted back into equation (2.19) to arrive at (2.22). The result is simplified in terms of $\tilde{V}_{out}$ as shown in equation (2.23). Finally, continuity as presented in equation (2.20) and the isentropic relationship in equation (2.17) are used once again to arrive at equation (2.24).

$$\tilde{V}_{out}^{2} - \left\{ \underbrace{\tilde{V}_{out} \left[\frac{A_{c,out}}{A_{c,in}} \right] \left[\frac{P_{out}}{P_{in}} \right]^{\frac{1}{k}}}_{v_{in}} \right\}^{2} = \left(\frac{2k}{k-1} \right) P_{in} v_{in} \left[1 - \left(\frac{P_{out}}{P_{in}} \right)^{\frac{k-1}{k}} \right] \tag{2.22}$$

$$\tilde{V}_{out}^2 = \frac{\left(\frac{2k}{k-1}\right) P_{in} v_{in} \left[1 - \left(\frac{P_{out}}{P_{in}}\right)^{\frac{k-1}{k}}\right]}{1 - \left\{\left[\frac{A_{c,out}}{A_{c,in}}\right]\left[\frac{P_{out}}{P_{in}}\right]^{\frac{1}{k}}\right\}^2} \tag{2.23}$$

$$\tilde{V}_{out}^2 = \left\{\underbrace{\frac{\dot{m} v_{out}}{A_{c,out}}}_{\tilde{V}_{out}}\right\}^2 \rightarrow \left\{\underbrace{\frac{\dot{m}\overbrace{\left(\frac{P_{in} v_{in}^k}{P_{out}}\right)^{\frac{1}{k}}}^{v_{out}}}{A_{c,out}}}_{\tilde{V}_{out}}\right\}^2 = \frac{\left(\frac{2k}{k-1}\right) P_{in} v_{in} \left[1 - \left(\frac{P_{out}}{P_{in}}\right)^{\frac{k-1}{k}}\right]}{1 - \left\{\left[\frac{A_{c,out}}{A_{c,in}}\right]\left[\frac{P_{out}}{P_{in}}\right]^{\frac{1}{k}}\right\}^2} \tag{2.24}$$

$$\dot{m} = \sqrt{\frac{A_{c,out}^2 \left(\frac{2k}{k-1}\right) P_{in} \left[\frac{P_{out}}{p_{in}}\right]^{\frac{2}{k}} \left[1 - \left(\frac{P_{out}}{P_{in}}\right)^{\frac{k-1}{k}}\right]}{v_{in} \left\{1 - \left\{\left[\frac{A_{c,out}}{A_{c,in}}\right]\left[\frac{P_{out}}{P_{in}}\right]^{\frac{1}{k}}\right\}^2\right\}}}$$

The result is simplified as shown in equation (2.26) where equation (2.25) denotes the mass flux through the constricted cross-sectional area.

$$G = \frac{\dot{m}}{A_{c,out}} \tag{2.25}$$

$$G_{1-D,isentropic,unchoked} = \sqrt{\frac{P_{in}\rho_{in}\left(\frac{2k}{k-1}\right)\left[\left(\frac{P_{out}}{P_{in}}\right)^{\frac{2}{k}} - \left(\frac{P_{out}}{P_{in}}\right)^{\frac{k+1}{k}}\right]}{1-\left\{\left(\frac{A_{c,out}}{A_{c,in}}\right)^{2}\left(\frac{P_{out}}{P_{in}}\right)^{\frac{2}{k}}\right\}}} \tag{2.26}$$

Equation (2.26) is the St. Venant's equation, modified in order to include an area ratio between the inlet channel and the constricted channel cross-sections.

Choking can occur if the velocity reaches the speed of sound. The mass flow rate then becomes independent of the downstream pressure and remains at a fixed value. The definition of the speed of sound is provided in equation (2.27), Moran and Shapiro (2004). Observe that the partial derivative has once again become the total derivative, as shown in equation (2.7).

$$c = \sqrt{-v^2\left(\frac{\partial p}{\partial v}\right)_s} \rightarrow \sqrt{-v^2\left(\frac{dp}{dv}\right)} \tag{2.27}$$

The choked flow condition is obtained by referring back to equation (2.23) and setting the outlet velocity $\tilde{V}_{out}^2 = c^2 = -v^2\left(\frac{dp}{dv}\right)$. The solution is provided by equation (2.28).

$$\tilde{V}_{out}^2 = c^2 \rightarrow \frac{\left(\frac{2k}{k-1}\right) P_{in} v_{in} \left[1 - \left(\frac{P_{out}}{P_{in}}\right)^{\frac{k-1}{k}}\right]}{1 - \left\{\left[\frac{A_{c,out}}{A_{c,in}}\right]\left[\frac{P_{out}}{P_{in}}\right]^{\frac{1}{k}}\right\}^2} = -v_{out,cr}{}^2 \left(\frac{dp}{dv}\right) \tag{2.28}$$

Equation (2.17) is differentiated to solve for $\frac{dp}{dv}$ as presented in equation (2.29).

$$p v^k = P_{in} v_{in}^k \rightarrow p = \frac{P_{in} v_{in}^k}{v^k} \rightarrow \frac{dp}{dv} = -k P_{in} v_{in}{}^k v^{-k-1} \tag{2.29}$$

The end result of equation (2.29) is then substituted into equation (2.28) to solve for the critical downstream pressure. The derivation is presented in equation (2.30) through equation (2.33). Note that the pressure that is determined is the downstream pressure, which corresponds to the downstream specific volume.

$$\underbrace{\frac{\left(\frac{2\cancel{k}}{k-1}\right)\cancel{P_{in}} v_{in}\left[1 - \left(\frac{P_{out,cr}}{P_{in}}\right)^{\frac{k-1}{k}}\right]}{1 - \left\{\left[\frac{A_{c,out}}{A_{c,in}}\right]\left[\frac{P_{out,cr}}{P_{in}}\right]^{\frac{1}{k}}\right\}^2}}_{\hat{V}_{out}^2} = \underbrace{-v_{out,cr}{}^2 \underbrace{\left\{-\cancel{k}\cancel{P_{in}} v_{in}{}^k v_{out,cr}{}^{-k-1}\right\}}_{\frac{dp}{dv}}}_{c^2} \tag{2.30}$$

$$\left(\frac{2}{k-1}\right)\left[1 - \left(\frac{P_{out,cr}}{P_{in}}\right)^{\frac{k-1}{k}}\right] = \frac{v_{in}{}^{k-1}}{v_{out,cr}{}^{k-1}}\left[1 - \left\{\left[\frac{A_{c,out}}{A_{c,in}}\right]\left[\frac{P_{out,cr}}{P_{in}}\right]^{\frac{1}{k}}\right\}^2\right]$$

Invoking equation (2.17) again, the following relationship is derived – shown in equation (2.31).

$$v_{out,cr} = \left(\frac{P_{in} v_{in}^{k}}{P_{out,cr}}\right)^{\frac{1}{k}} : \left(\frac{v_{out,cr}}{v_{in}}\right)^{k} = \left(\frac{P_{in}}{P_{out,cr}}\right) ; \frac{v_{out,cr}}{v_{in}} = \left(\frac{P_{in}}{P_{out,cr}}\right)^{\frac{1}{k}}$$

$$\left(\frac{v_{out,cr}}{v_{in}}\right)^{k-1} = \frac{\left(\frac{P_{in}}{P_{out,cr}}\right)}{\left(\frac{P_{in}}{P_{out,cr}}\right)^{\frac{1}{k}}} = \left(\frac{P_{in}}{P_{out,cr}}\right)^{\frac{k-1}{k}} \tag{2.31}$$

$$\left(\frac{2}{k-1}\right)\left[1-\left(\frac{P_{out,cr}}{P_{in}}\right)^{\frac{k-1}{k}}\right] = \underbrace{\left\{\left(\frac{P_{out,cr}}{P_{in}}\right)^{\frac{k-1}{k}}\right\}}_{\left(\frac{v_{in}}{v_{out,cr}}\right)^{k-1}}\left[1-\left\{\left(\frac{A_{c,out}}{A_{c,in}}\right)\left(\frac{P_{out,cr}}{P_{in}}\right)^{\frac{1}{k}}\right\}^{2}\right] \tag{2.32}$$

$$\left(\frac{P_{out,cr}}{P_{in}}\right)^{\frac{1-k}{k}} + \left(\frac{k-1}{2}\right)\left(\frac{A_{c,out}}{A_{c,in}}\right)\left(\frac{P_{out,cr}}{P_{in}}\right)^{\frac{2}{k}} = \frac{k+1}{2} \tag{2.33}$$

The condition presented here as equation (2.33) is known as the critical pressure ratio at which choked flow occurs for a fixed upstream pressure. It is appropriate to think of this condition as a lower bound domain restriction of the pressure ratio $\frac{P_{out}}{P_{in}}$ for the unchoked flow equation shown here as equation (2.26). For $P_{out,cr} > P_{out}$, the mass flow rate will not increase and it is fixed at the value calculated by equation (2.34).

$$G_{1-D,choked} = \sqrt{\frac{P_{in}\rho_{in}\left(\frac{2k}{k-1}\right)\left[\left(\frac{P_{out,critical}}{P_{in}}\right)^{\frac{2}{k}} - \left(\frac{P_{out,critical}}{P_{in}}\right)^{\frac{k+1}{k}}\right]}{1-\left\{\left(\frac{A_{c,out}}{A_{c,in}}\right)^2\left(\frac{P_{out,critical}}{P_{in}}\right)^{\frac{2}{k}}\right\}}} \tag{2.34}$$

Figure 2.1 demonstrates the effect of pressure ratio *PR*, aspect ratio *AR*, and specific heat ratio *k* on the expansion factor *Y* defined by equation (2.38). The expansion factor shown here is effectively a dimensionless mass flux that relates the mass flux to the inlet thermodynamic state as shown in equation (2.35). The definition of the terms used in equation (2.38) are provided in equations (2.36), (2.37), and (2.16). The mass flux is shown in equation (2.39).

$$Y = \frac{G(PR, AR, k)}{\sqrt{P_{in}\rho_{in}}} \tag{2.35}$$

$$PR = \frac{\max\left(P_{out}, P_{crit}\right)}{P_{in}} \tag{2.36}$$

$$AR = \frac{A_{c,out}}{A_{c,in}} \tag{2.37}$$

$$Y = \sqrt{\frac{\left(\frac{2k}{k-1}\right)\left[(PR)^{\frac{2}{k}} - (PR)^{\frac{k+1}{k}}\right]}{1-\left\{(AR)^2(PR)^{\frac{2}{k}}\right\}}} \tag{2.38}$$

$$G = Y\sqrt{P_{in}\rho_{in}} \tag{2.39}$$

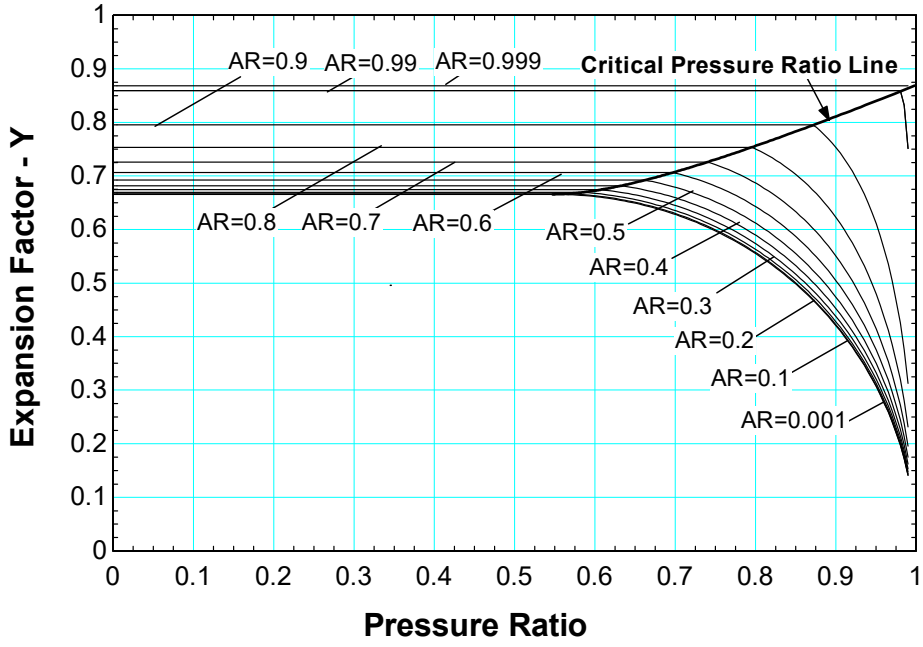

Figure 2.1 Expansion factor Y as a function of pressure ratio for various aspect ratios; also shown is the calculated critical pressure ratio line as defined by equation (2.33); The specific heat ratio was taken to be k=1.292, corresponding to carbon dioxide at 300 K and ideal gas conditions.

Figure 2.1 also shows that a theoretical minimum of the expansion factor exists as $AR \to 0$. The mass flux for *AR* approaching zero is expressed in equation (2.40)

$$G_{1-D,AR\to 0} = \sqrt{P_{in}\,\rho_{in}\left(\frac{2k}{k-1}\right)\left[\left(\frac{P_{out,critical}}{P_{in}}\right)^{\frac{2}{k}} - \left(\frac{P_{out,critical}}{P_{in}}\right)^{\frac{k+1}{k}}\right]} \tag{2.40}$$

The result is the well-known St. Venant's equation for constricted flow where the cross-sectional area of the constriction is much smaller than the inlet channel. Notice that the same result would

have been developed if equation (2.41) was considered instead of (2.4). In the case defined below, the kinetic energy at the inlet is neglected which leads to the result reported in equation (2.40).

$$h_{in} - h_{out} = \frac{\tilde{V}_{out}^2 - \cancel{\tilde{V}_{in}^2}}{2} = \frac{\tilde{V}_{out}^2}{2} \tag{2.41}$$

Also of note, is that with the dependence of the aspect ratio eliminated, the critical pressure ratio becomes a constant as demonstrated in equations (2.42) and (2.43).

$$\begin{gathered}\left(\frac{P_{out,cr}}{P_{in}}\right)^{\frac{1-k}{k}} + \left(\frac{k-1}{2}\right)\cancel{\left(\frac{A_{c,out}}{A_{c,in}}\right)}\left(\frac{P_{out,cr}}{P_{in}}\right)^{\frac{2}{k}} = \frac{k+1}{2} \\ \left(\frac{P_{out,cr}}{P_{in}}\right)^{\frac{1-k}{k}} = \frac{k+1}{2}\end{gathered} \tag{2.42}$$

$$\frac{P_{out,cr}}{P_{in}} = \left(\frac{k+1}{2}\right)^{\frac{k}{1-k}} \tag{2.43}$$

Equation (2.43) is the critical pressure ratio for flow through a constriction where $A_{c,in} >> A_{c,out}$. This well-documented relationship is often substituted for the pressure ratio shown in equation (2.40), resulting in the following relationship for the mass flux as a function of upstream conditions for choked flow conditions.

$$G_{1-D,choked,AR\to 0} = \sqrt{P_{in}\,\rho_{in}\left(\frac{2k}{k-1}\right)\left[\underbrace{\left(\left(\frac{k+1}{2}\right)^{\frac{k}{1-k}}\right)^{\frac{2}{k}}}_{\frac{P_{out,critical}}{P_{in}}} - \underbrace{\left(\left(\frac{k+1}{2}\right)^{\frac{k}{1-k}}\right)^{\frac{k+1}{k}}}_{\frac{P_{out,critical}}{P_{in}}}\right]}$$

$$G_{1-D,choked,AR\to 0} = \sqrt{P_{in}\,\rho_{in}\left(\frac{2k}{k-1}\right)\left(\frac{k+1}{2}\right)^{\frac{2}{1-k}}\left[1-\frac{\left(\frac{k+1}{2}\right)^{\frac{k+1}{1-k}}}{\left(\frac{k+1}{2}\right)^{\frac{2}{1-k}}}\right]}$$

$$G_{1-D,choked,AR\to 0} = \sqrt{P_{in}\,\rho_{in}\left(\frac{2k}{k-1}\right)\left(\frac{k+1}{2}\right)^{\frac{2}{1-k}}\left[1-\frac{1}{\left(\frac{k+1}{2}\right)^{\frac{1-k}{1-k}}}\right]}$$

$$G_{1-D,choked,AR\to 0} = \left(\frac{k+1}{2}\right)^{\frac{1}{1-k}}\sqrt{P_{in}\,\rho_{in}\left(\frac{2k}{\cancel{k-1}}\right)\left[\frac{\cancel{k-1}}{k+1}\right]} \tag{2.44}$$

$$G_{1-D,choked,AR\to 0} = \left(\frac{2}{k+1}\right)^{\frac{1}{k-1}}\sqrt{P_{in}\,\rho_{in}\left(\frac{2k}{k+1}\right)} \tag{2.45}$$

Equation (2.45) shows the critical mass flux as a parameter independent of pressure ratio for $P_{critical,AR\to 0} > P_{out}$.

2.1.2 Conceptual Basis for the Discharge Coefficient

The isentropic relationship derived in section 2.1.1 defines the ideal flow rate through a constricted channel. A reduction in the actual flow rate from this isentropic value will always

occur as irreversible flow components are inherent to any process that occurs in finite time. Furthermore, the flow pattern previously described is strictly for one-dimensional flows. The discharge coefficient, defined by equation (2.46), is often employed as a matter of convenience to relate complicated three-dimensional flow effects to the one-dimensional isentropic relationship shown in section 2.1.1.

$$C_{discharge} = \frac{G_{actual}}{G_{1-D,isentropic}} \tag{2.46}$$

The cumulative effects of geometry and fluid property variations results in a complicated flow pattern through any constricted device. The literature provided in Linfield (2000) shows that the discharge coefficient is a function of the following parameters: wall angle α, inlet-to-constriction ratio AR, orifice shape χ, edge-radius-of-curvature to diameter ratio $\frac{R_{lip}}{d_h}$, gas specific heat ratio k, and pressure ratio PR. Linfield cites Shapiro (1953) to show that the effects of gravity and jet expansion into an infinite medium may be neglected. Finally, Ward-Smith (1979) also documents that the orifice thickness to diameter ratio $\frac{L}{d_h}$ plays a crucial role in causing additional pressure losses beyond the orifice entrance due to Fanno flow. The resulting functional relationship is shown in equation (2.47) where the parameters are demonstrated graphically in Figure 2.2 and Figure 2.3. It is clear based on these parameters that the problem is very difficult to describe analytically and only lends itself to a description in two-dimensions at best. The following analysis considers some of these two dimensional effects.

$$C_d = C_d\left(\alpha, AR, \chi, \frac{R_{lip}}{d_h}, k, PR, \frac{L}{d_h}\right) \tag{2.47}$$

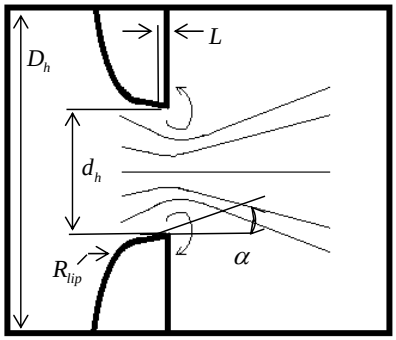

Figure 2.2 Geometrical properties related to critical discharge coefficient

The contraction coefficient is another means of relating the actual flow rate to the ideal flow rate. The definition is provided in equation (2.48) and graphically demonstrated in Figure 2.3.

$$C_c = \frac{A_{vena-contracta}}{A_{constriction}} = \frac{A_{vc}}{A_{c,out}} \tag{2.48}$$

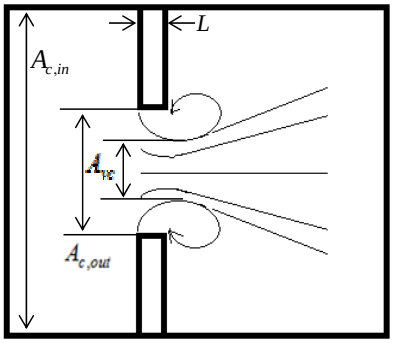

Figure 2.3 Ratio between the cross-sectional areas of the orifice to that of the vena contracta.

Equation (2.48) demonstrates that the flow rate is limited by the cross-sectional area of the vena contracta and not the area of the constriction. This is an important association which establishes that the flow will neck down further than the cross-sectional area of the flow restriction due to two-dimensional lip effects. The problem with this approach is that it is very difficult to measure the hydraulic diameter of the vena contracta. Furthermore, it would be not be in the best interest of the practicing engineer to develop an industry standard based on such a measurement intensive parameter. Nonetheless, the idea does provide a conceptual basis for one-dimensional model developed in Section 2.1.1.

An analytical solution exists for the discharge coefficient associated with a planar, incompressible, inviscid flow through a slot from an infinite reservoir, as defined by equation (2.49) – and shown in Dias (1987). The derivation is based on complex potential flow theory where the flow field is mapped onto the hodographic plane with the variable definitions provided by equation (2.50).

$$C_d\big|_{PR=1} = \frac{1}{1+\int_0^1 \cot\left(\frac{\pi}{2}x\right)\sin(\alpha x)\,dx} \qquad \textit{for a planar slit} \tag{2.49}$$

$$V^2 = u^2 + v^2 \quad ; \quad \theta = \tan^{-1}\left(\frac{v}{u}\right) \qquad \textit{hodographic plane transformation variables} \tag{2.50}$$

Equation (2.49) can be integrated for various wall angles α to determine discharge coefficients for common two-dimensional flow configurations. Note that $\alpha = \frac{\pi}{2}$ corresponds to the classic result $C_d\big|_{PR=1} = \frac{\pi}{\pi+2} \cong 0.611$ or for a Borda-mouthpiece where $\alpha = \pi$ the discharge coefficient is $C_d\big|_{PR=1} = \frac{1}{2}$.

2.1.3 Critical versus Choked Flow

The discharge coefficient is highly dependent on the expansion rate of the medium. Three separate published regimes exist where results have been obtained experimentally and computationally for two-dimensional flows: incompressible, critical, and choked.

The literature confuses the two terms critical flow and choked flow quite often by using them interchangeably. Where it is true that all choked flows can be regarded as critical flows, it is not true that all critical flows are choked flows.

A critical flow results when the velocity of any particle in the flow reaches the sonic condition (i.e. the particle susceptible to the least amount of shear stress) defined by equation (2.27). In contrast, a choked flow results when the bulk of particles in the flow have reached the sonic condition.

$$\begin{aligned} \tilde{V}_{\max} &= c \qquad \textit{critical flow} \\ \tilde{V}_{bulk} &= c \qquad \textit{choked flow} \end{aligned} \tag{2.51}$$

This is a distinct difference that was not considered in the one-dimensional derivation. The solution methodology for the two-dimensional model is quite complicated and only the highlights of a derivation by Linfield (2000) are presented here.

An analytical solution exists to evaluate the onset of choking in two-dimensional planar flow. The result is illustrated in equation (2.52) which shows that one may obtain the choked pressure ratio by only knowing the wall angle α and specific heat ratio k.

$$\begin{aligned} V &= \frac{\alpha}{2} \\ V &= \sqrt{\frac{k+1}{k-1}}\tan^{-1}\left(\sqrt{\left(\frac{k-1}{k+1}\right)\left(M_{choked}^2-1\right)}\right)-\tan^{-1}\left(\sqrt{M_{choked}^2-1}\right) \\ PR_{choked}^{planar} &= \frac{1}{\left(1+\left(\frac{k-1}{2}\right)M_{choked}^2\right)^{\frac{k}{k-1}}} \end{aligned} \tag{2.52}$$

The solution for axisymmetric flow is substantially more involved. However it was noted in Linfield (2000) that Alder (1976) showed that the axisymmetric choked pressure ratio $PR_{choked}^{axisymmetric}$ was only slightly lower than that for planar flow. Linfield quotes $\alpha = 90^{\circ}, PR_{choked}^{planar} = 0.039$ is only slightly decreased to $\alpha = 90^{\circ}, PR_{choked}^{axisymmetric} = 0.035$.

2.1.4 Standard Graph Solution Methodology of Linfield (2000)

Linfield (2000) extended the work of Norwood (1962) and Alder (1976) by numerically evaluating the discharge coefficient for both planar and axisymmetric flows in subsonic and supersonic flow configurations. The subsonic approach is attributed to mathematical relationships developed in Shapiro (1953). Flow in the supersonic regime is solved based on the solutions obtained for the subsonic approach by using them as initial conditions.

Linfield (2000) constructed a semi-empirical model called the *Standard Graph* to evaluate the discharge coefficient based on planar flow. The model uses a combination of analytical, computational, and experimental results to construct a flow map of the discharge coefficient as a function of the specific heat ratio, pressure ratio, and wall angle for flow through a planar duct.

The *Standard Graph* approach relies heavily on the analytical solution for a planar slit provided by equation (2.49). The assumptions employed in the construction of the *Standard Graph* are detailed in equation (2.53).

$$C_d = C_d\left(\alpha, AR = 0, \chi = planar, \frac{R_{lip}}{d_h} = 0, k, PR, \frac{L}{d_h} \to 0\right) \tag{2.53}$$

The model discerns that, if the discharge coefficient can be obtained at the incompressible limit where $PR \to 1$, a flow map can be constructed for all subsequent pressure ratios based on empirically fit equations for the information shown in equation (2.54).

$$\begin{aligned} C_d\big|_{PR=1} &= f(\alpha,k); \qquad \left.\frac{\partial C_d}{\partial PR}\right|_{PR=1} = f(\alpha,k) \\ C_d\big|_{PR=PR_{critical}} &= f(\alpha,k) \quad \left.\frac{\partial C_d}{\partial PR}\right|_{PR=PR_{critical}} = f(\alpha,k) \\ C_d\big|_{PR=PR_{choked}} &= f(\alpha,k) \quad \left.\frac{\partial C_d}{\partial PR}\right|_{PR=PR_{choked}} = f(\alpha,k) \end{aligned} \tag{2.54}$$

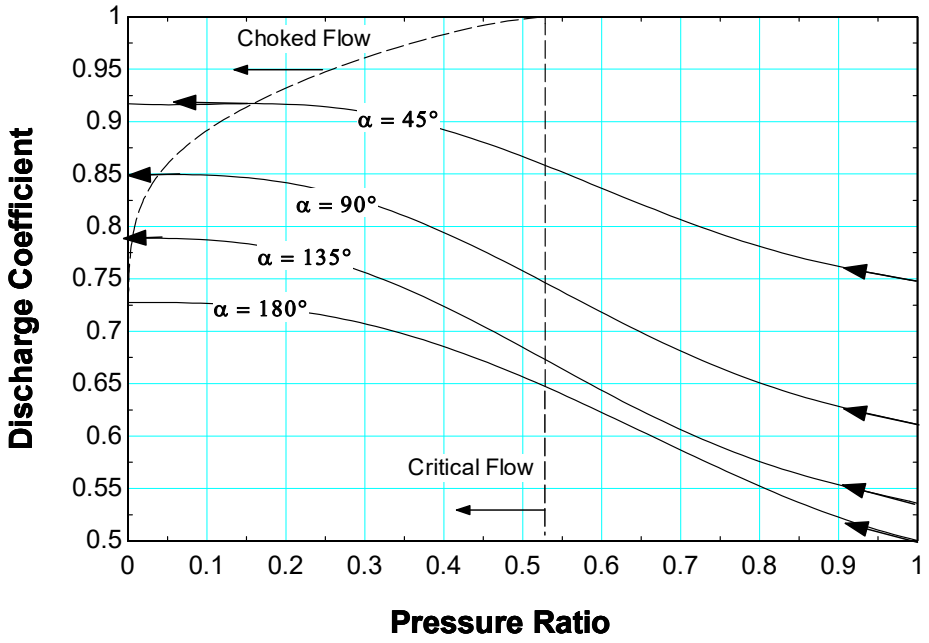

Figure 2.4 Standard Graph flow map methodology attributed to Linfield (2000). Graph depicts the discharge coefficient for an ideal gas with aspect ratio AR=0, specific heat ratio k=1.4, and wall angle α

Figure 2.4 is an illustration of the *Standard Graph* approach where the discharge coefficient is illustrated as a function of pressure ratio *PR* and wall angle α. The arrows shown in Figure 2.4 locate the point and the derivative of the information required. Linfield has documented functions for all equations shown in (2.54) so that implementation of the *Standard Graph* approach is rather simple.

2.1.4.1 Curve-fits used to construct Standard Graph

Discharge Coefficient for Incompressible Flow at PR=1

The relationship presented in equation (2.55) shows that the discharge coefficient for an incompressible substance through a planar geometry at pressure ratios approximately equal to unity can adequately be defined strictly on the wall angle α. The slope of the line then deviates from that point according to equation (2.57) based on the argument presented in Buseman (1937) as summarized by Linfield (2000) – shown here as equation (2.56).

$$C_d\big|_{PR=1} \approx \frac{1}{1+\sqrt{1-\left(\frac{\sin\alpha}{\alpha}\right)^{1.15}}} \tag{2.55}$$

$$C_d\Big|_{PR\approx 1}^{90^\circ} = \frac{1}{1+\frac{2}{\pi}\frac{\rho_{jet}}{\rho_o}} \cong \frac{1}{1+\frac{\rho_{jet}}{\rho_o}\sqrt{1-\left(\frac{\sin\alpha}{\alpha}\right)^{1.15}}} \tag{2.56}$$

$$\left.\frac{\partial C_d}{\partial PR}\right|_{PR=1} = \frac{-\sqrt{1-\left(\frac{\sin\alpha}{\alpha}\right)^{1.15}}}{k\left(1+\sqrt{1-\left(\frac{\sin\alpha}{\alpha}\right)^{1.15}}\right)^2} = -\frac{C_d\big|_{PR=1}\left(1-C_d\big|_{PR=1}\right)}{k} \tag{2.57}$$

Figure 2.5 shows the discharge coefficient as a function of wall angle α through a planar slit. The exact solution provided by equation (2.49) is shown to confirm the approximate solution provided by equation (2.55).

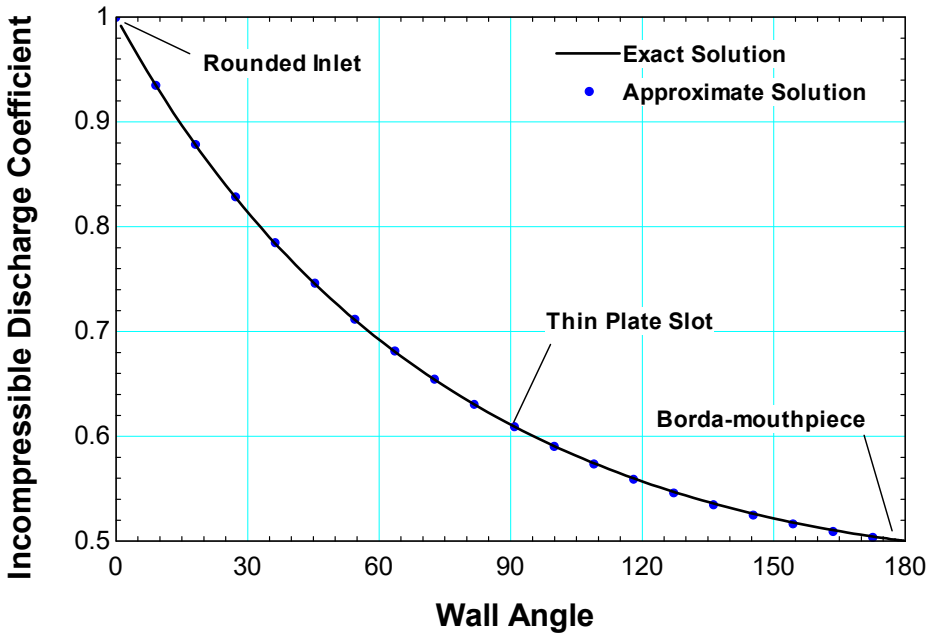

Figure 2.5 Discharge coefficient for *PR=1* as a function of wall angle α for planar flow; basis for Standard Graph approach, k=1.4

The discharge coefficient for an incompressible substance is the same at pressure ratios close to unity and is strictly a function of wall angle. The deviation in discharge coefficient from that point then changes according to the specific heat ratio k .

Discharge Coefficient at Critical Pressure Ratio

The critical pressure ratio was defined in equation (2.33). Linfield (2000) documents the following curve-fit relationships at this limit.

$$
\begin{aligned}
&C_d\big|_{PR=PR_{critical}} = A(\bar{\alpha}) + k\,B(\bar{\alpha}) \\
&A = 1 - 0.5103\bar{\alpha} + 0.05644\bar{\alpha}^2 + 0.1360\bar{\alpha}^3 \\
&B = -0.07373\bar{\alpha} + 0.07731\bar{\alpha}^2 - 0.02848\bar{\alpha}^3
\end{aligned}
\tag{2.58}
$$

$$
\begin{aligned}
&\left.\frac{\partial C_d}{\partial PR}\right|_{PR=PR_{critical}} = \frac{\bar{\alpha}}{C(k) + \bar{\alpha}D(k)} \\
&C = 0.1549 - 0.01177\,k \\
&D = 0.934 + 0.6433\,k
\end{aligned}
\tag{2.59}
$$

Note that $\bar{\alpha}$ is a non-dimensional wall angle defined by equation (2.60) and the specific heat ratio k was defined in equation (2.16).

$$
\bar{\alpha} = \frac{\alpha}{\pi} \tag{2.60}
$$

Discharge Coefficient for Choked Flow

The following curve-fit relationships from Linfield (2000) apply to the development of the standard discharge coefficient graph in the choked flow regime. The coefficients shown in equation (2.61) are slightly different from those published in Linfield (2000). Furthermore, the sign of the second term has been modified such that $C_d = f(E, -kF)$ instead of $C_d = f(E, kF)$ in order to be consistent with the graphs actually presented in Linfield (2000).

$$
\begin{aligned}
&C_d\big|_{PR=PR_{choked}} = E(\bar{\alpha}) - k\,F(\bar{\alpha}) \\
&E = 1 - 0.3052\bar{\alpha} + 0.1322\bar{\alpha}^2 \\
&F = 0.0483\bar{\alpha} - 0.04124\bar{\alpha}^2 + 0.06505\bar{\alpha}^3
\end{aligned}
\tag{2.61}
$$

$$
\left.\frac{\partial C_d}{\partial PR}\right|_{PR=PR_{choked}} = 0 \rightarrow C_d\big|_{PR<PR_{choked}} = C_d\big|_{PR\rightarrow 0} \tag{2.62}
$$

$\bar{\alpha}$ is defined in equation (2.60).

2.1.4.2 Standard Graph Equivalent Discharge Coefficient Procedure

Linfield (2000) stipulates that the *Standard Graph* discharge coefficient approach developed in the previous section should apply to other constrictive devices with different wall angles α, inlet-to-constriction ratios AR, orifice shapes χ, and edge-radius-of-curvature to diameter ratios $\frac{R_{lip}}{d_h}$ provided that the discharge coefficient for the prototype device when evaluated in the incompressible limit shares a comparable discharge coefficient with those supported by the *Standard Graph*. The idea is expressed in equation (2.63) and illustrated in

$$
C_d\big|_{PR=1}^{prototype}\left(\alpha, AR \geq 0, \chi = \begin{matrix} planar \\ axisymmetric \\ other \end{matrix}, \frac{R_{tip}}{d_h} > 0, k\right) := C_d(\alpha)\Big|_{PR=1}^{standard\ graph} \quad desired \tag{2.63}
$$

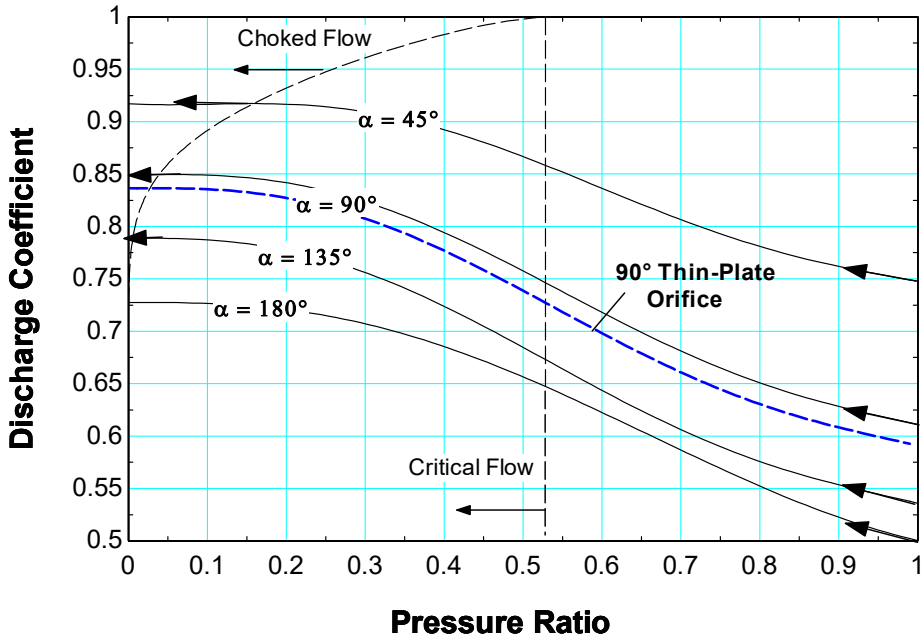

Figure 2.6 Conceptual basis for Standard Graph approach. The trend of the discharge coefficient of the prototype is estimated to be approximately equal to that of a planar element evaluated at a particular wall angle α, k=1.4

The concept of the *Standard Graph* approach dictates that the incompressible flow limit $C_d\big|_{PR=1}$ of the prototype must be known. Once this reference is known, the value of $C_d\big|_{PR=1}$ is input into equation (2.64) – which is a restatement of equation (2.55) – to solve for the wall angle $\alpha'_{standard\ graph}$. This procedure will effectively translate the prototypical orifice into a standard planar constriction evaluated at some arbitrary wall angle. The distribution of the planar constriction based on this effective wall angle is now the distribution of the adjusted prototype as demonstrated in the final iteration of the procedure outlined in equation (2.65).

$$\frac{\sin\alpha'_{standard\ graph}}{\alpha'_{standard\ graph}} \approx \left[1-\left(\frac{1}{C_d\big|_{PR=1}}-1\right)^2\right]^{\frac{1}{1.15}} \tag{2.64}$$

$$C_d\big|_{PR=1}^{prototype}\left(\alpha_{prototype}, AR\geq 0, \chi = \begin{matrix} planar \\ axisymmetric \\ other \end{matrix}, \frac{R_{tip}}{d_h}\geq 0, k\right) \qquad known$$

$$C'_d\big|_{PR=1}^{prototype}\left(\alpha_{prototype}, AR=0, \chi = planar, \frac{R_{tip}}{d_h}=0, k\right) = f\left(C_d\big|_{PR=1}^{prototype}\right) \qquad determined$$

$$C'_d\big|_{PR=1}^{prototype} \rightarrow \frac{\sin\alpha'_{standard\ graph}}{\alpha'_{standard\ graph}} \approx \left[1-\left(\frac{1}{C'_d\big|_{PR=1}^{prototype}}-1\right)^2\right]^{\frac{1}{1.15}} \rightarrow \alpha'_{standard\ graph} \quad solve\ \alpha'_{standard\ graph} \tag{2.65}$$

$$C'_d\big|_{PR=1}^{prototype} = C_d\big|_{PR=1}^{standard\ graph}\left(\alpha'_{standard\ graph}\right) \qquad translation\ achieved$$

$$C'_d\Big|^{prototype} = C_d\Big|^{standard\ graph}\left(\alpha'_{standard\ graph}\right)$$

Two major issues exist with this approach. The first issue is the prototype mapping dependence on $C_d\big|_{PR=1}^{prototype}$ which must be measured or approximated by some method. The second major issue is determining the value of the variable $C'_d\big|_{PR=1}^{prototype}$ once $C_d\big|_{PR=1}^{prototype}$ is known. Fortunately a few ideas have been developed and will be explained in the following sections. Also shown are published results for $C_d\big|_{PR=1}^{axisymmetric}$ shown in Linfield (2000) and restated here as Table 2-1 through Table 2-3.

Table 2-1 Published values of $C_d|_{PR=1}$ for a 90° slot and conical orifice with an aspect ratio $AR = 0$.

Author	Year	$C_d\|_{PR=1}^{planar}$	$C_d\|_{PR=1}^{axisymmetric}$
Analytical Solution		0.6110154…	
Rouse & Abul-Fetouh	1950		0.612
Garabedian	1956		0.579
Hunt	1967		0.578
Bloch	1969		$0.59131 \le C_d \le 0.59139$
Alder	1976	0.611	0.591
Pickett	1989	0.61101564	
Linfield	2000	0.61102	0.59137

Table 2-2 Published values of $C_d|_{PR=PR_{crit}}$ for a 90° slot and conical orifice with an aspect ratio $AR = 0$ and $k = 7/5$.

Author	Year	$C_d\|_{PR=PR_{crit}}^{planar}$	$C_d\|_{PR=PR_{crit}}^{axisymmetric}$
Chaplygin	1902	0.74	
Norwood	1962	0.745	
Alder	1976	0.745	0.726
Kosolapov & Sivoborod	1984	0.76	
Pickett	1989	0.744559129	
Linfield	2000	0.74456	0.72606

Table 2-3 Published values of $C_d|_{PR=PR_{choked}}$ for a 90° slot and conical orifice with an aspect ratio $AR = 0$ and $k = 7/5$. Note: ( )[1] notes values were obtained from reading a graph by Linfield.

Author	Year	$C_d\|_{PR=PR_{choked}}^{planar}$	$C_d\|_{PR=PR_{choked}}^{axisymmetric}$
Frankl	1947	0.85	
Norwood	1962	0.850	
Benson & Pool	1965	0.853	
Fenain et al	1974		0.837[1]
Alder	1976	0.849	0.830
Filippov et al	1982	0.842	0.819[1]
Kosolapov & Sivoborod	1984	0.85	0.832
Linfield	2000	0.84925	0.83083

2.1.4.3 Discharge Coefficient for Axisymmetric Flow

The discharge coefficient for incompressible axisymmetric flow through a circular orifice is explicitly stated as a function of the wall angle α in equation (2.66). Stated differently, the aspect ratio $AR = 0$ and the pressure ratio $PR = 1$.

$$C_d\big|_{PR=1}^{axisymmetric} = \frac{1}{1+\sqrt{1-\left[\frac{\sin^2\alpha}{2(1-\cos\alpha)}\right]^{\beta}}} \tag{2.66}$$

Linfield (2000) modified the β term from the exact solution of β=2 to β=0.94 to match the numerical value he obtained for a thin plate orifice $C_d\big|_{PR=1}^{\alpha=90^\circ} \approx 0.591$. The output from equation (2.66) is compared to the discharge coefficient obtained for incompressible flow through a planar flow restriction in Figure 2.7. The trends are very similar and the solutions reproduce the classic solutions of $C_d\left(\alpha = 0^\circ\right) = 1$ and $C_d\left(\alpha = 180^\circ\right) = \frac{1}{2}$ respectively. Notice that the incompressible discharge coefficient through a circular orifice is shown to be only slightly lower than the planar flow counterpart.

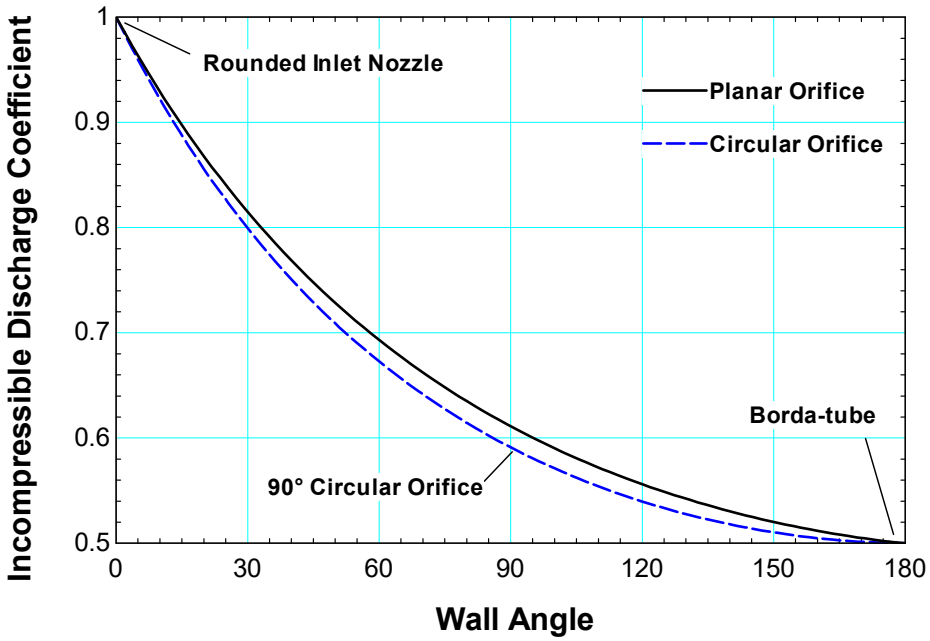

Figure 2.7 Discharge coefficient for *PR=1* as a function of wall angle α for planar flow and axisymmetric flow, k=1.4

2.1.4.4 Conical Orifices with Edge Rounding

Smoothing of the inlet flow pattern can also take place if the lip geometry is sufficiently rounded so that the flow remains attached to the wall of the orifice during the expansion process. The idea is to virtually eliminate any deviation between the area of the orifice and that of the vena contracta by retarding separation of the boundary layer. This is effectively why a long-radius nozzle such as the ISA 1932 referenced in White (2008) maintains a discharge coefficient near unity.

Edge rounding of the inlet lip is accommodated in the *Standard Graph* approach by solving equations (2.67) through (2.69) for the effective wall angle $\hat{\alpha}$. Once this value is obtained, the effective wall angle is used in equation (2.66) to locate the approximate incompressible discharge coefficient to be used in the *Standard Graph* approach.

$$\hat{\alpha} = \max\left(\alpha - \Delta\alpha, 0\right) \tag{2.67}$$

$$\Delta\alpha = A(\alpha)\ln\left[\left(\frac{R_{lip}}{d_h}\, x1000\right)^2 + 1\right] \tag{2.68}$$

$$A = 0.04626\alpha + 0.01163\alpha^2 \tag{2.69}$$

A combination of curve-fits and limiting restraints were used to construct the empirical relationships provided above. The two limits imposed on the empirical relationship are shown here in equation (2.70).

$$\begin{aligned} &C_d\left(\alpha\right)\Big|_{\frac{R_{lip}}{d_h}\to 0} = C_d\left(\alpha\right) \\ &C_d\Big|_{\frac{R_{lip}}{d_h}\geq 0.82} \approx 0.99 \end{aligned} \tag{2.70}$$

Note that an “ideal” sharp lip orifice is a non-physical object; there will always be blunting of the inlet lip as a result of any manufacturing process. For this reason, flow separation will always occurs slightly aft of the leading edge of the orifice. To a working approximation, the

International Standards Organization (ISO, 1980) had defined a sharp lip for an orifice flow meter based on equation (2.71).

$$\frac{R_{lip}}{d_h} \leq 0.0004 \tag{2.71}$$

The other limit discerned from equation (2.70) can be justified based on the listed ASME standard (1961) referenced by Linfield (2000) which stipulates that for all practical working approximations the discharge coefficient is approximately unity for rounded inlets where $\frac{R_{lip}}{d_h} \geq 0.82$. The model seems to under predict the discharge coefficient in this limit as is illustrated in Figure 2.8 where $\frac{R_{lip}}{d_h} \geq 10$ seems to predict discharge coefficients closer to unity.

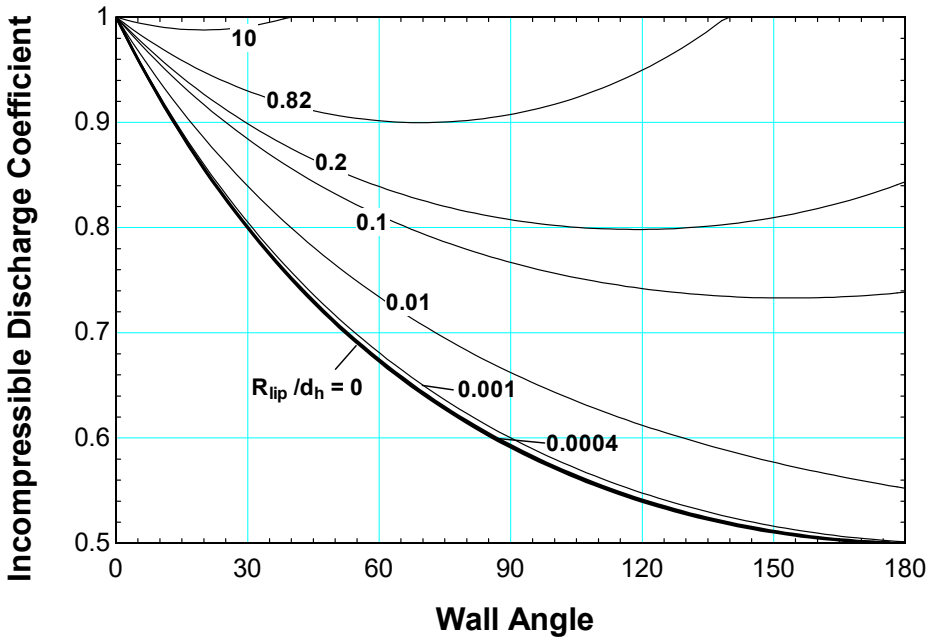

Figure 2.8 Discharge coefficient for *PR=1* as a function of wall angle α for flow through a restriction with different ratios of the lip radius to the diameter of the orifice, k=1.4

2.2 Major Pipe Losses which occur during Reattachment

Just as one could visualize the total pressure drop in a system as a compilation of major and minor losses, one could also break the problem down further by recasting the 'major losses' term in proportion to its constituents. This situation leads to equation (2.72) which states that an axial flow subject to major losses alone (i.e. no form losses) will still incur a pressure loss due to frictional, accelerant, and gravitational effects.

$$\underbrace{\Delta P_{pipe-flow}}_{major\ losses} = \Delta P_{frict} + \Delta P_{accel} + \Delta P_{grav} \tag{2.72}$$

This section is primarily concerned with losses related to friction and flow development which occurs after the sudden expansion form loss detailed in Section 2.1.

Ward-Smith (1984) details that a relationship exists between the critical discharge coefficient C_d and orifice length to orifice diameter $\frac{L}{D_h}$. In particular, he illustrates that the functional relationship illustrated in Figure 2.9 applies to circular orifices with $\frac{L}{D_h}$ ratios in the range shown.

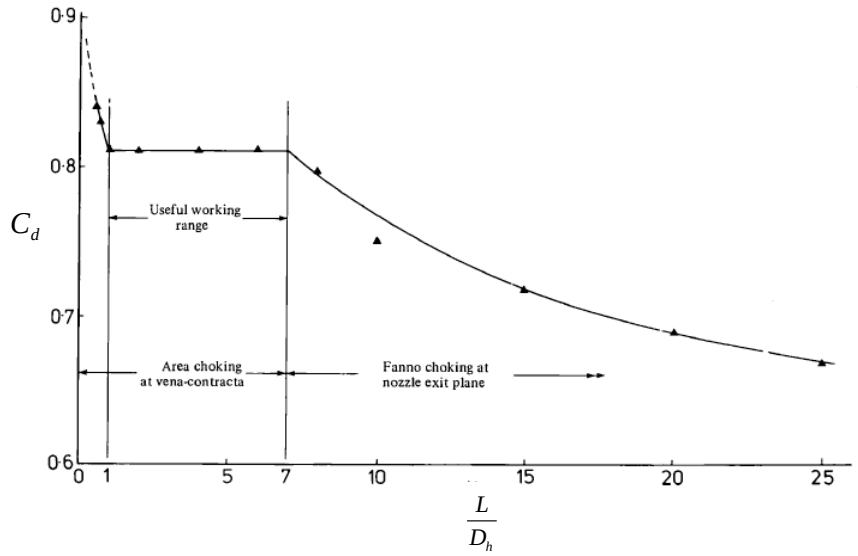

Figure 2.9 Functional relationship between discharge coefficient and the ratio of the orifice length to the orifice diameter. Reproduced from Ward-Smith (1979).

The following sections detail specific methods for estimating the frictional and accelerant pressure drops which occur aft of the orifice inlet.

2.2.1 Frictional Pressure Drop

Laminar Flow

The following discussion is a compilation of the information provided in Nellis and Klein (2009) and White (2008). The primary focus is to address the frictional pressure drop in the wake of the form loss step change in pressure addressed in Section 2.1.

Analytical solutions for laminar flow in a duct subject to friction have been obtained for various geometrical conditions. Laminar flow is especially susceptible to deviations in geometrical conditions so it stands to reason that exact solutions in this regime need to take into consideration all geometrical boundaries present in the duct of interest.

Nellis and Klein (2009) have published the exact solutions for hydrodynamically fully developed flow through a circular duct as shown in equation (2.73), flow through a concentric annulus in equation (2.74), and finally flow through two parallel plates in equation (2.75). Note that as the aspect ratio *RR* in equation (2.74) approaches 0 or 1, the equation naturally simplifies to flow through a cylinder and flow through two parallel plates respectively.

$$f_{fd,h} = \frac{64}{\mathrm{Re}_{D_h}} \tag{2.73}$$

$$f_{fd,h} = \frac{64}{\mathrm{Re}_{D_h}} \sqrt{\frac{(1-RR)^2}{1+RR^2-\left(\frac{1-RR^2}{\ln\left(RR^{-1}\right)}\right)}} \tag{2.74}$$

$$RR = \frac{R_{inner}}{R_{outer}}$$

$$f_{fd,h} = \frac{96}{\mathrm{Re}_{D_h}} \tag{2.75}$$

The average friction factor for laminar flow which includes entrance effects is given by Shah and London (1978) as was published in Nellis and Klein (2009). The formula is exact for a circular tube where $f_{fd,h}\,\mathrm{Re}_{D_h} = 64$ but was shown in Nellis and Klein (2009) to perform well under other geometrical conditions. The dimensionless length L^+ for hydrodynamically developing internal flow is reproduced here in equation (2.77).

$$\overline{f} \approx \frac{4}{\mathrm{Re}_{D_h}}\left[\frac{3.44}{\sqrt{L^+}} + \frac{\frac{1.25}{4L^+} + \frac{\overbrace{\left(f_{fd,h}\,\mathrm{Re}_{D_h}\right)}^{duct\ shape\ dependence}}{4} - \frac{3.44}{\sqrt{L^+}}}{1+\frac{0.00021}{\left(L^+\right)^2}}\right] \tag{2.76}$$

$$L^+ = \frac{L}{D_h\,\mathrm{Re}_{D_h}} \tag{2.77}$$

Turbulent Flow

Turbulent flow is effectively insensitive to duct shape but highly dependent on surface roughness. In this regime, kinetic energy is dissipated along the duct's wall via the viscous sublayer which can be on the order of the wall roughness if the material is course enough. The standard approach is to use either the Blasius (1911) solution shown in equation (2.78) if the walls are "smooth" or use the Colebrook (1939) solution presented in equation (2.79). Other explicit turbulent friction factor equations have been proposed throughout the years such as the one for multi-phase flow proposed by Churchill (1977) shown in equation (2.80). All of these equations are based on the Darcy friction factor definition.

$$\textit{Blasius}\,(1911) \qquad f_{fd,h,e=0} = \frac{0.316}{\mathrm{Re}_{D_h}^{0.25}} \qquad 4000 < \mathrm{Re}_{D_h} < 10^5 \qquad (2.78)$$

$$\textit{Colebrook}\,(1939) \qquad \frac{1}{\sqrt{f_{fd,h}}} = 3.48 - 1.7373 \ln\left(\frac{2e}{D_h} + \frac{9.35}{\mathrm{Re}_{D_h}\sqrt{f_{fd,h}}}\right) \qquad (2.79)$$

$$\textit{Churchill}\,(1977)\ f_{2\phi,fd,h} = 8\left\{\left(\frac{8}{\mathrm{Re}}\right)^{12} + \left(\left[2.457\ln\left(\frac{1}{\left(\frac{7}{\mathrm{Re}}\right)^{0.9} + 0.27\left(\frac{e}{D_h}\right)}\right)\right]^{16} + \left(\frac{37530}{\mathrm{Re}}\right)^{16}\right)^{-1.5}\right\}^{\frac{1}{12}} \qquad (2.80)$$

The friction factor is used to compute the pressure drop according to equation (2.81) for a single phase fluid.

$$f = \tau_s \frac{8}{\rho U_m^2} = -\frac{dP}{dx}\frac{2D_h}{\rho U_m^2} \tag{2.81}$$

A number of models exist to compute the pressure drop for a two-phase fluid. The empirical model proposed by Müller-Steinhagen and Heck (1986) shown here as equations (2.82) through (2.87) was shown in Ould Didi et al. (2002) to provides excellent agreement with experimental data across a number of different two-phase flow regimes.

$$\left.\frac{dP}{dz}\right|_{fric,2\phi} = \Lambda\left(1-x\right)^{\frac{1}{3}} + \left.\frac{dP}{dz}\right|_{go} x^3 \tag{2.82}$$

$$\Lambda = \left.\frac{dP}{dz}\right|_{lo} + 2\left(\left.\frac{dP}{dz}\right|_{go} - \left.\frac{dP}{dz}\right|_{lo}\right)x \tag{2.83}$$

$$\left.\frac{dP}{dz}\right|_{lo} = f_l \frac{2G^2}{D_h \rho_l} \tag{2.84}$$

$$\left.\frac{dP}{dz}\right|_{go} = f_g \frac{2G^2}{D_h \rho_g} \tag{2.85}$$

$$f_{MSH,\phi} = f_\phi\left(e, \mathrm{Re}_{D_h}\right) \tag{2.86}$$

$$f_{MSH,\phi:\,fd,h,e=0} = \underbrace{\frac{0.079}{\mathrm{Re}_\phi^{0.25}}}_{\substack{\text{Correlation based on} \\ \text{Fanning friction factor}}} \tag{2.87}$$

The subscripts *l* and *g* denoted in the model stand for liquid and gas phase constituents respectively. *G* refers to the mass flux through the test section defined by equation (2.88) and the Reynolds' number Re_ϕ can be calculated for each phase based on equation (2.89).

$$G = \frac{\dot{m}}{A_c} \tag{2.88}$$

$$\mathrm{Re}_{D_h,\phi} = \frac{GD_h}{\mu_\phi} \tag{2.89}$$

Note that the friction factors used in equations (2.84) and (2.85) refer to the Fanning friction factor and not the Darcy friction factor obtained from equations (2.73) through (2.80). This concept is readily identified by comparing equations (2.87) and (2.78). As such, any friction factor calculated by the Colebrook equation or Churchill equation should be divided by a factor of 4 in order to use in equations (2.84) and (2.85). The conversion is appropriately shown in equation (2.90).

$$\underbrace{f_{MSH,\phi}}_{\substack{\text{Correlation based on} \\ \text{Fanning friction factor}}} = \underbrace{\frac{f_{Colebrook}\,;\, f_{Churchill}}{4}}_{\substack{\text{Correlation based on} \\ \text{Darcy friction factor}}} \tag{2.90}$$

The average turbulent flow friction factor which includes entrance effects as shown in Nellis and Klein (2009) is reproduced here as equation (2.91).

$$\overline{f} = f_{fd,h}\left(1+\left(\frac{D_h}{L}\right)^{0.7}\right) \tag{2.91}$$

2.2.2 Acceleration Pressure Drop

The following discussion pertains to density driven pressure drops due to acceleration of the flow. The general equation for this type of pressure loss is provided in (2.92).

$$\Delta P_{accel} = G^2 \left[\frac{1}{\rho_{out}} - \frac{1}{\rho_{in}} \right] \tag{2.92}$$

Single phase flows are not generally sensitive to this type of pressure loss. Two-phase flows are more vulnerable to this type of pressure loss and may be modeled using the density information provided in EES as well as the aforementioned equation attributed to Isbin et al. (1958) originally defined in equation (1.10) but reproduced here as equation (2.93).

$$\mu_{2\phi,cavity} = \left[\frac{x}{\mu_g} + \frac{1-x}{\mu_l} \right]^{-1} \tag{2.93}$$

2.3 Empirical Model for Labyrinth Seals

Suryanarayanan (2009) extended the work of Gamal et al. (2006, 2008). Suryanarayanan (2009) developed a model for the incompressible discharge coefficient (2.94) and expansion factor (2.95) of a gas through a labyrinth seal. The parameters used in equations (2.94) through (2.99) are identified in Figure 2.10.

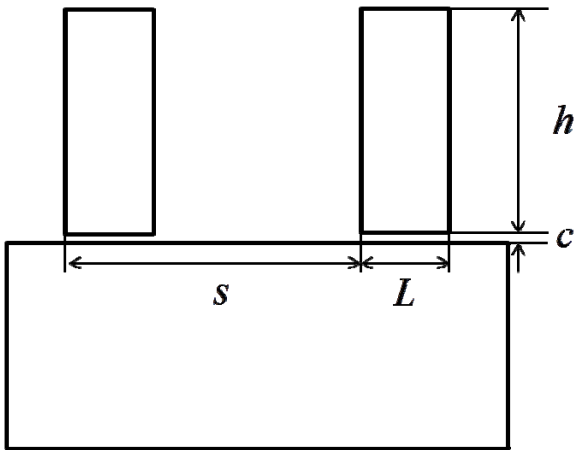

Figure 2.10 Parameters used in empirical model by Suryanarayanan (2009)

Equation (2.94) represents the incompressible discharge coefficient of the first seal in a labyrinth seal.

$$C_d\big|_{PR=1}^{1^{st}\,seal} = \frac{0.7757 - 0.002051\,L/c}{\left(1 + 44.86\dfrac{L/c}{\mathrm{Re}_{D_h}}\right)^{0.2157}} \tag{2.94}$$

Equation (2.95) represents a compressibility factor that was determined to vary linearly with pressure ratio.

$$\psi = 0.558\,PR + 0.442 \tag{2.95}$$

The empirical discharge coefficient and compressibility factor are then input into equation (2.96) to determine the mass flux through the labyrinth seal.

$$G_{empirical} = C_d\big|_{labyrinth}\,\psi\sqrt{2\,\rho_{in}\left(P_{in}-P_{out}\right)} \tag{2.96}$$

The model was extended for subsequent throttling by employing the empirical relationships presented in (2.97) through (2.99). Note that equation (2.98) represents an empirical kinetic energy carry-over coefficient which accounts for the exiting flow between adjacent coaxial seals.

$$C_d\big|_{labyrinth}^{2^{nd}-n^{th}\,seal} = C_d\big|_{labyrinth}^{1^{st}\,seal}\left(0.925\gamma^{0.861}\right) \tag{2.97}$$

$$\gamma = \left(1-6.5\left(\frac{c}{s}\right)-8.638\left(\frac{c}{s}\right)\left(\frac{L}{s}\right)\right)\left(\mathrm{Re}+R_0\right)^{\left(2.454\left(\frac{c}{s}\right)+2.268\left(\frac{c}{s}\right)\left(\frac{L}{s}\right)^{1.678}\right)} \tag{2.98}$$

$$R_0 = \left(1-6.5\left(\frac{c}{s}\right)-8.638\left(\frac{c}{s}\right)\left(\frac{L}{s}\right)\right)^{\left(\frac{-1}{2.454\left(\frac{c}{s}\right)+2.268\left(\frac{c}{s}\right)\left(\frac{L}{s}\right)^{1.678}}\right)} \tag{2.99}$$

The applicability of the model is summarized in equation (3.1).

$$
\begin{aligned}
&PR \to 1 \\
&0.0075 < \frac{c}{s} < 0.0375 \\
&0.0075 < \frac{L}{s} < 0.5 \\
&2.67 < \frac{L}{c} < 66.67 \\
&0.75 < \frac{h}{s} < 4 \\
&134 < \mathrm{Re}_{D_h} < 15000
\end{aligned}
\tag{3.1}
$$

References

Alder, G.M., 1976, Ph.D. thesis. “Transonic Flow through Sharp-Lipped Convergent Nozzles”, University of Edinburgh.

Benson, R.S. and Pool, D.E., 1965, “The Compressible Flow Discharge Coefficients for a Two-Dimensional Slit”, Int. J. Mech. Sci., Vol. 7, pp. 337-353.

Buseman, A., 1937, “Note on Contraction Coefficients of Jets of Gas”, J. Research, US National Bureau of Standards, pp. 765-775.

Chaplygin, S.A., 1902, “Gas Jets”, Scientific Memoirs, Moscow University, English Translation: NACA TM1063, 1944.

Churchill, S.W., 1977, “Friction-factor equation spans all fluid-flow regimes”, Chemical Engineering, Vol. 84 pp. 91-92.

Colebrook, C.F., 1939, “Turbulent Flow in Pipes with Particular Reference to the Transitional Region between the Smooth and the Rough Pipe Laws”, J. Inst. Civil Eng. Vol 11, pp. 133-156.

Dias, F., Elcrat, A.R., and Trefethen, L.N., 1987, “Ideal jet flow in two dimensions”, J. Fluid Mech., vol. 185, pp 275-288.

Fenain, M., Dutouquet, L., and Solignac, J.L., 1974, “Calcul des Performances d’une Tuyere Propulsive Convergente. Comparaison avec L’Experience”, La Recherche Aerospatiale, No. 5, pp. 261-276.

Filippov, G.A., Saltanov, G.A., Sivoborod, V.A., Kosolapov, Y.S., 1982, “Discharge of Gases with Differing Adiabatic Exponents”, Izvestia Akademii Nauk SSSR, Energetika I Transport, Vol. 20, No. 1, pp 121-126, English Translation: Allerton Press Inc.

Frankl, F.I., 1947, “The Flow of a Supersonic Jet from a Vessel with Plane Walls”, Dokl. Akad. Nauk. SSSR Vol. 58, No. 3, pp. 381-384.

Garabedian, P.R., 1956, “The Mathematical Theory of Three-Dimensional Cavities and Jets”, Bulletin of the American Mathematical Society, Vol. 62, pp. 219-235.

Gamal, A.M., Ertas, B.H., and Vance, J.M., High-pressure pocket damper seals: leakage rates and cavity pressures. Proceedings of GT2006 ASME Turbo Expo 2006: Power for Land, Sea, and Air, May 8-11, 2006, Barcelona, Spain.

Gamal, A.M., 2007, Ph.D. thesis. “Leakage and Rotordynamic Effects of Pocket Damper Seals and See-Through Labyrinth Seals”, Texas A&M University, College Station.

Gamal, A.J., and Vance, J.M., 2008, “Labyrinth Seal Leakage Tests: Tooth Profile, Tooth Thickness, and Eccentricity Effects”, ASME, Vol. 130.

Gurevich, M.I., 1965, “The Theory of Jets in Ideal Fluids”, Academic Press, New York.

Hunt, B.W., 1968, “Numerical Solution of an Integral Equation for Flow from a Circular Orifice”. J. Fluid Mech., Vol. 31, pp. 361-377.
Isbin et al. (1958)

Klein, S.A. and Nellis, G.F., 2011, *Thermodynamics*, UW-Madison DoIT bookstore.

Kosolapov, Y.S. and Sivoborod, V.A., 1984, “Theoretical and Numerical Investigation of the Flow of Gas from Flat Slits and Axisymmetric Openings”, Izvestiya Akademii Nauk SSSR, Mekhanika Zhidkosti I Gaza No. 2, pp. 109-115, English Translation.

Linfield, K.W., 2000, Ph.D. thesis, “A Study of the Discharge Coefficient of Jets from Angled Slots and Conical Orifices”

Moran, M.J., and Shapiro, H.N., 2004, *Fundamentals of Engineering Thermodynamics*, 5th edition, Wiley,

Müller-Steinhagen, H., and Heck, K.A., 1986, “A simple friction pressure drop correlation for two-phase flow in pipes”, Chemical Engineering Processing, Vol. 20, pp. 297-308.

Nellis, G.F., and Klein, S.A., 2009, *Heat Transfer*, Cambridge: New York.

Norwood, R.E., 1962, “Two Dimensional Transonic Gas Jets”, Proc 4th US National Congress of Applied Mechanics, Vol. 2, pp. 1359-1367.

Ould Didi, M.B., Kattan, N., and Thome, J.R., 2002, “Prediction of two-phase pressure gradients of refrigerants inside horizontal tubes”, International Journal of Refrigeration, Vol. 25, pp. 935-947.

Pickett, J.S., 1989, “The Generalization and Evaluation of Solutions Occuring in Chaplygin’s Ideal Gas Jet Theory”, University of Toronto M.A.Sc. thesis.

Rouse, H., and Abul-Fetouh, A., 1950, “Characteristics of Irrotational Flow Through Axisymmetric Orifices”, J. App. Mech., pp. 421-426.

Shah, R.K. and London, A.K., 1978, *Laminar Flow Forced Convection in Ducts*, Academic Press, New York.

Shapiro, A.H., 1953, “The Dynamics and Thermodynamics of Compressible Fluid Flow”, Vol. 1 and 2, Ronald Press, New York.

Suryanarayanan, S., 2009, M.S. thesis, “Labyrinth Seal Leakage Equation”, Texas A&M University, College Station.

Ward-Smith, A.J., 1979, “Critical Flowmetering: The Characteristics of Cylindrical Nozzles with Sharp Upstream Edges”, Int. J. Heat & Fluid Flow, Vol. 1 No. 3 pp. 123-132.

White, F.M., 2008, *Viscous Fluid Flow*, McGraw-Hill.

3 Experimental Test Facility

The experimental apparatus designed and fabricated to aid in this research was developed to measure the flow rate of carbon dioxide driven by large pressure drops through typical shaft seal geometries. The design challenge was to construct a test facility that would operate continuously in the vicinity of the critical point of carbon dioxide (304.1K, 7.4MPa). Stability, low relative error and flexibility were identified as major design goals in the development of this test facility.

An analysis of the major components in the system as well as the methodology employed to design this test facility is provided in the sections that follow. Capturing phenomena near the critical point presents an interesting challenge as thermodynamic conditions vary substantially in this region making testing with any degree of accuracy particularly troublesome. A great deal of effort has been placed in the refinement of this test facility to meet the design challenges encountered in this project.

3.1 Experimental objectives, motivation, and approach

The objective of this research is to measure the flow of carbon dioxide through a shaft-seal interface driven by a large pressure gradient. The fluid parameters studied in this analysis include the upstream pressure, upstream density, and the downstream pressure. The seal geometry is manipulated to change the available flow area as well as other parameters that have

been shown to vary the discharge coefficient. A conceptual illustration of the critical parameters is provided in Figure 3.1.

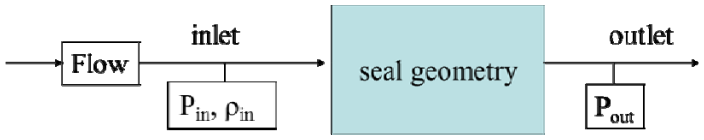

Figure 3.1 Critical parameters outlined for test facility

The motivation for this project is the necessity to quantify the leakage of supercritical carbon dioxide driven through large pressure gradients. The results of this project are crucial to the development of the overall S-CO_2 Brayton cycle. The current objective is to develop good engineering models to understand the fundamental process of a fluid at non-ideal gas conditions undergoing a rapid expansion. The derivation of the original compressibility model shown in Chapter 2 considers the ideal gas relationship outlined here as equation (3.2). One aspect of this research aims to see how significantly the flow deviates from the model based on the compressibility of an ideal gas.

$$pv^k = const \tag{3.2}$$

The desired ranges of the three fluid parameters illustrated in Figure 3.1 are listed in Table 3-1. Primary importance was placed on designing a test facility to support a controllable and steady inlet thermodynamic state. Property variations in the vicinity of a fluid's critical point are large and facilitate the need for precise measurements and regulation. Table 3-1 illustrates the

requirements set forth in the design methodology behind this test facility; notice that the inlet densities vary over a 600 kg/m^3 span. The explanation for this large density span is illustrated in Figure 3.2 where small temperature changes result in exaggerated changes in density along an isobar.

Table 3-1 Test Facility Operating Conditions

PARAMETER	VARIABLE	RANGE
Inlet Density	ρ_{inlet}	200 – 800 kg/m^3
Inlet Pressure	P_{inlet}	7.33 – 14 MPa
Outlet Pressure	P_{outlet}	1.4 – 14 MPa

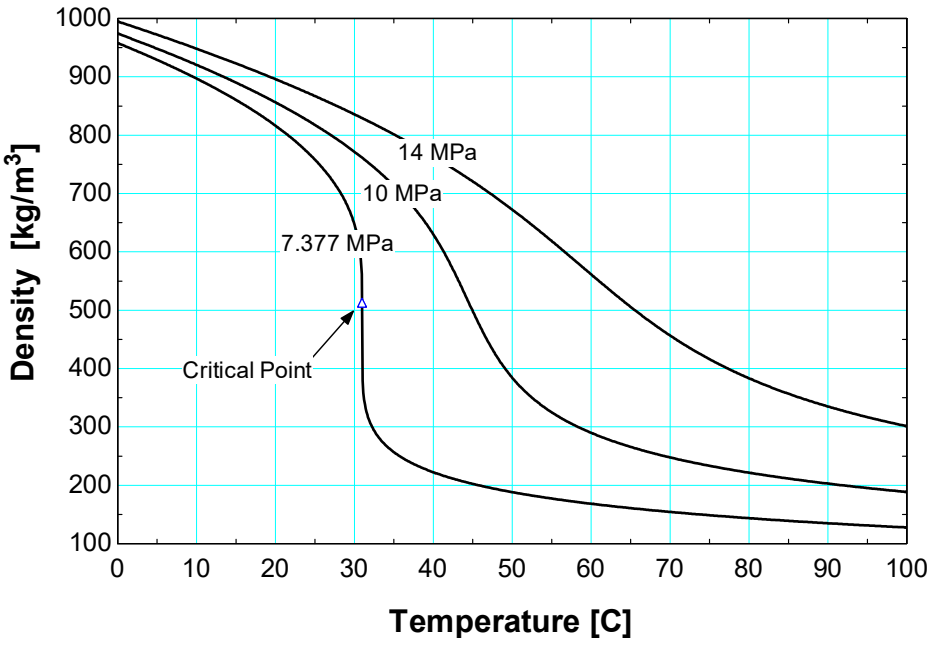

Figure 3.2 Thermodynamic property variation of carbon dioxide near the critical point

The approach taken in this project was to construct a test facility that would continuously cycle carbon dioxide through a constricted interface. An overview of the test facility conceived for this project is shown in Figure 3.3. The facility supports high pressures on the order of 14 MPa and two-phase downstream conditions.

Figure 3.3 shows a schematic of the measurement instrumentation integrated with the compression loop test facility. The crucial instrumentation used in this facility include a coriolis flow meter that measures the mass flow rate and density at the inlet to the test section as well as two pressure transducers that measure the pressures at the inlet and outlet of the test section. Type-E thermocouples are also placed throughout the facility.

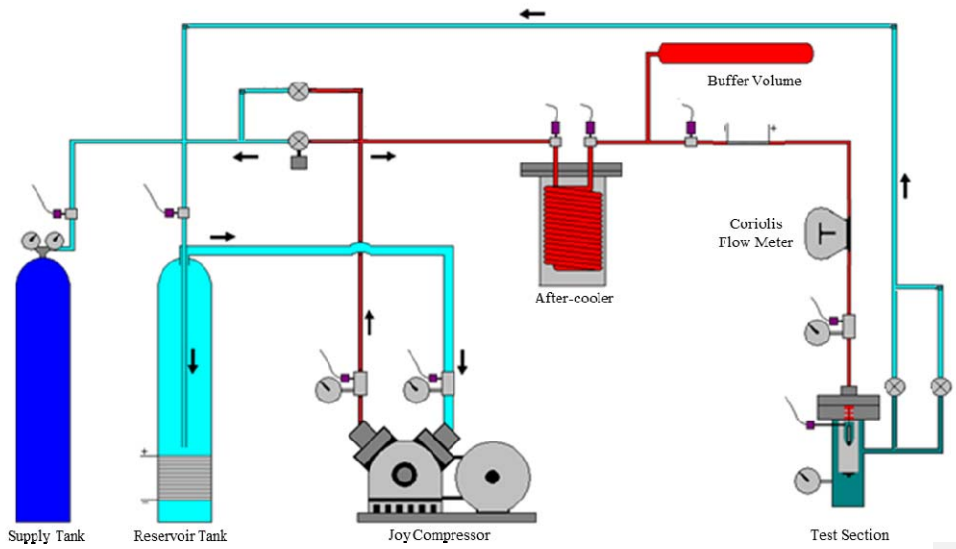

Figure 3.3 Test facility schematic; red=high pressure, cyan=low pressure

Figure 3.3 has been color-coded to provide an overview of the pressures in the system. The lines highlighted in red note the highest pressures found in the system and range from 7.4 -14 MPa. The dark cyan color notes the test section downstream pressure which is regulated by two valves anywhere from 1.4 – 14 MPa. The light cyan color represents the compressor inlet pressure which is maintained by the regulator attached to the supply tank from 1.38 – 3.45MPa. The supply tank is shown in blue and is shipped at room temperature as a two phase mixture often at about 5.5 MPa. Arrows are also drawn in the figure noting the direction of flow in that part of the system.

Many design obstacles were encountered in this project as a result of the wide range of thermodynamic conditions experienced by the working fluid. Of note, the fluid exhibits supercritical, two-phase, and gaseous behavior as it is continuously cycled in the loop. First, it is crucial to fix the inlet state as the proximity to the critical point dictates that small temperature deviations will result in large density variations leading to inadequate results. The flow exits the seal geometry as a two-phase mixture and must subsequently undergo a phase-change to cycle through the compressor. This parameter was particularly troublesome as the mass flow rate through the evaporator is highly dependent on the high pressure inlet density and could result in large pressure drops through the duct work if not adequately accounted for in the system. Finally, large pressure drops compounded with large flow rates facilitated the need for large equipment to promote continuous cycling of the working fluid.

3.2 Compression Loop Cycle

This section documents the modeling assumptions employed in the development of this test facility. A schematic of the facility is presented in Figure 3.4 along with a cycle diagram provided in Figure 3.5. The thermodynamic states shown as 1 through 11 in Figure 3.4 correspond to the points detailed in Figure 3.5.

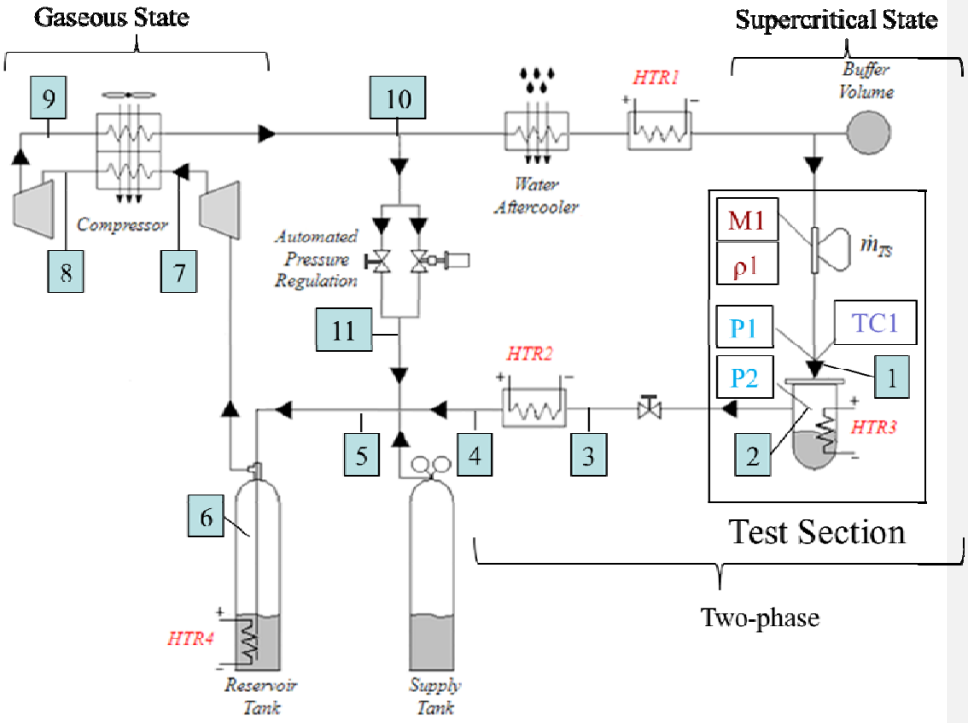

Figure 3.4 Schematic of UW compression loop facility

Figure 3.4 highlights the actual test section integrated with the compression loop facility. The primary instrumentation outlined in Figure 3.1 is detailed here shown as reference points M1, ρ1, P1, P2, and TC1. These points respectively reference the location of measurement of mass flow rate and density with the coriolis mass flow meter, the upstream and downstream pressures, and the temperature at the inlet to the test facility. The test section is the primary focus of this research where the other components used in this facility are crucial to facility operation to support high capacity flow rates and stable operation. Secondary instrumentation has been omitted for clarity in this schematic.

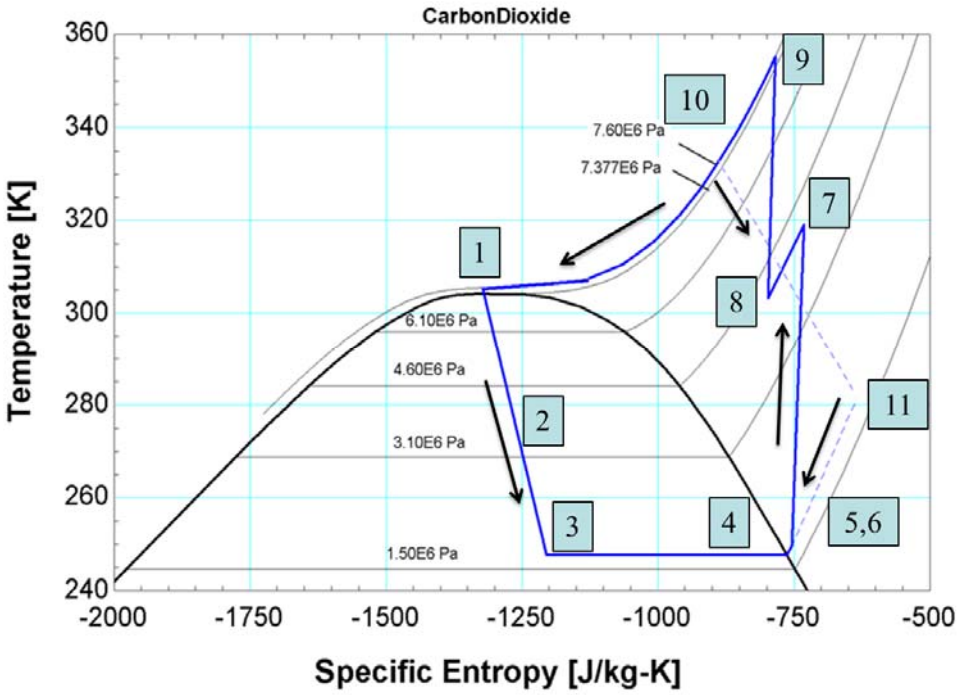

Figure 3.5 Temperature-entropy diagram of UW-Madison S-CO_2 Compression Loop facility

The cycle diagram in Figure 3.5 details the thermodynamic states in the cycle. The primary loop complete with the test section loop is detailed here in blue with the excess loop presented as a dashed line in the background of the figure. The specific entropy of states 1 through 3 vary depending on the desired inlet density. State 1 here is shown in Figure 3.5 starting from a nominal value of 7.6 MPa and 305 K which corresponds to an inlet density of about 500 kg/m^3 as seen in Figure 3.2.

The methodology employed in the design of this test facility begins by specifying the desired values for the inlet state as shown in equation (3.3). The thermodynamic state specified is taken above the critical pressure of carbon dioxide at 7.377 MPa with an inlet density near the critical point.

$$\begin{aligned} &\textit{Supercritical Inlet State} \\ &P_1 = P_{inlet} \\ &\rho_1 = \rho_{inlet} \end{aligned} \tag{3.3}$$

The specific enthalpy at the inlet state is specified according to equation (3.4) and evaluated in Engineering Equation Solver (EES).

$$h_1 = enthalpy\left(Carbon\,Dioxide, P_1, \rho_1\right) \tag{3.4}$$

The flow is throttled through the test section to an outlet pressure specified by equation (3.5). The expansion process is presumed to be isenthalpic as expressed in equation (3.6). Note that if the outlet pressure is sufficiently low, the flow will exit as a two-phase mixture as demonstrated in Figure 3.6.

$$P_2 = P_{outlet} \tag{3.5}$$

$$h_2 = h_1 \tag{3.6}$$

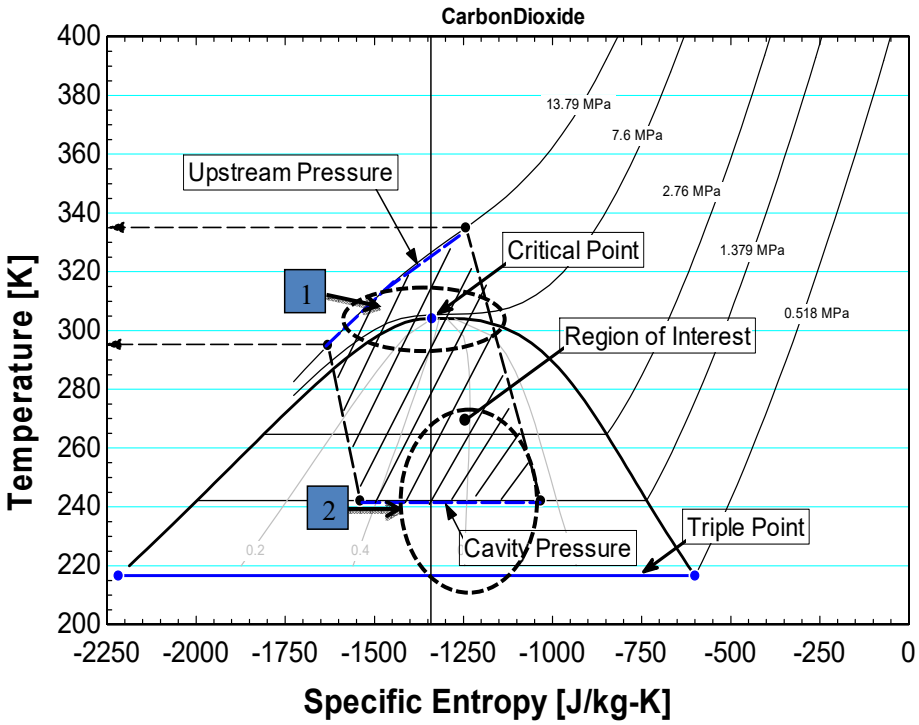

Figure 3.6 Test facility desired operating range

Figure 3.6 demonstrates the desired test facility operating range on a property diagram plot. The possible ranges of upstream and downstream states are circled and labeled 1 and 2 respectively. The broad range of test conditions detailed in Figure 3.6 demonstrates the importance of designing the facility as flexible as possible in order to meet the range of inlet densities specified in Table 3-1.

The flow through the test section then undergoes a secondary throttling process through a valve to reach the lowest pressure of the facility dictated by the compressor inlet pressure as demonstrated in equation (3.7).

$$\begin{aligned} P_3 &= P_{comp-inlet} \\ h_3 &= h_2 \end{aligned} \tag{3.7}$$

The flow is sent through an evaporator as demonstrated in equation (3.8).

$$\begin{aligned} P_4 &= P_3 \\ \dot{Q}_{evaporator} &= \dot{m}_{test-section}\left(h_4 - h_3\right) \end{aligned} \tag{3.8}$$

The working fluid cycled through the test section loop is then combined with the fluid from the excess flow loop as demonstrated in Figure 3.7. The mass and energy balances are shown in equation (3.9). Note that the excess flow loop referred to in equation (3.9) is solved in iterative fashion later in the program.

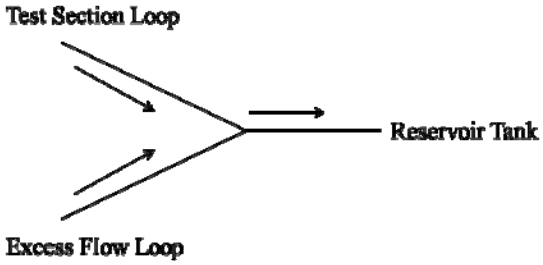

Figure 3.7 Convergent flow paths entering reservoir tank

$$\begin{aligned} \dot{m}_{test-section} + \dot{m}_{excess} &= \dot{m}_{reservoir} \\ \dot{m}_{test-section} h_4 + \dot{m}_{excess} h_{11} &= \dot{m}_{reservoir} h_5 \end{aligned} \tag{3.9}$$

$$P_5 = P_4 \tag{3.10}$$

The flow is then collected in the reservoir tank as shown in equation (3.9). The tank is used to stratify the liquid and gaseous components of the flow in order to separate any residual liquid out of the flow. The bottle is heated in order to vaporize this residual liquid – the extracted carbon dioxide is then sent to the inlet of the compressor as indicated in equations (3.12) and (3.13).

$$P_6 = P_5 \tag{3.11}$$

$$h_5 = h_l(P_5) + h_g(P_5) \tag{3.12}$$

$$h_6 = h_g(P_6) \tag{3.13}$$

The total pressure differential across the two stages of the compressor is assumed to be split evenly between the two stages as shown in equation (3.14) with no pressure drop across the intercooler as shown in equation (3.15).

$$P_7 - P_6 = P_9 - P_8 \tag{3.14}$$

$$P_8 = P_7 \tag{3.15}$$

The compressor is modeled as two separate stages with both intercooling and after-cooling capability. An isentropic efficiency of $\varepsilon = 0.85$ is estimated for each stage. The equations for the first stage are implemented in EES as demonstrated in equations (3.16) through (3.19).

$$s_6 = entropy\left(Carbon\ Dioxide, P_6, h_6\right) \tag{3.16}$$

$$s_{7,isentropic} = s_6 \tag{3.17}$$

$$h_{7,isentropic} = enthalpy(Carbon\ Dioxide, P_7, s_{7,isentropic}) \tag{3.18}$$

Equation (3.19) is implicitly solved for h_7 in EES.

$$\varepsilon = \frac{h_{7,isentropic} - h_6}{h_7 - h_6} \tag{3.19}$$

The intercooling stage is modeled as demonstrated in equation (3.20) and (3.22).

$$dT \approx 10^{\circ} C \tag{3.20}$$

$$T_8 = T_{air} + dT \tag{3.21}$$

$$\dot{Q}_{intercooler} = \dot{m}_{compressor} \left(h_8 - h_7 \right) \tag{3.22}$$

A second compressor stage is modeled similar to the first with equations (3.24) through (3.27) where the exit pressure returns to the inlet pressure as shown in equation (3.23).

$$P_9 = P_1 \tag{3.23}$$

$$s_8 = entropy(Carbon\,Dioxide, P_8, T_8) \tag{3.24}$$

$$s_{9,isentropic} = s_8 \tag{3.25}$$

$$h_{9,isentropic} = enthalpy\left(Carbon\,Dioxide, P_9, s_{9,isentropic}\right) \tag{3.26}$$

Again, equation (3.27) is implicitly solved for h_9.

$$\eta_{C,isentropic} = \frac{h_{9,isentropic} - h_8}{h_9 - h_8} \tag{3.27}$$

The compressor after-cooling stage is modeled similar to the intercooling stage between the two compression stages.

$$\dot{Q}^{1}_{intercooler} = \dot{Q}^{2}_{intercooler} \tag{3.28}$$

The flow splits at this point and is governed by the required flow rate through the test section. The mass balance governing this process was shown previously in (3.9) but shown here as (3.29) for reference.

$$\dot{m}_{compressor} = \dot{m}_{test-section} + \dot{m}_{excess} \tag{3.29}$$

The amount of cooling required to return to the inlet state P_1, ρ_1 is provided by equation (3.30).

$$\dot{Q}_{aftercooler} = \dot{m}_{test-section}\left(h_{10} - h_1\right) \tag{3.30}$$

The residual flow is cycled back through the excess loop and modeled as an isenthalpic throttling process with equation (3.31).

$$h_{10} = h_{11} \tag{3.31}$$

3.3 Extensive Cycle Estimates

The pressure drop due to form losses only was used as a baseline when designing this facility. The equipment needed to be of adequate size to accommodate the large density and pressure gradients in this test facility.

The most crucial aspect of this facility was making a preliminary estimate of the flow rate. Conceptually, Figure 3.6 shows that the fluid starts off from an initially supercritical state and proceeds through a throttle to a two-phase region. These conditions ensure that the flow will cavitate and make modeling the flow particularly troublesome. The approach used in the development of this facility was to use the single phase isentropic expansion model described in Chapter 2 to estimate the mass flow rate through the geometry used at Sandia National Laboratories and compare it to the information reported in Wright et al (2009) as shown here in Table 3-2.

Table 3-2 Reported leakage flow rate estimates and measurements reported in Wright et al (2009) compared to single-phase isentropic flow model developed in Chapter 2

	Barber-Nichols and Sandia National Laboratory	
	Estimate A	Estimate B
Upstream Pressure	13.84 MPa	7.7 MPa
Input Temperature	325 K	325 K
Downstream Pressure	1.38 MPa	1.38 MPa
Diameter of Journal	13.97 mm	13.97 mm
Diametrical Clearance	76.2 μm	76.2 μm
Reported Mass Flow Rate	0.0882 kg/s	0.0326 kg/s
UW Mass Flow Rate	0.105 kg/s	0.0435 kg/s
% Difference	19.0%	33.4%

Estimate A represents the expected thermodynamic state the fluid will be in upon exiting the compressor expanded through the shaft seals to a downstream cavity pressure of 1.38 MPa.

Estimate B is more indicative of a process where the compressor inlet thermodynamic state is allowed to expand through the shaft seals to a downstream cavity pressure of 1.38 MPa.

Table 3-2 compares the difference between the reported mass flow rate shown in Wright et al. (2009) and the UW model developed in Chapter 2. Note that the results of the UW model shown in Table 3-2 do not consider two-dimensional effects as the discharge coefficient has been set to unity $C_d = 1$. A facility capable of replicating the working fluid pressures and upstream temperatures was conceived based on the UW methodology used to model the mass flow rate shown in *Estimate A* of Table 3-2.

The next step was to determine the maximum clearance area the facility could support. This value was dictated by two key components: the coriolis mass flow meter and the compressor. The maximum expected flow rate could not exceed the capacity of the flow meter. Likewise, the capacity of the compressor had to support large flow rates delivered at high pressure.

The coriolis flow meter used in this experiment is a CMF010 Rosemount coriolis flow meter with a maximum capacity of 0.03 kg/s. As such, it was necessary to reduce the available flow area in order to decrease the maximum flow rate across the desired 12 MPa pressure drop. Mass flow rates on the order of 0.1 kg/s as estimated in Table 3-2 were not possible with this flow meter.

The size of the compressor required to support flow rates on the order of 0.1 kg/s delivered at 13.8 MPa posed the largest limitation to this research. A simple analysis of the required

volumetric flow rate at standard temperature and pressure conditions (STP) corresponding to a mass flow rate of 0.1 kg/s is presented below in equation (3.32). It shows that the required volumetric flow rate is about 115 scfm.

$$\begin{aligned}
&\dot{m}_{test-section} = 0.1\frac{kg}{s} \\
&\rho_{STP} = density\left(Carbon\,Dioxide, P = 101.325\,kPa, T = 20\,^{\circ}C\right) = 1.84\frac{kg}{m^3} \\
&\dot{m}_{test-section} = \rho_{STP}\dot{V}_{STP} \\
&\dot{V}_{STP} = 0.054\frac{m^3}{s} = 115\,scfm
\end{aligned} \tag{3.32}$$

A compressor capable of delivering a capacity dictated by equation (3.32) at pressures of 13.8 MPa was not available at the time of this initial estimate. Delivery was also on the order of 24 weeks so the effort to test geometry similar to that at Sandia National Laboratories was left to a later date.

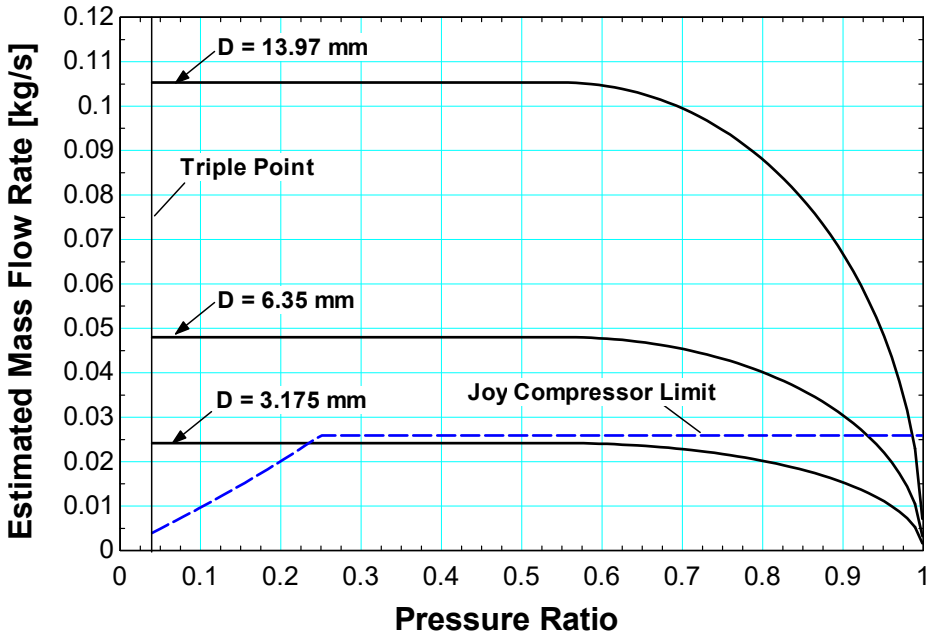

Figure 3.8 Estimate of mass flow rate for several different journal diameters at an inlet pressure of 13.8 MPa and temperature of 325 K. Compressor limit based on equation (3.34) through (3.40)

The flow area was reduced to accommodate a lower flow rate. Figure 3.8 demonstrates the importance of reducing the diameter of the shaft journal in this test series. The reduction in area was accomplished by reducing the journal diameter size as demonstrated in Figure 3.8. The clearance area was kept at a prototypical level of 76.2 μm for each case. The final iteration showed that flow rates through shaft diameters on the order of $D = 3.175 mm$ could be tested with the available equipment. The estimated volumetric flow rate through the compressor based on a similar analysis exemplified in equation (3.32) is shown here as equation (3.33).

$$\dot{m}_{test-section} = 0.03\frac{kg}{s}$$
$$\dot{V}_{STP} = 0.016\frac{m^3}{s} = 34\,scfm \tag{3.33}$$

Notice that the mass flow rate through prototypical geometry identified in Table 3-2 is shown to exceed the estimated capacity of the available Joy compressor. A photograph of this compressor is provided in Figure 3.9 along with a specification sheet provided in Table 3-3 Clearance area about shafts with diameters of $D = 13.97\,mm$ and prototypical diametrical clearances of 76.2 μm were clearly unattainable. The following analysis demonstrates the estimated capacity of the Joy compressor shown here in equation (3.34) through (3.40).

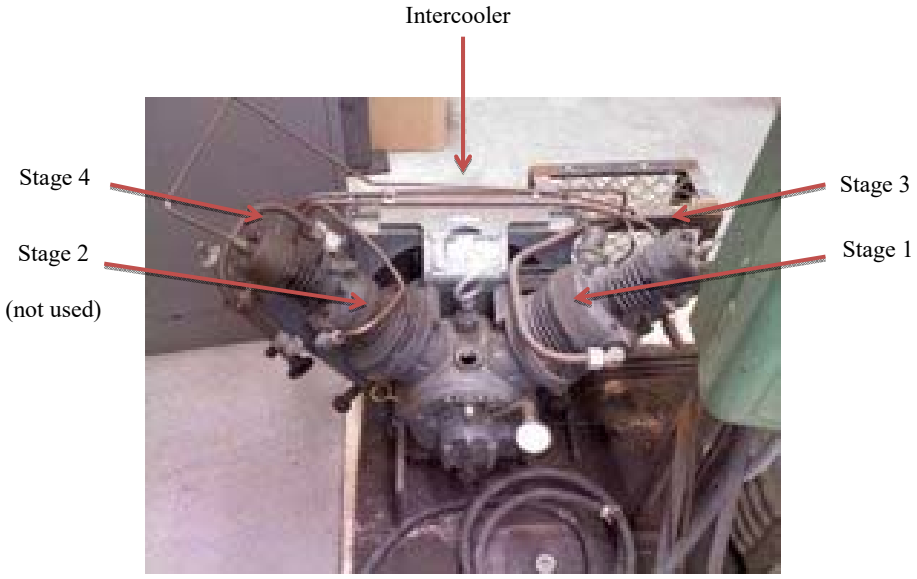

Figure 3.9 Four stage piston-type Joy compressor with the bottom two stages 1 and 2 not used in this experiment

Table 3-3 Measured Joy compressor parameters

PARAMETER	VARIABLE	RANGE
Third Stage		
Stroke	$S\|_{comp}^{3rd}$	5.715 cm
Bore	$B\|_{comp}^{3rd}$	2.680 cm
Volume	$V\|_{comp}^{3rd}$	32.23 cm^3
Fourth Stage		
Stroke	$S\|_{comp}^{4th}$	5.715 cm
Bore	$B\|_{comp}^{4th}$	1.397 cm
Volume	$V\|_{comp}^{4th}$	8.760 cm^3
Miscellaneous		
Frequency	f_{comp}	1540 rpm

The Joy compressor shown in Figure 3.9 used in this research is an old 4-stage piston compressor shown in Figure 3.9 where the bottom two low pressure stages could not be used in order to prevent the formation of solid carbon dioxide crystals from forming inside the compressor. The objective was to avoid pressures approaching the triple point of carbon dioxide at 518 kPa

The maximum pressure entering the compressor inlet was restricted to 3.45 MPa as demonstrated by equation (3.34). It was important to stay below this value for two reasons based on the hardware layout of this project. The major restriction was the compressor inlet stage itself. The compressor is old and little to no information remains about the integrity of the system. At the onset of this project, the compressor was cycled with air and the natural inlet pressure to this

stage was quantitatively found to be only slightly higher than 3.45 MPa. The second major restriction was based on the maximum outlet pressure of the regulator used in this project.

$$P_{\max-stage3} = 3.45MPa \tag{3.34}$$

The inlet pressure to the compressor could then be regulated anywhere below the value expressed in equation (3.34) as shown here in equation (3.35).

$$P_{comp-inlet} = \min\left(P_{outlet},\ P_{\max-stage3}\right) \tag{3.35}$$

The saturated vapor density $x = 1$ was determined based on the compressor inlet pressure shown in equation (3.36).

$$\rho_{comp-inlet} = density\left(CarbonDioxide, P = P_{comp-inlet}, x = 1\right) \tag{3.36}$$

The volumetric efficiency of both stages coupled together was approximated based on equation (3.37). Again the bottom two stages are not used to compress carbon dioxide so the cumulative effect of leakage from the high pressure stages into the low pressure stages is unknown. Equation (3.37) is by no means an exact measurement of the coupled-stage volumetric efficiency, but does provide at least a baseline of what one might expect in the system. The volumetric efficiency of each stage was estimated at $\eta\big|_{comp} = 0.65$. The compressor is old and

prone to appreciable leakage from the high pressure stages into the low pressure stages (which are not used).

$$\frac{1}{\eta_{comp,two-stages}} \approx \frac{1}{\eta|_{comp}^{stage\,3}} + \frac{1}{\eta|_{comp}^{stage\,4}} \tag{3.37}$$

The volumetric flow rate through the compressor was approximated by measuring the frequency of the compressor f_{comp} and the volume of the cylinders inside the compressor shown here as $V|_{comp}^{3^{rd}}$ and $V|_{comp}^{4^{th}}$. The results were shown in Table 3-3. Note that a single stage does not support the required inlet to outlet compression ratio to reach testing pressures above 7.4 MPa.

The volumetric flow rate was estimated by equation (3.38) followed by the mass flow rate in equation (3.40).

$$\dot{V}_{comp} = f_{comp} V|_{comp}^{3^{rd}} \tag{3.38}$$

Finally, the mass flow rate through the compressor was approximated based on equation (3.40) with the result plotted in Figure 3.8. The referenced density corresponds to state 6 of the cycle shown here as equation (3.39).

$$\rho_{comp-inlet} = \rho_6 = density\left(CarbonDioxide, P_6, h_6\right) \tag{3.39}$$

$$\dot{m}_{compressor} = \eta_{comp,two-stages} \rho_{comp-inlet} \dot{V}_{comp} \tag{3.40}$$

The final mass flow estimate was determined as the difference between the compressor through flow to the expected mass flow rate through the test section as demonstrated in equation (3.41).

$$\dot{m}_{excess} = \dot{m}_{compressor} - \dot{m}_{test-section} \tag{3.41}$$

Several valves were integrated into the test facility to accommodate the full range of flow rates and pressure gradients expected through the test section as illustrated for the 3.175 mm shaft detailed in Figure 3.8. The valve network is demonstrated in Figure 3.10 with the test loop and excess loops highlighted.

The valves chosen for this facility were determined based on their maximum flow coefficients denoted in literature as C_v. The flow coefficient is effectively a standard measure of the flow conductance an object such as a valve, orifice, etc. imposes on the flow. Figure 3.10 reports the maximum flow coefficient for each valve currently implemented in the facility. The valve detailed with a max flow coefficient of $C_v = 0.9$ will be replaced in the future as it is too big. Instead, it will be replaced with a much smaller valve on the order of C_v=0.04 as demonstrated in the excess loop.

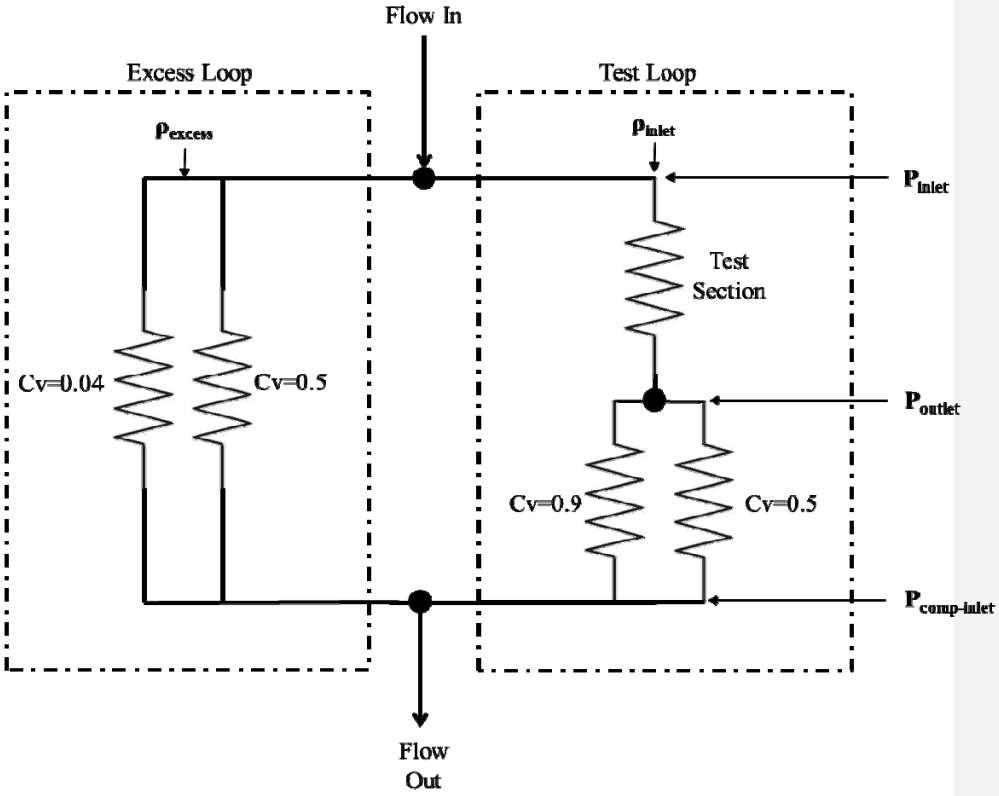

Figure 3.10 Valve network schematic where the max flow coefficient Cv for each valve is shown

The excess flow loop in the figure details a relatively large valve in parallel with a small valve. The idea here is to effectively set the pressure differential from P_{inlet} to $P_{comp-inlet}$ with the larger valve and then have the smaller valve regulate the pressure by using a motorized mechanism to regulate the pressure differential controlled by a PID system. The objective of this system is to regulate the inlet pressure to the test loop by implementing small changes to the mass flow rate through the excess loop. Valve selection for this purpose was based on the following analysis.

The definition of the flow coefficient is quite often misinterpreted as simply equation (3.42). The problem is that equation (3.42) is not dimensionless and the definition provided here is strictly for incompressible flow through a flow restriction. The following documentation provides a simple overview from information attained via *swagelok.com* and *goreg.com.* Equations (3.42) through (3.45) were obtained from a *swagelok.com* technical bulletin entitled *Valve Sizing* (2007). Note that the published leading coefficient in equation (3.44), $coeff = \frac{1}{0.471}$, has been altered from its original form in *Valve Sizing* (2007) to be consistent with values obtained from *goreg.com*.

$$C_v = Q\sqrt{\frac{SG}{\Delta P}} \qquad Dimensional, Incompressible \tag{3.42}$$

Equation (3.43) is the measured industry standard for liquid service through a flow restriction. Q in this case represents the flow rate in US gallons per minute (not Imperial), GPM; SG_{liquid} is the specific gravity of the fluid relative to water at 60°F; and the pressure differential is measured in psi and denoted as ΔP. Note that since the equation only applies to incompressible fluids, no reference pressure for water is given and is assumed to be 1 atm. N_1 is a unit conversion variable where $N_1 = 1$ for the reference units provided here. Effects of temperature are commonly ignored for liquids.

$$Q_{liquid,STP} = N_1 C_v \sqrt{\frac{\Delta P}{SG_{liquid}}} \tag{3.43}$$

The simple formula shown for liquid service in (3.43) is severely contrasted with the definition required for gas service through a flow restriction shown here in equation (3.44) and (3.45). Q in this case represents the flow rate in standard cubic feet of air per minute, SCFM; SG_{gas} is the specific gravity of the fluid relative to air where both are determined at 60°F and 1 atm; the pressure differential is measured in psi and denoted as ΔP; P_{in} is the inlet pressure given in psia; and T_{in} is the inlet temperature in °R. $N_2 = 13.9$ for the reference units provided here.

Equation (3.44) is used for gas flow service above an assumed critical pressure ratio of 0.5. Note that the critical pressure of a substance is rarely exactly 0.5 as was demonstrated in Figure 2.1 in chapter 2. However, this industry standard does seem to be a decent rule of thumb provided the aspect ratio of the flow restriction is kept at a minimum. Note that the critical pressure ratio of air is approximately 0.53.

$$Q_{gas,STP} = \frac{1}{0.471} C_v N_2 P_{in} \left[1 - \frac{2\Delta P}{3P_{in}} \right] \sqrt{\frac{\Delta P}{P_{in} T_{in} SG_{gas}}} \quad PR > 0.5 \tag{3.44}$$

$$Q_{gas,STP} = C_v N_2 \frac{P_{in}}{\sqrt{T_{in} SG_{gas}}} \qquad PR \leq 0.5 \tag{3.45}$$

The required size of the valve was estimated based on the following analysis using the definitions provided in equations (3.44) and (3.45) and desired values reported in Table 3-4.

Table 3-4 Parameters used in valve sizing estimate

PARAMETER	VARIABLE	VALUE
Inlet Temperature	T_{inlet}	325 K
Inlet Pressure	P_{inlet}	13.8 MPa
Outlet Pressure	P_{outlet}	1.4 MPa – 13.8 MPa
Expected Volumetric Flow Rate	$Q_{excess,STP}$	0 – 0.016 m^3/s

The expected values of pressures, temperatures, and flow rates identified in Table 3-4 are those used to construct Figure 3.8. The additional volumetric flow rate was estimated based on equation (3.33).

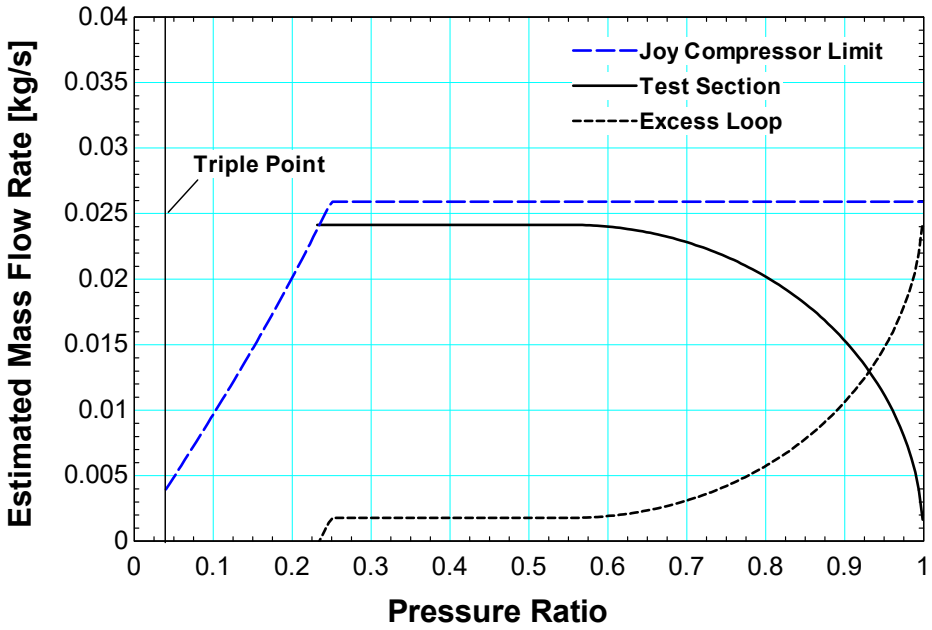

Figure 3.11 Expected flow rates in test facility from an initial inlet pressure of 13.8 MPa and an upstream temperature of 325 K

Figure 3.11 illustrates the estimated flow rates through the facility as a function of pressure ratio when throttling carbon dioxide with an upstream pressure of 13.8 MPa and an upstream temperature of 325 K. Notice that the flow rate through the compressor is fixed and is split between the test section and the excess loop as modeled in equation (3.41).

With the flow rate through the excess loop fixed by equation (3.41), an estimation of the maximum required valve coefficient can be determined as illustrated in Figure 3.12. The methodology employed in this estimation is shown in equations (3.46) through (3.49).

The specific gravity $SG = 1.53$ for carbon dioxide at standard conditions is calculated in EES as shown in equation (3.46). Notice the reference values are consistent with those necessary to apply equations (3.44) and (3.45).

$$\begin{aligned} \rho_{CO_2-ref} &= density\left(Carbon\ Dioxide, P = 1\,atm, T = 60^\circ F\right) \\ \rho_{Air-ref} &= density\left(Air, P = 1\,atm, T = 60^\circ F\right) \\ SG &= \frac{\rho_{CO_2-ref}}{\rho_{Air-ref}} = 1.53 \end{aligned} \tag{3.46}$$

The excess flow rate $\dot{m}_{excess}$ as calculated from equation (3.41) and illustrated in Figure 3.11 is divided by the reference density to calculate the excess volumetric flow rate at 60°F and 1 atm as demonstrated in (3.47).

$$Q_{excess,STP} = \frac{\dot{m}_{excess}}{\rho_{CO_2-ref}} \tag{3.47}$$

The pressure differential is obtained from equation (3.48) due to the pressure gradient experienced by the excess loop as was demonstrated in the resistance network highlighted in Figure 3.10.

$$\Delta P = P_{inlet} - P_{comp-inlet} \tag{3.48}$$

Finally, the flow coefficient is determined using equations (3.44) and (3.45) in a function. The result is shown as a function of pressure ratio in Figure 3.12.

$$C_v = f\left(P_{inlet}, T_{inlet}, \Delta P, SG, Q_{excess,STP}\right) \tag{3.49}$$

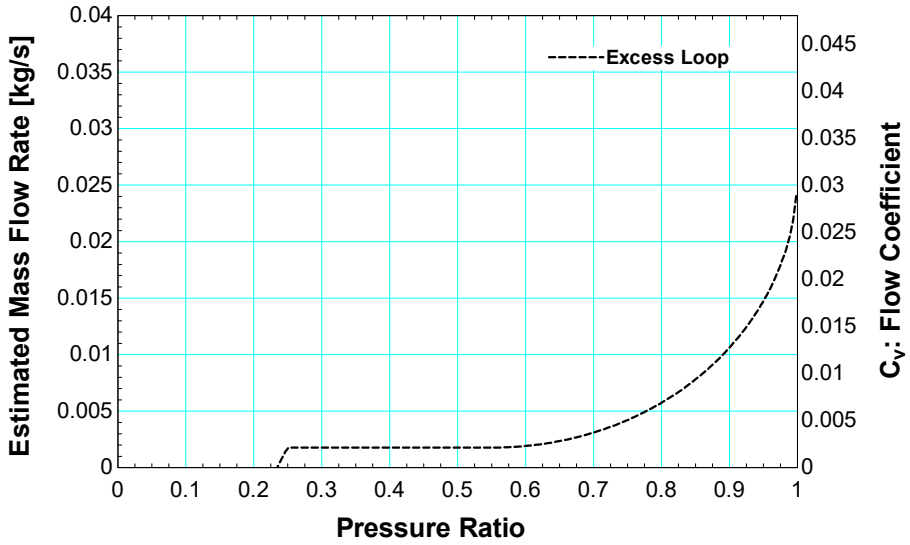

Figure 3.12 Excess flow loop valve coefficient estimation as a function of pressure ratio and estimated mass flow rate

Figure 3.12 shows that the maximum desired flow coefficient should be about $C_v = 0.03$; an SS-31RS4 valve from Swagelok was identified to meet the criteria specified. The flow coefficient as a function of the number of valve turns is detailed here as illustrated in Figure 3.13. Notice that the valve has particularly good flow coefficient resolution as a function of the number of turns at $\Delta C_v = \frac{0.0025}{turn}$. Furthermore, the maximum allowable pressure of the valve is 34.5 MPa which is well above the minimum 13.8 MPa requirement.

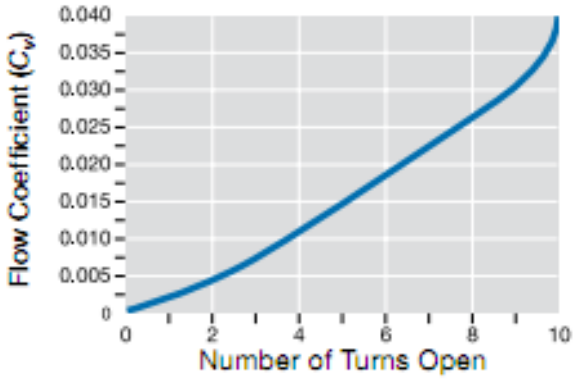

Figure 3.13 Flow coefficient for SS-31RS4 valve from Swagelok

3.4 Geometrical Parameters and Eccentricity Study

3.4.1 Geometrical Parameters

Section 3.3 illustrated that the desired pressure gradients investigated in this study coupled with the available compression equipment required that the flow conductance of the test section be reduced as much as possible. This meant that the flow had to be constricted by decreasing the effective available flow area to about $A_c = 0.3846 mm^2$. Conceptually, this meant that the flow coefficient C_v had to be of the same order as that used to size the excess loop valve detailed in Figure 3.12. Equation (3.50) provides an overview of the results obtained in that study.

$$O(C_v) \approx 0.03 \tag{3.50}$$

The effective flow area was minimized to acceptable levels by establishing maximum geometric values for each constrictive device chosen for investigation as detailed in Table 3-5. The natural

annular orifices which occur between the outer diameter of various shafts and the inner diameter of various seals are used to simulate labyrinth seals.

Table 3-5 Components attributing to available flow area in test section

PARAMETER	VARIABLE	VALUE	UNCERTAINTY
ORIFICE			
Nominal orifice diameter	$D_{orifice}$	0.711 mm	12.7 μm
SEAL			
Nominal seal diameter	D_{seal}	3.183 mm	3.81 μm
Seal length	L_{seal}	0 – 7.62 mm	2.54 μm
Max seal roughness	e_{seal}	0.305 μm	
SHAFT			
Nominal shaft diameters	D_{shaft}	3.1 – 3.175 mm	0.762 μm
Shaft length	L_{shaft}	50.8 mm	
Max shaft roughness	E_{shaft}	0.051 μm	

3.4.2 Eccentricity Overview

Eccentricity is an important characteristic that must be controlled in devices which constrict fluid flow through an annular region in order to eliminate undesirable two dimensional effects. Eccentricity has been reported to increase the flow rate in many studies such as Piercy et al. (1933), Tao and Donovan (1955), and Gamal (2007). The change is flow rate due to eccentricity is conceptually described in this section. Note that in all instances identified, eccentricity is shown to increase the flow rate through an annular profile over the concentric counterpart.

The velocity profile in a concentric annular duct is reported in equation (3.53). This is an exact solution to the equations reported in (3.51) with boundary conditions identified in (3.52). Note that $r = a$ is the radial dimension of r at the outer radius and $r = b$ is the radial dimension of r at the inner radius. Furthermore, equations reported in (3.51) make the following assumptions:

- The flow is axisymmetric
- Fully developed incompressible flow
- Constant properties through the chamber
- Potential energy effects are negligible

$$\frac{\mu}{r}\frac{\partial}{\partial r}\left[r\frac{\partial u_x}{\partial r}\right] = \frac{\partial p}{\partial x}$$
$$\frac{\partial p}{\partial r} = 0 \tag{3.51}$$

$$u_x\big|_{r=a} = 0 \qquad \textit{outer radius}$$
$$u_x\big|_{r=b} = 0 \qquad \textit{inner radius} \tag{3.52}$$

Note that the pressure differential $\frac{\partial p}{\partial x}$ in (3.53) has become the total differential $\frac{dp}{dx}$ as the pressure gradient with respect to r is shown to be negligible in (3.51).

$$u_x(r) = \frac{1}{4\mu}\left(\frac{dp}{dx}\right)\left[\left(r^2 - b^2\right) - \left(a^2 - b^2\right)\frac{\ln\frac{r}{b}}{\ln\frac{a}{b}}\right] \tag{3.53}$$

Several velocity profiles based on equation (3.53) are plotted in Figure 3.14 where $a = 1$ and $0 < \frac{b}{a} < 1$. Also plotted is the location of the maximum velocity u_{max} through the annular channel for $0.001 < \frac{b}{a} < 1$. Notice that the location of the maximum velocity u_{max} seems to show the greatest sensitivity as $\frac{b}{a} \to 1$ (corresponding to a very small clearance annulus). For this reason, it would seem that the maximum velocity would show the greatest relative change to even minor deviations in eccentricity as $\frac{b}{a} \to 1$.

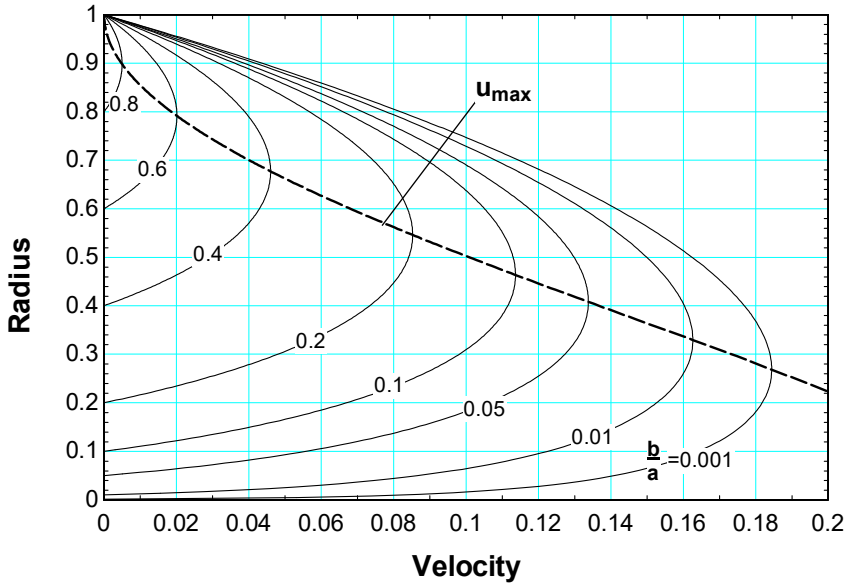

Figure 3.14 Velocity profiles through an annular region for a=1, 0<b/a<1

The flow rate through a concentric annular duct is derived by integrating equation (3.53) across the velocity profile to obtain equation (3.54).

$$Q_{concentric} = \frac{\pi}{8\mu}\left(-\frac{dp}{dx}\right)\left[a^4 - b^4 + \frac{\left(a^2 - b^2\right)^2}{\ln\frac{a}{b}}\right] \tag{3.54}$$

White (2006) reproduces the result obtained from Piercy et al. (1933) to evaluate the flow rates through eccentric channels. The result is shown here as equation (3.57) where the parameters used in the equation are demonstrated in equation (3.58). Equation (3.57) is an exact solution for laminar flow through eccentric annular channels; the result was obtained by considering a complex-variable method of the form demonstrated here as equations (3.55) and (3.56).

$$z' = M\tan\frac{\varsigma}{2} \tag{3.55}$$

where

$$z' = x + iy \;\; and \;\; \varsigma = \xi + i\eta \tag{3.56}$$

$$Q_{eccentric} = \frac{\pi}{8\mu}\left(-\frac{dp}{dx}\right)\left[a^4 - b^4 - \frac{4c^2M^2}{\beta - \alpha} - 8c^2M^2\sum_{n=1}^{\infty}\frac{ne^{-n(\beta+\alpha)}}{\sinh\left(n\beta - n\alpha\right)}\right] \tag{3.57}$$

$$
\begin{aligned}
F &= \frac{a^2 - b^2 + c^2}{2c} \\
M &= \left(F^2 - a^2\right)^{1/2} \\
\alpha &= \frac{1}{2}\ln\frac{F + M}{F - M} \\
\beta &= \frac{1}{2}\ln\frac{F - c + M}{F - c - M}
\end{aligned}
\tag{3.58}
$$

Figure 3.15 illustrates the ratio between equations (3.57) to (3.54); that is, the ratio of the flow rate for an eccentric to a concentric annulus. The figure shows that the relative impact of eccentricity is substantial in laminar flow, especially in narrow gaps where $\frac{b}{a} \to 1$. In the worst case scenario, the flow rate will increase by a factor of 2.5 through a narrow gap at maximum eccentricity. This is the same result which is obtained from lubrication theory which applies to flow rates through a narrow annulus identified here as equation (3.59) and reproduced from White (2006); the result obtained from this equation is also plotted in the figure.

$$
\frac{Q_{eccentric}}{Q_{concentric}} = 1 + \frac{3}{2}\left(\frac{c}{a-b}\right)^2 \quad Narrow\ Annulus,\ \frac{b}{a} = 1 \tag{3.59}
$$

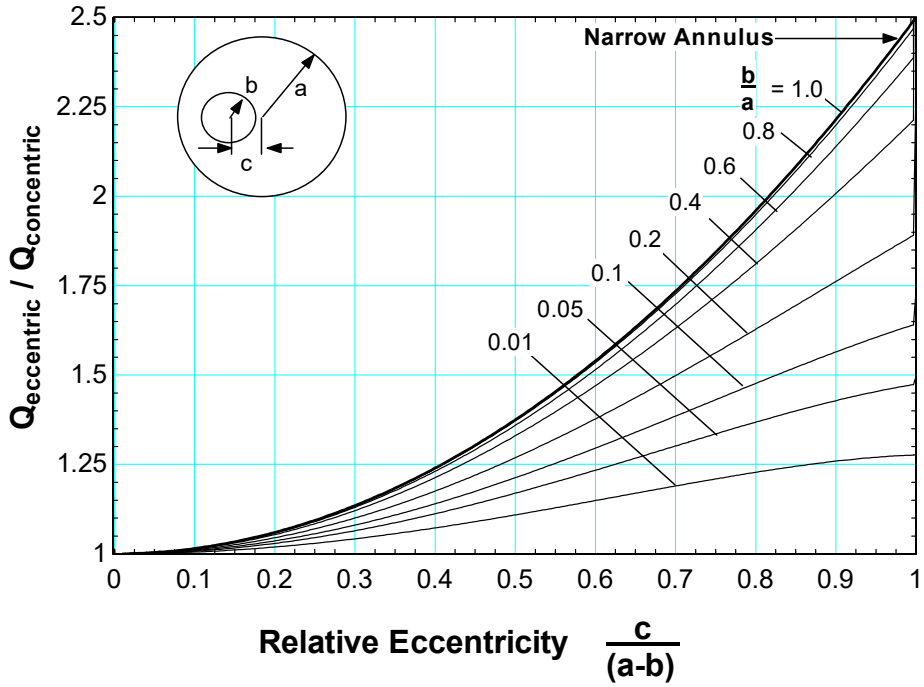

Figure 3.15 Flow rates through eccentric annular gaps relative to concentric annular gaps as a function of relative eccentricity. Also plotted is the relatively simple result lubrication theory.

Piercy et al. (1933) provides a contour plot of the velocity lines through an eccentric annulus where $\frac{b}{a}=\frac{c}{a}=\frac{1}{4}$. A swelling of the velocity profile biased towards the apogee of the seal is noticeable and is reproduced here as Figure 3.16.

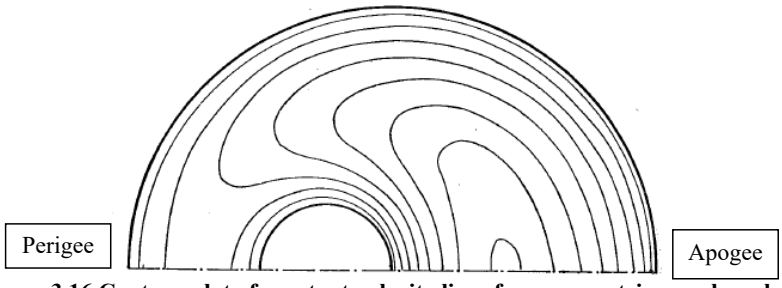

Figure 3.16 Contour plot of constant-velocity lines for an eccentric annulus where b / a = c / a = 1 / 4 ; [referenced from Piercy et al. (1933) and White (2006)]

A less rigorous study through narrow annular gaps only was conducted by Tao and Donovan (1955). The study assumes a frictional factor of the form illustrated in equation (3.60). The primary concern of the investigation was to detail the relative difference in flow rate between narrow eccentric and concentric annular gaps. The final relationship effectively shows that the value of $\frac{Q_{eccentric}}{Q_{concentric}}$ is independent of the constant D used in equation (3.60). Note that the actual value used for the coefficient D will be bounded by the values $D = 64$ and $D = 96$; these values correspond to flow through a circular channel and two infinite plates, respectively.

$$f = \frac{D}{\mathrm{Re}^n} \tag{3.60}$$

The functional form for the expected flow increase over the concentric case due to eccentricity is reported here as equation (3.61).

$$\frac{Q_{eccentric}}{Q_{concentric}} = \frac{1}{\pi}\int_0^{\pi}\left(1+\left(\frac{c}{a-b}\right)\cos\theta\right)^{\frac{3}{2-n}} d\theta, \quad \textit{Narrow Annulus}, \frac{b}{a} = 1 \tag{3.61}$$

The original study details specific techniques that can be used to solve equation (3.61) explicitly for both laminar and turbulent flow conditions. Indeed, in the case of laminar flow where $n = 1$, the exact equation is simplified to a form consistent with equation (3.59). The result is more complicated for the turbulent case where the value $n = 0.25$. The value $n = 0.25$ is attributed to Blasius (1911), corresponding to turbulent flow through a smooth duct. A value of $D = 0.316$ is noted, but not expressly used in equation (3.61). The explicit solution for turbulent flow results in a fairly complicated hypergeometric series. With the advent of modern computers, however, the results for both laminar and turbulent flow are easily obtained numerically in EES as demonstrated in equation (3.62). The results are plotted in Figure 3.17 along with the exact solution obtained for laminar flow by Piercy et al. (1933). Notice that the model developed by Tao and Donovan (1955) follows the trend developed by Piercy et al. (1933) exactly.

$$\frac{Q_{eccentric}}{Q_{concentric}} = \frac{1}{\pi}\,\text{integral}\left\{\left(\left(1+\left(\frac{c}{a-b}\right)\cos\theta\right)^{\frac{3}{2-n}}\right),\Delta\theta,\theta=0,\theta=\pi\right\}\ ...n=\left\{\begin{matrix}1\rightarrow laminar\\0.25\rightarrow turbulent\end{matrix}\right\} \quad (3.62)$$

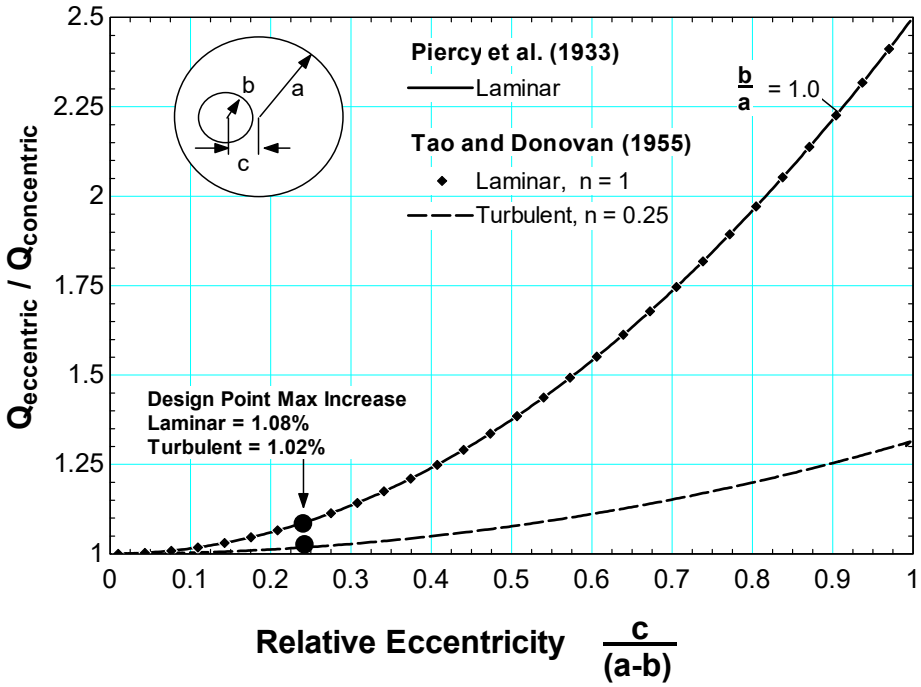

Figure 3.17 Flow rates through narrow eccentric annular gaps where b / a = 1 for both laminar and turbulent regimes; the results obtained from Piercy et al. (1933) and Tao and Donovan (1955) are reported.

Figure 3.17 establishes the clear objective that the effects of eccentricity must be minimized.

Three sources of error are specified in Table 3-6 based on the tolerances of the components used to construct the test section. A great deal of effort has gone into the design of this test section to reduce systematic errors inherent with repeated assembly. Notice that an expected maximum relative eccentricity design point is specified in Figure 3.17. The actual test section design requires a careful assembly procedure in order to meet the specified design point illustrated above. The method is detailed in the next section where only the highlights are demonstrated here.

Table 3-6 Tolerances of components used to minimize eccentricity in the test section

PARAMETER	VARIABLE	VALUE	UNCERTAINTY
Nominal seal diameter	D_{seal}	3.175 mm	+ 2.54 μm
			+10.16 μm
Nominal assembly shaft diameter	$D_{shaft}\|_{assembly}$	3.099 mm	+0.000 μm
			+1.524 μm
Nominal alignment shaft diameter	$D_{shaft}\|_{alignment}$	3.175 mm	+0.000 μm
			+1.524 μm
PARAMETER	VARIABLE	UNCERTAINTY	
Collet total indicated runout	TIR_{collet}	Uncertainty @ Tip	1.016 μm
		Uncertainty @ $4 \cdot D_{shaft}$	3.048 μm

Table 3-6 identifies the tolerances of the components used to align the shaft within the seal to minimize the effects of eccentricity. The test section detailed here simulates a shaft-seal interface by holding a gauge-pin very precisely. The uncertainty due to eccentricity is a byproduct of two major contributing factors in the test section – uncertainty due to available cross-sectional area and uncertainty introduced as a byproduct of the total indicated runout of the collet system used to hold the shaft. Notice that the indicated runout of the collet used in this facility has two rated uncertainties – one at the tip of the collet and the other at 4 times the diameter of whatever it holding. A schematic is provided below in Figure 3.18. This section details the major sources of error in the cross-sectional area and that of the collet system.

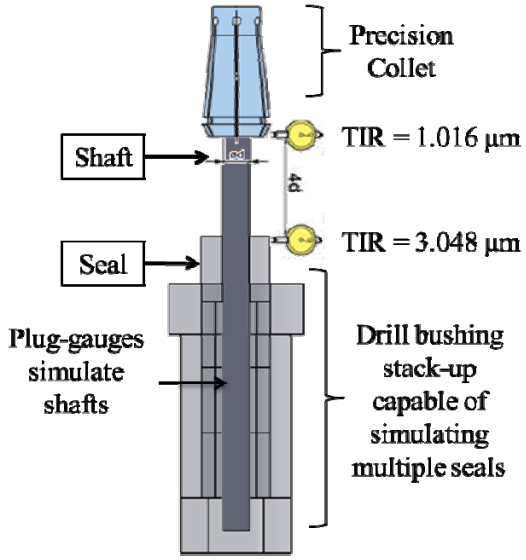

Figure 3.18 Schematic of components used in eccentricity tolerance calculation

3.4.3 Measurement Uncertainty in Cross-Sectional Area

Type X plug go-gauges are used in the facility to simulate the shaft as they have a maximum rated uncertainty on the order of +1.5 µm as noted in Table 3-6. A seal with a comparable rated uncertainty would be ideal; however, it was not possible to acquire such a precise seal at the geometry and tolerances desired. The best available seal interface that could be fabricated was obtained by slicing apart drill bushings that have a maximum rated uncertainty of about +/- 4 µm. The relative impact on the uncertainty of the annular area is demonstrated below as an output from EES shown in Figure 3.20. It is clear that the uncertainty of the seal provides the largest relative error in the shaft-seal interface. Unfortunately, measurement of the inner diameter of the bushing proved to be just as inaccurate as the rated uncertainty from the

manufacturer as demonstrated below in Figure 3.20. Said differently, the discrete nature of the computer pixilation went directly from 3178.4 µm to 3184.7 µm without allowing finer precision in the measurement. As it stands, the lens required to encompass the entire diameter of the seal inside the field of view of a microscope turned out to be just as inaccurate as the tolerance specified by the drill bushing manufacturer. Nevertheless, the uncertainty in the cross-sectional was reduced to about +/-5% based on the nominal conditions identified in Figure 3.19.

Variable±Uncertainty	Partial derivative	% of uncertainty
Ac = 0.4035±0.0194 [mm^2]		
seal = 3.181±0.00381 [mm]	∂Ac/∂ seal = 4.997	96.34 %
shaft = 3.1±0.000762 [mm]	∂Ac/∂ shaft = -4.869	3.66 %

No unit problems were detected.

Figure 3.19 Relative impact of shaft-seal uncertainty on annular area

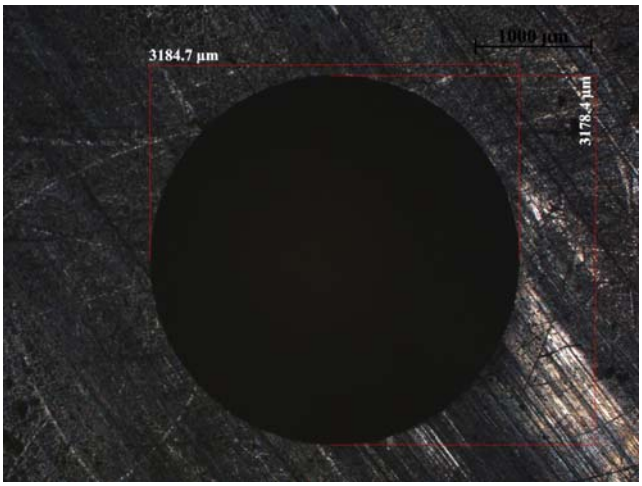

Figure 3.20 Measurements made of drill bushing with microscope proved to be just as inaccurate as manufacturer tolerances

3.4.4 Expected Eccentricity

The uncertainty in the diameter of the seal has the unfortunate effect of also contributing to uncertainty in the eccentricity. In a perfect assembly process, the seal would first be aligned with a shaft of the exact diameter of the seal. This alignment process was crucial in order to effectively "tare" the facility and reduce all other systematic errors in the facility. A degree of uncertainty is introduced in this process, however, as illustrated in Figure 3.21-A. The worst case alignment is demonstrated here, where the minimum shaft and maximum seal diameters based on the tolerances noted in Table 3-6 are shown to result in a maximum eccentricity error of $k_1 = 5.08\mu m$. The result is a worst-case assembly error of the same eccentricity using the smaller diameter shaft noted in Figure 3.21-B. The seal diameter would need to be toleranced more tightly in order to reduce this alignment eccentricity.

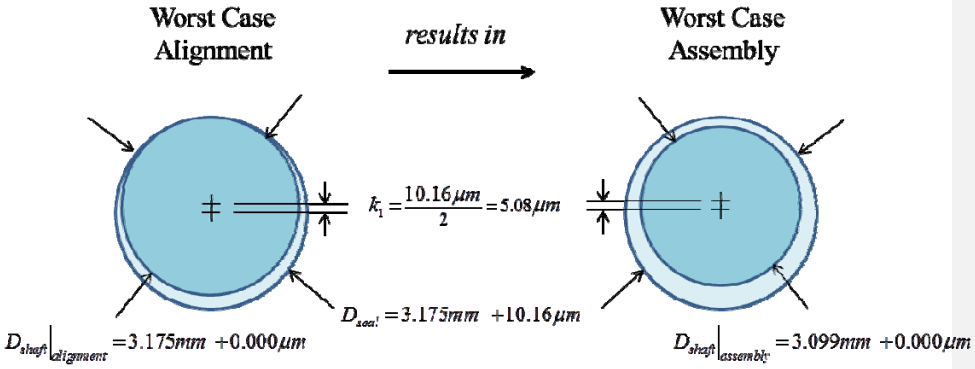

Figure 3.21 Shaft to seal alignment and final assembly process demonstrations; A – alignment pin used to center shaft and seal assembly; B – final assembled position of shaft and seal

The uncertainty in the eccentricity is compounded by alignment issues induced by the clamping mechanism used to hold the shaft in place. In order to align all components with the large shaft as demonstrated in Figure 3.21-A, a tool-holding mechanism had to be used that would allow the shaft in figure *A* to be replaced by the shaft shown in figure *B*. The problem was in locating or developing such a tool-holding mechanism that would hold the shaft as straight as it was when the facility was aligned. The concept is demonstrated in exaggerated fashion in Figure 3.22. Note the induced angular offset incurred when replacing shaft *A* by shaft *B*.

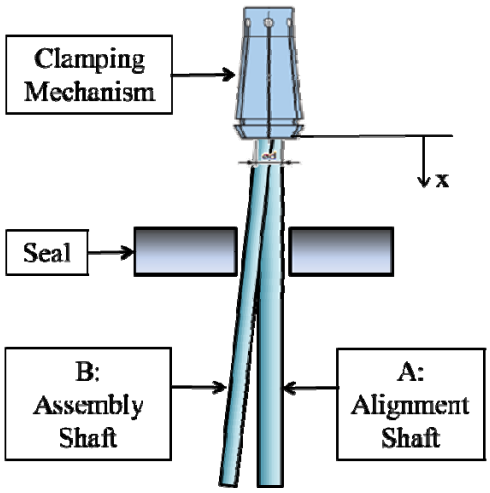

Figure 3.22 Alignment issues attributed to clamping mechanism error

A New Baby collet often used to hold end-mills in micro-machining was integrated into the test facility to limit the effects of this unavoidable error. The final tolerance on the assembly error is represented by the linear equation shown in equation (3.63) as a compilation of the shaft alignment error pictorially described in Figure 3.21 and the clamping mechanism error illustrated

in Figure 3.22 respectively. The shaft straightness is regarded as exact, which is effectively true for a plug gauge.

$$\underbrace{c}_{\text{eccentricity}} = \underbrace{k_1}_{\substack{\text{shaft}\\\text{alignment}}} + \underbrace{mx + k_2}_{\substack{\text{clamping}\\\text{mechanism}}} \tag{3.63}$$

The final step was to estimate the eccentricity introduced as a function of the clamping mechanism. This step is demonstrated in equation (3.64) using the information provided in Table 3-6 and conceptually illustrated in Figure 3.18. The final equation regarding the eccentricity at the nominal conditions listed in Table 3-6 is shown in equation (3.65) and illustrated in Figure 3.23.

$$\begin{aligned} k_2 &= TIR_{collet\,tip} = 1.016\mu m \\ m &= \frac{TIR_{4\cdot D_{shaft}} - TIR_{collet\,tip}}{4\cdot D_{shaft} - 0} = \frac{3.048\mu m - 1.016\mu m}{4\left(3.099mm\right)} = 0.164\,\frac{\mu m}{mm} \end{aligned} \tag{3.64}$$

$$\underbrace{c\big|_{D_{shaft}=3.099mm}}_{\text{eccentricity}} = \underbrace{5.08\mu m}_{\substack{\text{shaft}\\\text{alignment}}} + \underbrace{0.164\,\frac{\mu m}{mm}\left(x_{shaft}\right) + 1.016\mu m}_{\substack{\text{clamping}\\\text{mechanism}}} \tag{3.65}$$

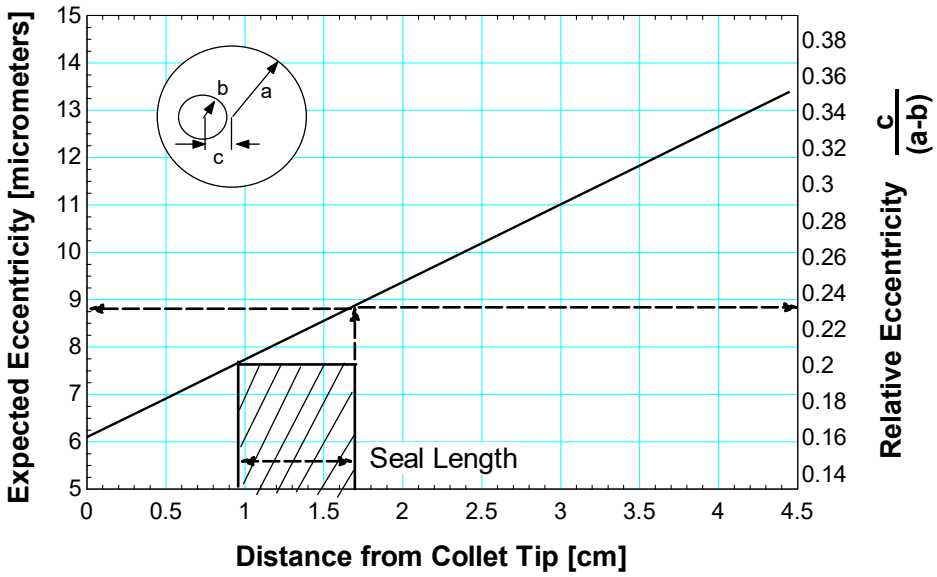

Figure 3.23 Expected eccentricity and relative eccentricity as a function of the distance from the collet tip.

Figure 3.23 illustrates the eccentricity as a function of the distance from the collet tip as defined by equation (3.65). The figure demonstrates the importance of positioning the seal as close as possible to the collet tip. The design specification calls for the seal to be positioned at a distance of about 1 cm from the collet tip. This configuration results in a relatively small expected maximum eccentricity of about 9 μm at the end of the seal. The relative eccentricity, however, is as high as 0.24. The problem is that the annulus between the shaft and the seal is so small that $a-b=\frac{3.175mm}{2}-\frac{3.099mm}{2}=38\mu m$; this small gap facilitates the need for extremely tight tolerances on the equipment required to control the eccentricity. The final result was published in Figure 3.17 where the ratio of $\frac{b}{a}=\frac{3.099mm/2}{3.175mm/2}=0.98$ is effectively unity.

3.4.5 Measured Eccentricity

The expected eccentricity detailed in the previous section was verified optically using the test setup presented in Figure 3.24. The test section was fastened to a fixture designed to clamp down to an optical table. A camera was outfitted with an external light source and a lens with a field of view that could verify the eccentricity in the as-assembled test condition. Alignment stages were outfitted to the camera fixture to provide adjustment of the field of view.

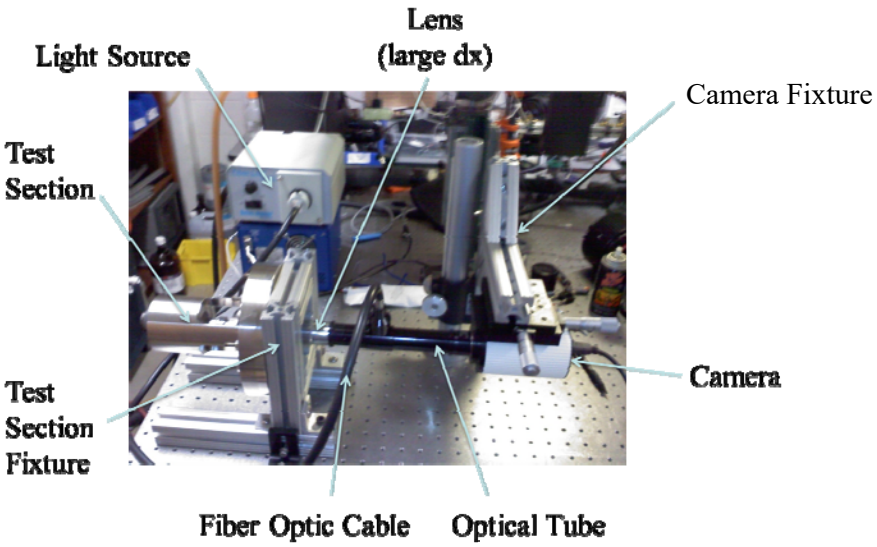

Figure 3.24 Optical setup used to verify the expected eccentricity

Pictures were taken about the shaft-seal interface as it was not possible to capture the entire structure in a single photograph. Several of these raw images are illustrated in Figure 3.26; the

images have been aligned to a background image to provide a visual interpretation of what was desired from this test series.

It was not possible to record images with the shaft and seal significantly out of focus. The images illustrated in Figure 3.26 were developed at the desired distance of $x_{shaft} \approx 1.8cm$ from the collet tip as shown in Figure 3.23, but the shaft had to be clamped farther into the collet tip – the concept is demonstrated in Figure 3.25.

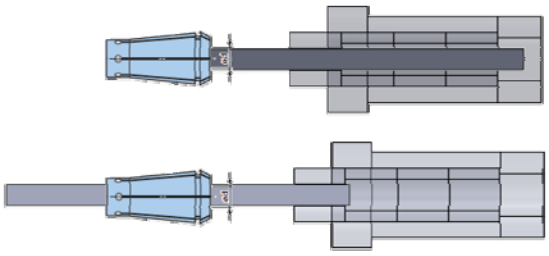

Figure 3.25 Focus solution which allowed imaging of shaft-seal interface at desired distance from collet tip

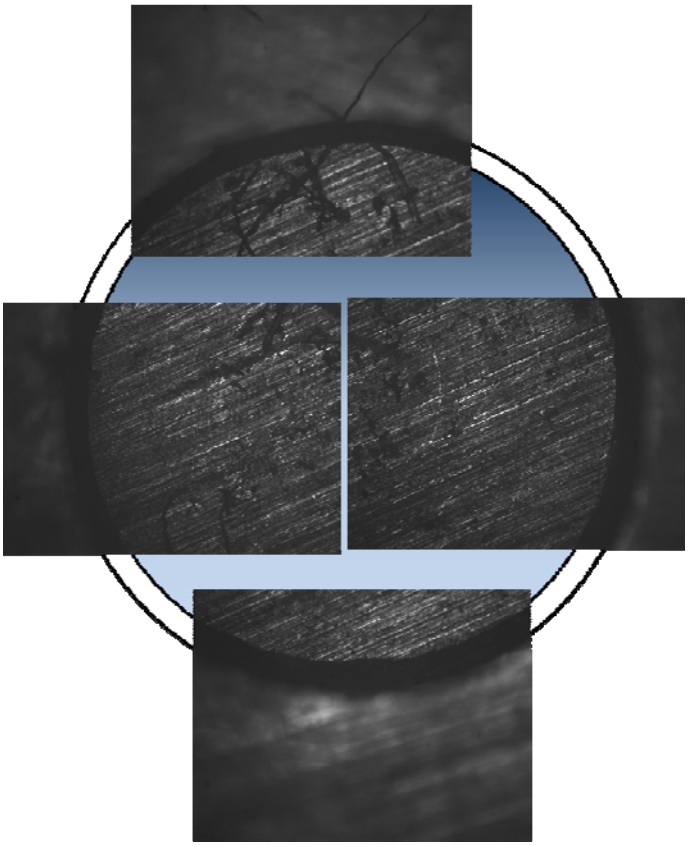

Figure 3.26 Raw images of assembled shaft-seal interface

The images obtained from the test series were difficult to interpret in raw form. The gradient across all the images made it difficult to state with any confidence that the distance from the shaft to the seal was being recorded comparatively. An imaging filter was developed in MATLAB for this process in order to bring the seal more in focus with the shaft and reduce background noise. The filtered images would then be used to deduce the distance from the shaft to the seal at various points around the shaft across all images taken. The idea was that if the

exact same process was applied to all images, the error introduced by the user recording the distance from the shaft to the seal would be the same for all measurements and therefore cancel from a measurement of the eccentricity. The program is conceptually illustrated in the flow chart detailed in Figure 3.27 and recorded in Appendix A: MATLAB Image Filtering Program.

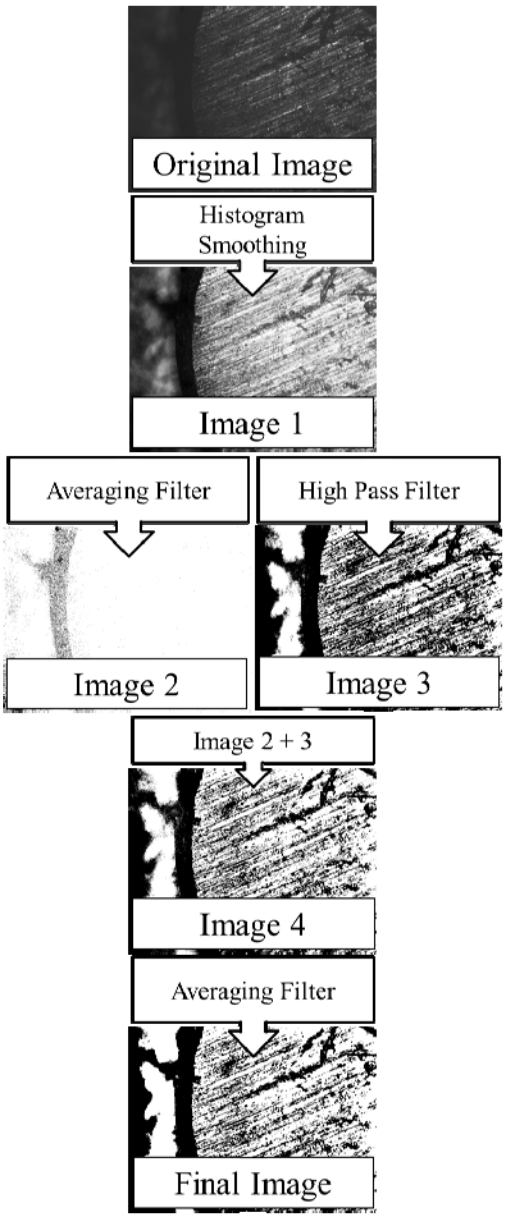

Figure 3.27 Flow chart of MATLAB image filtering program

The methodology used to develop the filtering program is as follows:

- A histogram smoothing technique is applied in order to extract the background image and increase the contrast throughout. This image is stored as Image 1.
- A special 2-d digital averaging filter is applied to Image 1 to blur the image and save only the elements of the image with the highest contrast. This image is stored as Image 2.
- A high pass filter is applied to Image 1 by using the built in fast-fourier-transform tools in MATLAB.
    - The 2-d fast fourier transform of the image is taken and shifted such that image information in the frequency domain with zero-frequency components are shifted towards the center of the spectrum. This saved as sub-image A.
    - A meshgrid the size of the sub-image A is constructed with a value of 1. A circle made of all 0's is then deleted from the center portion of the meshgrid to construct a convolution image that will delete the zero-frequency components in sub-image A. The result of the operation is stored as sub-image B.
    - With the zero-frequency components deleted from sub-image B, an inverse fast-fourier shift is taken of the image. An inverse fast fourier transform is taken of the result to obtain the image in the frequency domain with all the zero-frequency components deleted. The overall result is a contrasted image in the spatial domain.
    - The final sub-image is saved as Image 3.
- A weighted sum of Image 2 and Image 3 is developed and stored as Image 4 to recover some of the less severely contrasted elements of the original image.

- The 2-d digital averaging filter is applied to Image 4 to highlight the contrast further and bring more of the background image into the forefront. The result is stored as the final image.

A pixel counting program was used on the final images to count the number of pixels from the shaft to the seal at various intervals around the shaft. A figure detailing the contrast of the raw images illustrated in Figure 3.26 to the final images obtained from the filtering program is detailed in Figure 3.28.

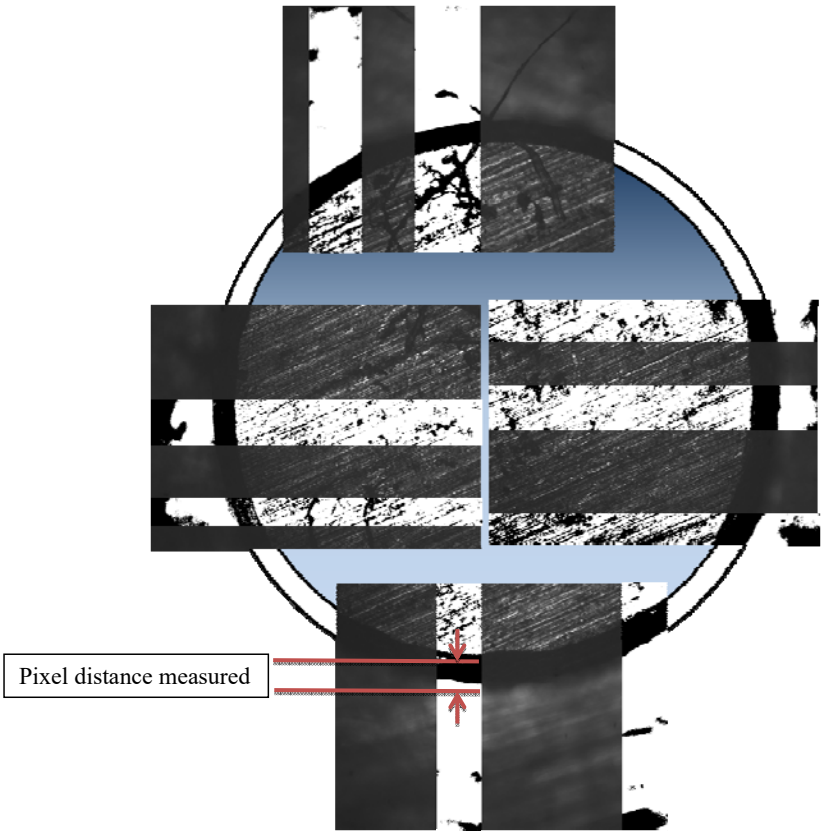

Figure 3.28 MATLAB filtered images placed over raw images of assembled shaft-seal interface

The results obtained from the pixel counting program are shown as a function of the pixel distance from the center shaft to the seal as conceptually demonstrated above in Figure 3.28. Pixel distances were measured at various locations around the shaft across all images taken. The results are shown in Figure 3.29. Two image results are presented in the figure where the seals and the shaft are in the image's focus, respectively. The data taken with the seals in focus, proved to be more consistent.

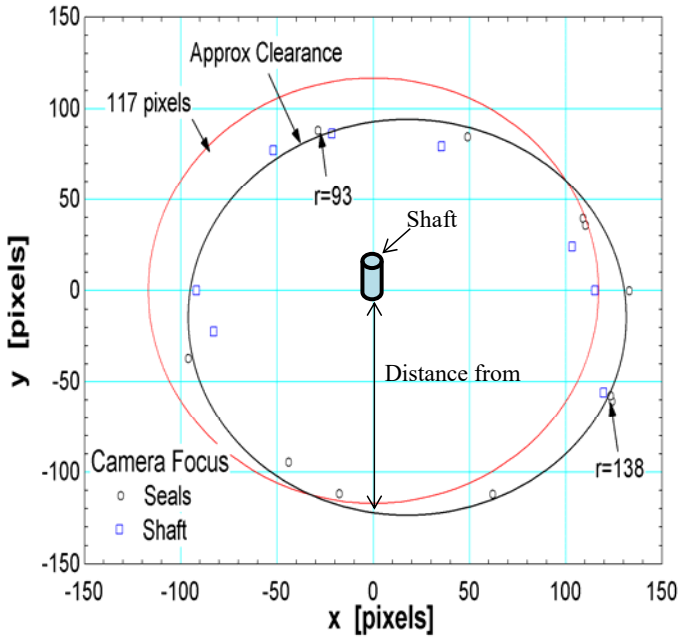

Figure 3.29 Results obtained from pixel counting program detailing the pixel distance from the center shaft to the seal.

An estimate of the relative eccentricity was determined based on the values provided in equation (3.66). Based on this analysis, the expected eccentricity detailed in Figure 3.23 as specified by the manufacturer's tolerances is within the desired eccentricity in the assembled configuration.

Relative eccentricity

$$\frac{c}{a-b} = \frac{\max\left(abs\left(\max - avg\right) + abs\left(\min - avg\right)\right)}{avg} \approx \frac{\max\left(21+24\right)}{117} \approx 0.205 \tag{3.66}$$

3.5 Instrumentation Uncertainty and Facility Control

The instrumentation utilized in the design of this test facility was selected to minimize the uncertainty of key variables at test conditions. A description of each of the components selected for this experiment is provided in this section. The relative uncertainty attributed to each component at test conditions is provided in Table 3-7.

Table 3-7 Instrumentation uncertainty at nominal conditions

PARAMETER	VARIABLE	VALUE	UNCERTAINTY
Inlet Density	ρ_{inlet}	200 – 800 kg/m^3	0.2 kg/m^3
Inlet Pressure	P_{inlet}	7.33 – 14 MPa	30000 Pa
Outlet Pressure	P_{outlet}	1.4 – 14 MPa	30000 Pa
Mass Flow Rate	$\dot{m}_{test-section}$	0.01 – 0.03 kg/s	0.000015 kg/s

3.5.1 Pressure Transducers

Instrumentation Configuration

Siemens SITRANS P 7MF4332 pressure transducers are used in this experiment. The transducers are rated to a maximum 40 MPa but are calibrated with the NI 9216 computer DAQ card used in this experiment up 14 MPa. The relevant information for the pressure transducers is listed in Table 3-8.

Table 3-8 Pressure transducer configuration summary

PARAMETER	VALUE
Siemens Absolute Pressure Transducer	
Device Accuracy	0.075%
Full Span	40 MPa
Application Full Span	14 MPa
Sensor Output	1V to 5V
NI 9215 DAQ Card	
Bits	16
Range	-10V to 10V
NI MAX configuration	
Full Span	14 MPa
Limits	1V to 5V
Summary	
Transducer Uncertainty	30 kPa
Transducer Quantization (MAX conf.)	3.5 MPa/V
Least Significant Bit Change	305μV/bit
DAQ Card Limitation	1.07 kPa/bit

The information presented in Table 3-8 shows that the uncertainty of the instrumentation is about 30 kPa. The National Instruments Measurement and Automation Explorer (MAX) is configured to read a voltage signal from 1V to 5V corresponding from 0 to 14 MPa respectively. This MAX configuration provides a 1.07 kPa/bit resolution compared to the transducer uncertainty of 30 kPa. Based on this information, the bit resolution of the NI 9215 DAQ card provides ample resolution for the pressure transducers used in this experiment.

Instrumentation Control

The facility is controlled by a LabView file which uses an integrated PI-controller to manipulate the inlet pressure into the facility. The pressure is manipulated by an actuated valve which

controls the excess flow loop of the test facility. An NI MID-7602 motor controller drives an Oriental Motor PK246PDAR26 stepper motor. The instrumentation is shown in Figure 3.30.

A **B**

Figure 3.30 Components used to control test facility: A – NI MID-7602 motor controller; B – Oriental Motor PK246DAR26

The motor is attached to a SS-31RS4 valve – refer to Figure 3.13 – with a MCS200506 flexible motor coupling. The layout of this system is provided in Figure 3.31. The valve stem is attached to the flexible motor coupling via a spline shaft which allows the valve stem to rise as a function of the number of turns. The valve-motor assembly sits on a platform which is welded together to form a solid base for the rest of the assembly.

A Labview VI was configured to read in the pressure output by the inlet pressure transducer and then update the location of the valve depending on the set point of the desired inlet pressure. It is important to note that this portion of the VI must only be turned on when the pressure is near the desired set point. The procedure for this sub-system dictates that the pressure be within +/- 150 kPa before it is turned on. The valve will then make fine adjustments to the excess flow loop allowing more or less mass to bypass the test section. Steady state does not last long with the

current Joy compressor as a large amount of carbon dioxide is lost (i.e. the compressor was not designed for this application) during a single test run of about 15-20 minutes.

There are two valves which allow pressure to flow through the excess loop as was detailed in Figure 3.10. To reach system pressure, close both of these valves at the beginning of a test run and allow the pressure on the high pressure side to build up to the desired test section inlet pressure. Once the system has approximately reached the required test section inlet pressure, manually open the automated valve until the pressure levels off. *Make sure the output signal on the MID-7602 is suppressed or you will not be able to turn the valve!*

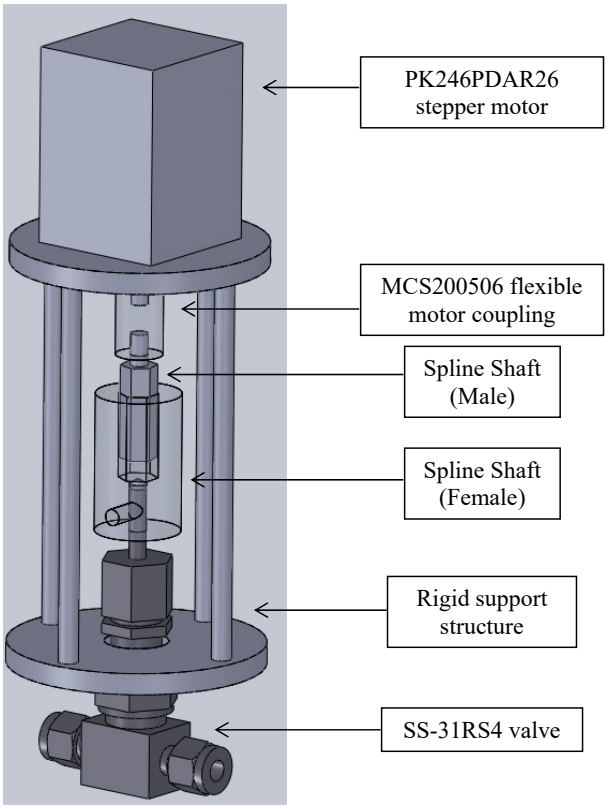

Figure 3.31 Automated valve which control test facility inlet pressure

3.5.2 Temperature

Instrumentation Configuration

Thermocouples are used to monitor and record the temperature at various locations in the facility. Type E thermocouples are used throughout the facility to monitor the temperature of the flow as they offer high resolution and work well at temperatures below 0°C. The pertinent

information is summarized in Table 3-9 and further illustrated in Figure 3.32 which shows the expected error based on the manufacturer's data for Type E thermocouples.

The facility also uses Type K thermocouples to monitor the heater surface temperatures. The Labview VI monitors these temperatures and ensures that they do not become excessively high such that the heater wires start to melt. If the temperatures pass a certain threshold, the VI will shut them off automatically based on the maximum desired temperature specified by the user.

Table 3-9 Temperature sensor summary

PARAMETER	VALUE
Type-E Thermocouples	
Resolution	68μV/°C
Temperature range	-40 to 800°C
Type-K Thermocouples	
Resolution	41 μV/°C
Temperature range	0 to 1100°C
NI 9213	
Bits	24
Range	-78.125mV to 78.125mV
Expected Error (Type E)	0.8°C – Figure 3.32~~Figure 3.32~~: Typ (High res)
Total Type-E Error	1°C

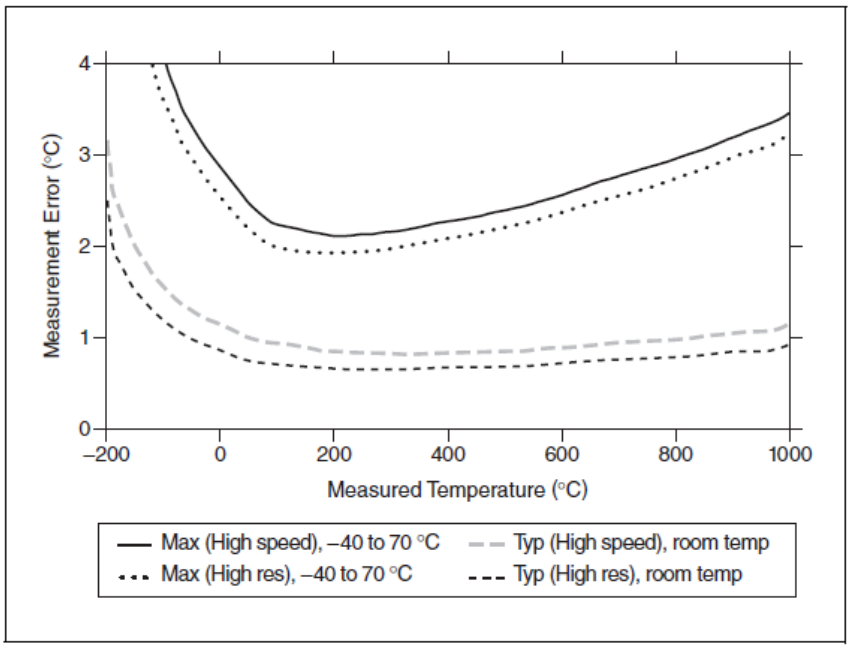

Figure 8. Thermocouple Types T and E Errors

Figure 3.32 NI 9213 Type E thermocouple measurement error illustrated to require high resolution input mode

The error in the temperature at the cold junction is shown to contribute greatly to the uncertainty of the thermocouples based on Table 3-9. There are 16 input channels and only one thermistor integrated into the NI 9213 card. National Instruments makes a note that nearby heat sources such as adjacent modules may cause errors in thermocouple measurements by creating a non-uniform temperature distribution across the reference terminal block. The temperature error will then increase as a function of the physical distance of the channel in question from the reference thermistor location. To decrease the severity of this effect, the NI CompactDAQ was installed next to one of the Safety and Instrumentation Panel Box inlets shown at the bottom of Figure 3.33 and Figure 3.34. Three 117 CFM axial fans were installed on the top of the box to draw

high velocity cool air over the NI 9213 thermocouple module as well as to dissipate the heat generated by the 240V heater relays. The NI 9213 module was also installed away from the other modules used in the CompactDAQ housing. The entire system was calibrated with the fans turned on in order to ensure repeatability.

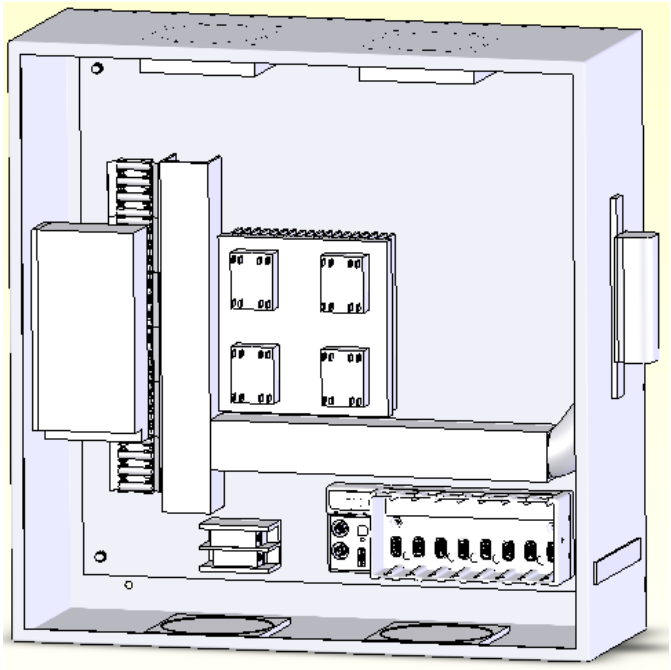

Figure 3.33 Layout of safety and instrumentation panel box

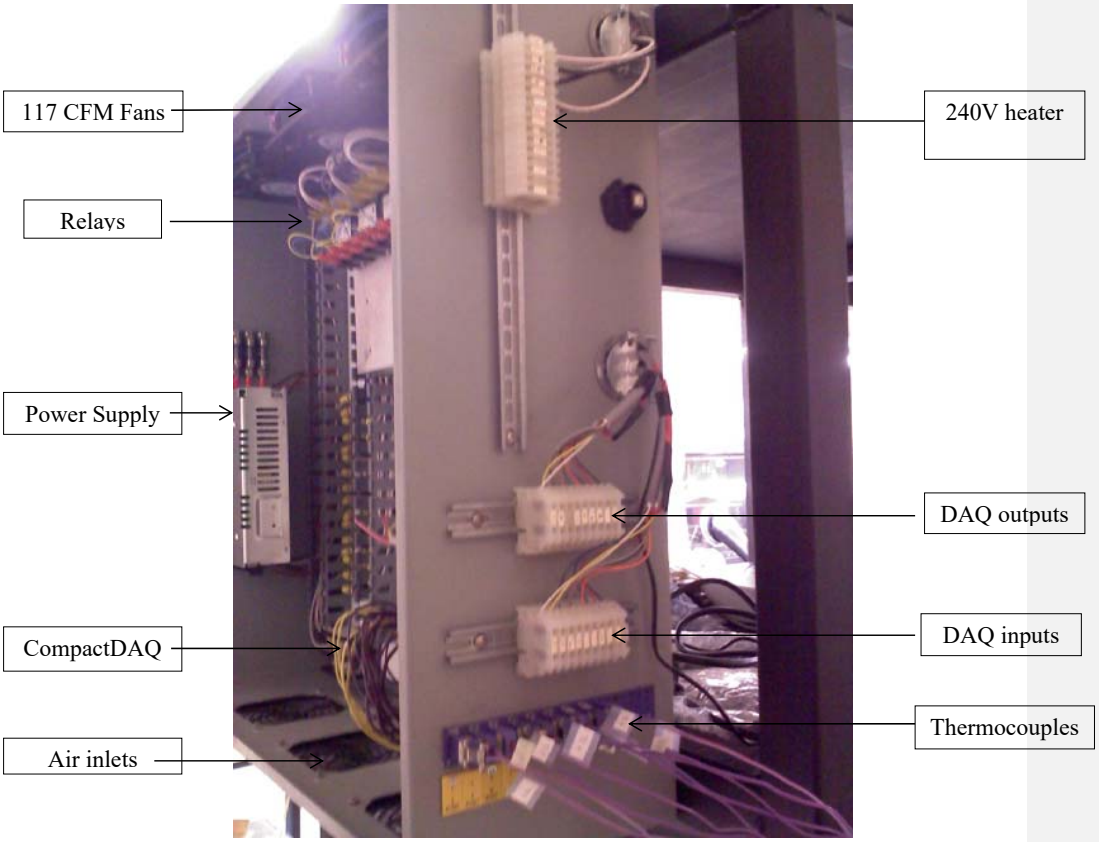

Figure 3.34 Safety and instrumentation panel box

The safety panel box was constructed to centralize the instrumentation and the 240V electrical lines which power the heaters.

Instrumentation Control

Temperature is regulated by two mechanisms in this facility. The first mechanism is the PID-controller implemented in Labview which continually monitors and adjusts the power sent to

tube surface heaters implemented throughout the facility. The concept is explained in Figure 3.35 and Figure 3.36 where a wall output signal 240V, 60Hz signal is turned on and off by a computer controlled relay.

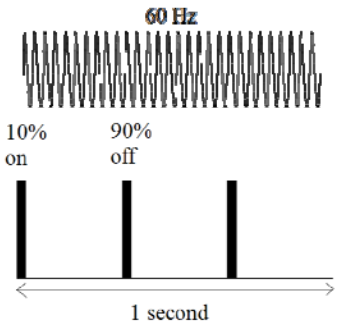

Figure 3.35 Relay controlled output signature of heaters

Figure 3.35 shows a 60Hz signal being continually cycled on and off over the course of 1 second. The energy output from the relay is on a total of 10% of the time and off 90% of the time in this example. The relay is not restricted to this limit however and by varying the ratio of the time the relay is on to the time the relay is off, one can adjust the integrated energy output dissipated by the heaters.

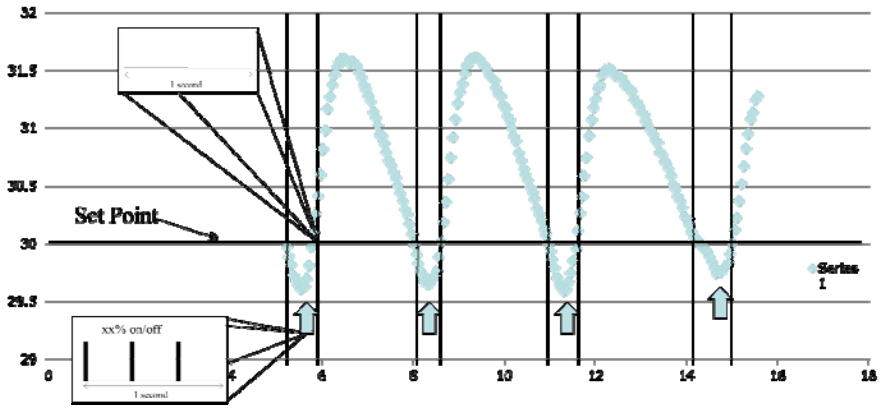

Figure 3.36 Description of PID operated heaters

Figure 3.36 shows a figure of a PID controller which has not been tuned for purposes of exaggerated demonstration. The set point in the figure indicated the desired temperature. At the point that the temperature falls below the set point, the total time the heaters are on quickly ramps up to a peak percentage which increases the temperature of the incoming stream. The power input into the stream is too great however and the flow overshoots the set point. The controller being insufficiently tuned quickly decreases in power output to effectively 0%. The incoming flow must then dissipate the thermal energy which has been stored in the stainless steel tubing. As times goes on, the energy content of the stainless steel tubing decreases and the flow again overshoots the set point. The heaters turn on again and the process repeats.

The problem discovered with this method was that the sampling time of the thermocouples interfered with the ability of the heater to respond quickly enough to flow temperature fluctuations. As was illustrated in Figure 3.32, the thermocouple temperature error increases with sampling rate (i.e. high speed vs. high resolution). Figure 3.37 demonstrates that the timing

modes if using all channels differ by a factor of 1 to 75 samples per second for high resolution and high speed respectively. The maximum sampling rate when operating in high resolution mode is 1 sample per second. It becomes exceedingly difficult to respond effectively to small temperature fluctuations in the flow when operating at such large time scales. The upstream heater was therefore decommissioned to only respond to large scale changes in temperature.

The heaters controlled in the two-phase region were unaffected by sampling time issues. Those heaters effectively need to operate at 100% duty cycle in order to cycle carbon dioxide continuously. The heaters are limited only by the melting point of the heating tape material rated to 480°C. The Labview VI will automatically decrease the power they dissipate if the surface temperature becomes too high.

Timing Mode	Conversion Time (Per Channel)	Sample Rate* (All Channels†)
High-resolution	55 ms	1 S/s
High-speed	740 µs	75 S/s

* If you are using fewer than all channels, the sample rate might be faster. The maximum sample rate = 1/(*Conversion Time* × *Number of Channels*), or 100 S/s, whichever is smaller. Sampling faster than the maximum sample rate may result in the degradation of accuracy.
† Including the autozero and cold-junction channels.

Figure 3.37 NI 9213 Timing mode disclaimer

3.5.3 Flow and Density

Instrumentation Configuration

Figure 3.38 shows the Rosemount CMF010 coriolis flow meter incorporated in the test loop. The coriolis flow meter offers exceptional independent resolution of the density and mass flow rate. A summary of the design configuration is provided in Table 3-10.

Figure 3.38 Rosemount CMF-010 Coriolis flow meter

Table 3-10 Coriolis flow meter summary

PARAMETER	VALUE
CMF010 Flow Meter with 2200 Transmitter	
Mass Flow Rate Accuracy	0.05%
Flow Rate Full Span	108 kg/hr
Density Accuracy	+/-0.2 kg/m^3

Density Full Span (MAX config)	1000 kg/m^3
Sensor Output	1V to 5V
NI 9215 DAQ Card	
Bits	16
Range	-10V to 10V
Least Significant Bit Change	305μV/bit
Summary	
Mass Flow Rate Uncertainty	0.054 kg/hr
Flow Rate Quantization	27 (kg/hr)/V
DAQ Card Limitation	0.008235 (kg/hr)/bit
Density Uncertainty	0.2 kg/m^3
Density Quantization	200 (kg/m^3)/V
DAQ Card Limitation	0.061 (kg/m^3)/bit

The uncertainty of the Coriolis flow meter is about 0.054 kg/hr and 0.2 kg/m^3 as reported in Table 3-10. The NI 9215 DAQ card quantization resolution is limited to 6.5 and 3.27 times the uncertainty of the input signals and provides adequate bit resolution.

3.5.4 Uncertainty of Isentropic Flow at Nominal Test Conditions

The uncertainty of the test loop where flow is expanded through an orifice from a nominal upstream condition of 7.6 MPa and 500 kg/m^3 is detailed in Figure 3.39 and Figure 3.40. Figure 3.39 seems to illustrate that the instrumentation uncertainty is small compared to the total uncertainty which takes into effect cross-sectional geometrical conditions. The problem with this figure is that it does not clearly illustrate how important uncertainty in the pressure ratio is to total uncertainty.

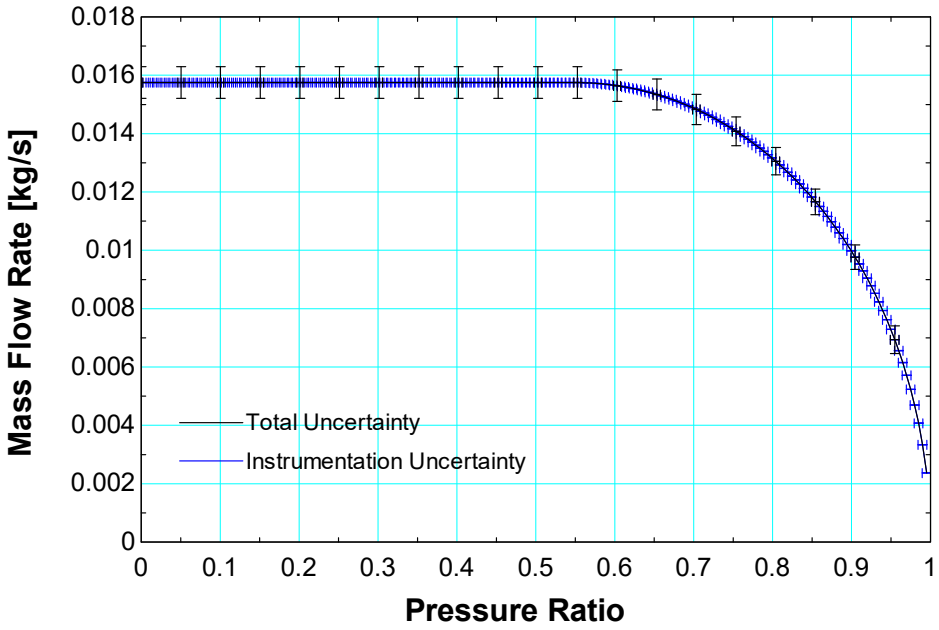

Figure 3.39 Uncertainty at nominal upstream test conditions of 7.6 MPa and 500 kg/m^3

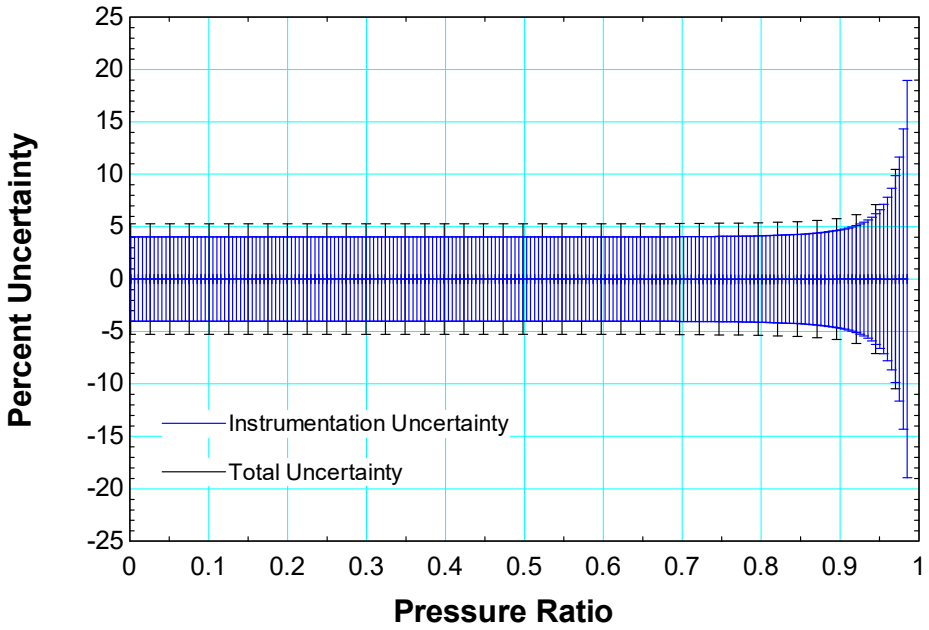

Figure 3.40 Percent uncertainty at nominal upstream test conditions of 7.6 MPa and 500 kg/m^3

A more interesting perspective of the facility uncertainty is illustrated in Figure 3.40. Notice that the facility maintains about +/-5% uncertainty throughout most of the range of pressure ratios desired when operating at a nominal upstream value of 7.6 MPa and 500 kg/m^3. Two regions are identified from the figure. In the first regime, both geometric and instrumentation uncertainty are important. The second regime is shown on the right hand side of Figure 3.40 where instrumentation error becomes an issue. In this limit, the pressures measured by the pressure transducers begin to approach one another which facilitates higher relative uncertainty. The uncertainty attributed to the mass flow meter also begins to increase as the flow rate approaches a value of 0 kg/hr.

3.6 Test Facility Design

The test facility was designed to cycle carbon dioxide through the test section continuously. The following section highlights the unique design elements which were considered in the fabrication of this test facility.

Sections 3.6.1 and 3.6.2 document the analysis and construction methodology employed in the design of the test section. The ideas which facilitated this design were developed in Sections 3.2 through 3.4.

Sections 3.6.3 details the two-phase recovery system which was used to cycle gaseous carbon dioxide through the compressor.

3.6.1 Test section assembly procedure

Section 3.2 and 3.3 provided a basis for the properties the facility would need to support and in what quantities. It was noted that the facility would need to accommodate high pressure gradients as well as large flow rates. This information was compounded by the ideas expressed in Section 3.4 where it was illustrated that limiting geometrical uncertainty was crucial to facility performance.

The goals outlined for the test section are provided below as well as noted in Figure 3.41.

- Accommodate high pressure gradients
- Support multiple seal configurations
- Limit uncertainty due to the design variable shown
- Encapsulate design in a pressure vessel shroud

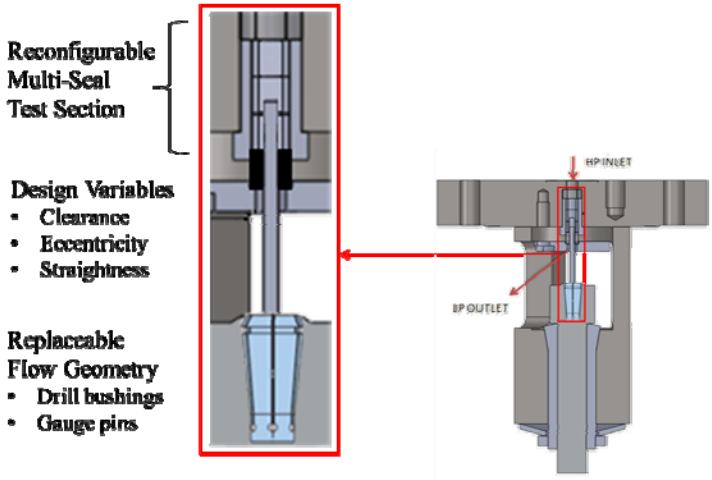

Figure 3.41 Design variables considered in the design of the test section

The alignment process used to simulate the shaft and seal interface is detailed here. The uncertainty in the eccentricity requires that the procedure detailed here be followed precisely in order to limit three-dimensional flow conditions.

Collet Holder Sub-Assembly

The Collet Holder Sub-Assembly is detailed in Figure 3.42. The design uses a multiple stage collet system in order to achieve proper alignment of the assembly gauge pin shown at the bottom. It is very important to use the assembly gauge pin with a diameter 3.175mm (0.125in) in this initial sub-assembly.

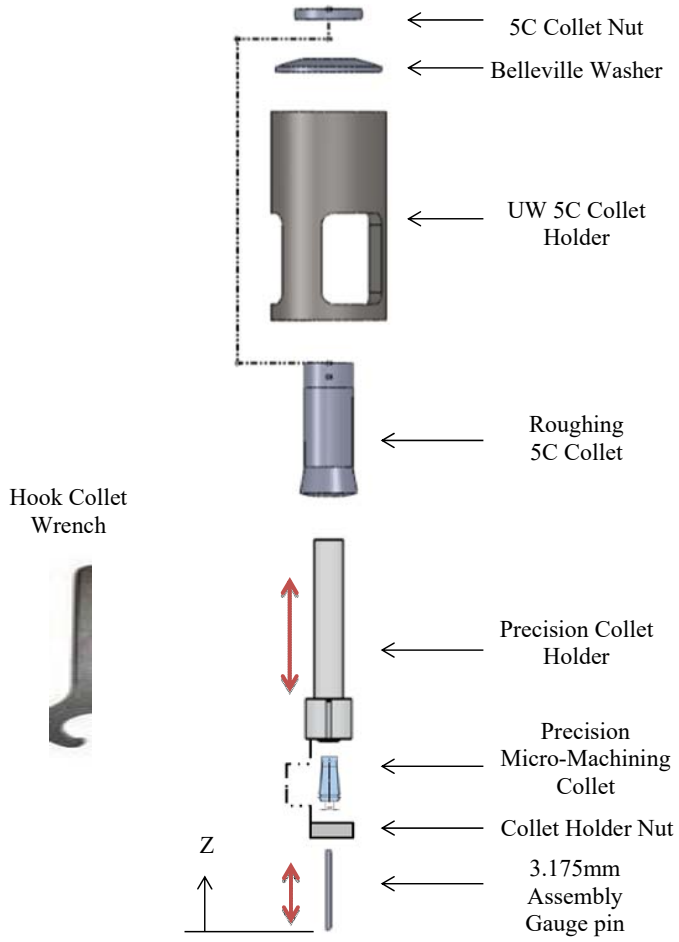

Figure 3.42 Assembly procedure of Collet Holder Sub-Assembly

The dashed lines in the figure represent the components which are screwed together in order to provide a clamping mechanism for dependent child components. Tightening the Collet Holder Nut requires the use of the Hook Collet Wrench also shown in the figure. The child components are illustrated in the figure with red up and down arrows noting the flexible parent-child interface in the axial Z-direction. The gauge pin and precision collet holder are free to move in the axial direction and allow the final assembly the ability to support multiple seal configurations. Figure 3.43 illustrates one particular configuration of this sub-assembly.

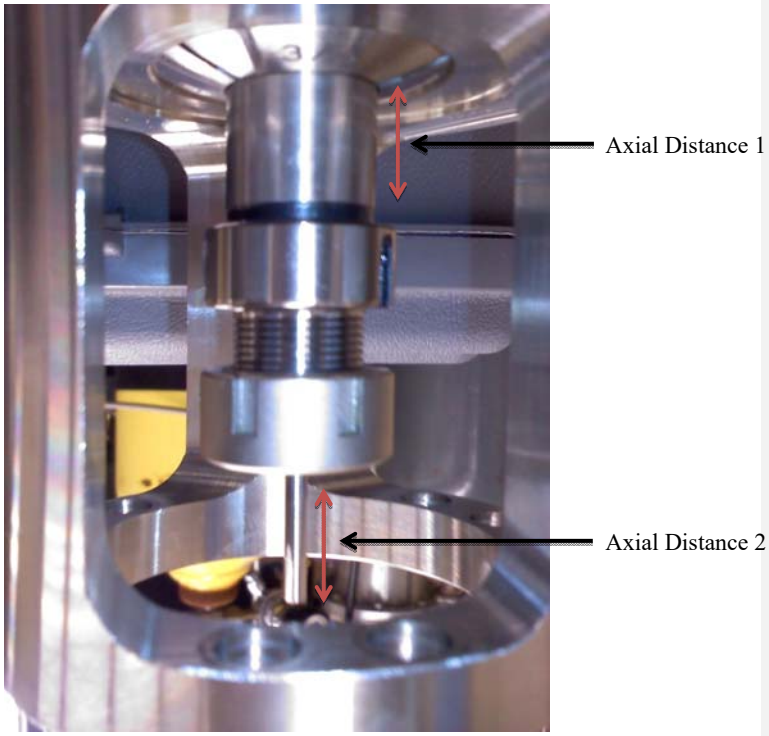

Figure 3.43 Collet holder sub-assembly shown in configured state with alignment gauge pin attached

Figure 3.43 illustrates the Collet Holder Sub-Assembly configured to support one seal. The red up and down arrows which were included in Figure 3.42 are shown here to provide a visual aid of the flexible interfaces in the sub-assembly. Notice that the sub-assembly was designed to accommodate multiple seals by skewing the relative distances between the axial distances shown in the figure. Axial distance 1 may be reduced while simultaneously increasing axial distance 2 to provide up to 4 cm of axial depth available for seal stacking. The uncertainty in the annular area based on the axial depth was shown in Figure 3.23.

Shaft-Seal Sub-Assembly

The Shaft-Seal Sub-Assembly is illustrated in Figure 3.44. The Collet-Holder Sub-Assembly is combined with a stackup of drill bushings which simulate shaft seals. A seal clamp is used to bolt the seal-stackup to the Test Section Flange as shown in the figure.

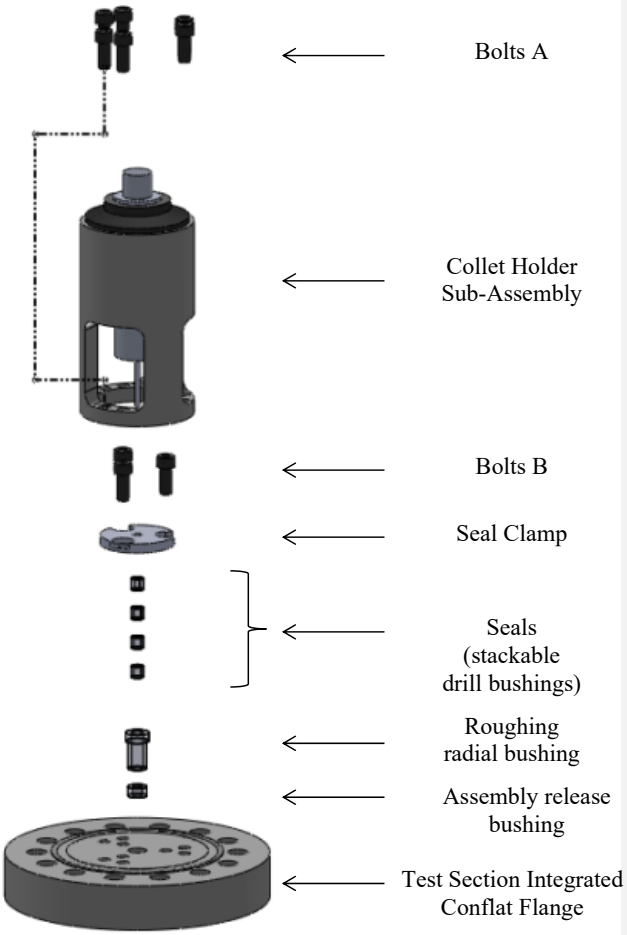

Figure 3.44 Assembly procedure of Shaft-Seal Sub-Assembly

Bolting the configuration in the proper order is crucial to limiting uncertainty in the final assembly. The inner bolt pattern is used to clamp the seal-stackup to the flange as demonstrated in Figure 3.45. The figure shows a stack-up of the assembly release bushing, roughing radial bushing, three 7.938mm ID seal spacers, one 3.175mm ID seal, and seal clamp mated to the test

section flange. It is very important to leave this stack-up loosely bolted together (Bolts B in Figure 3.44) in this step in order to align all the seals with the 3.175mm gauge pin shown at the bottom of the Collet-Holder Sub-Assembly in Figure 3.42 later. Use enough copper lubricant on Bolts A and B to prevent galling as shown in Figure 3.44.

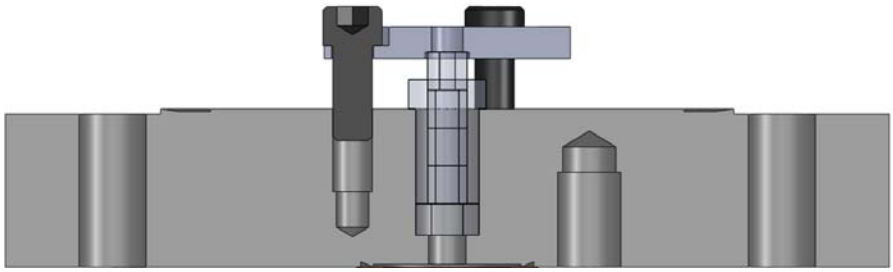

Figure 3.45 Conflat Flange seal-stackup bolting configuration

The Collet Holder Sub-Assembly from Figure 3.42 is then bolted to the outer bolt pattern of the Test Section Flange as depicted in Figure 3.46. The outer diameter of the seal clamp and the inner diameter of the 5C Collet Holder from Figure 3.42 should just clear with the gauge pin inserted into the center portion of the seal stack-up configuration. The final configuration of this assembly step is shown here as Figure 3.46. Notice that there is effectively zero clearance between the alignment gauge pin and the top seal shown in the figure; this alignment procedure is crucial to meeting the stringent uncertainty specifications referenced in Section 3.4.4 and illustrated in Figure 3.21-A.

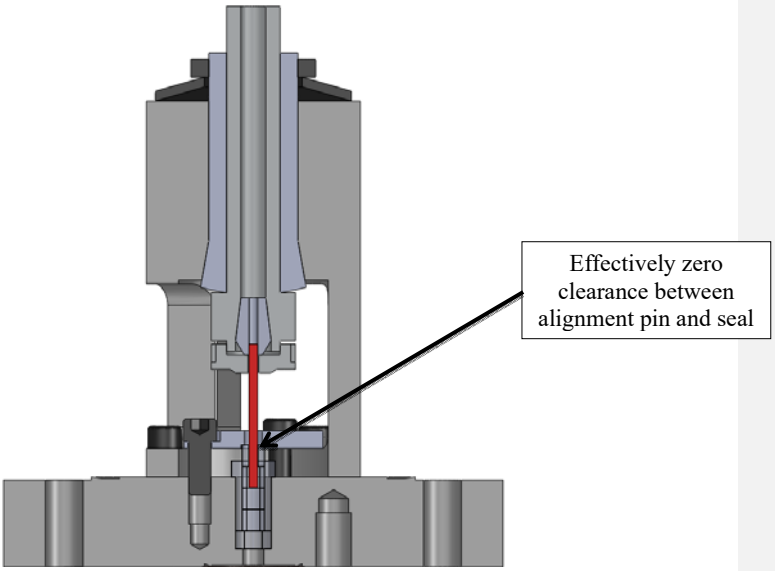

Figure 3.46 Shaft-Seal Sub-Assembly with 3.175mm gauge pin used to align multiple seals; shown here aligning only one seal

Once the Shaft-Seal Sub-Assembly shown in Figure 3.46 has been loosely bolted together to form the configuration shown, tighten Bolts A as Figure 3.44 to the flange while leaving Bolts B loose. In this fashion, the alignment pin will become a fixed reference centering point. The seals with then automatically align themselves to the centering pin. Tighten Bolts B to fix the seals in place about the alignment pin.

The next step requires considerable patience and is the most difficult step of the process. The objective is to remove the alignment pin and replace it with a small diameter gauge pin in order to simulate the shaft-seal clearance.

The process requires the Hook Collet Wrench Figure 3.42, tweezers, and a hammer. Untighten the Collet Holder Nut from Figure 3.42 with the Hook Collet to free the Precision Micro-Machinging Collet. The collet will stay stuck inside the Precision Collet Holder; stick the tweezers down the bore-hole of the Collet Holder to use as a hammer punch. Lightly tap on the tweezers with the hammer to completely free the collet. The alignment pin should be free to move inside the assembly at this point. It will be necessary, however, to use the tweezers, light hammering, and gravity to take the alignment pin out of the assembly completely.

Insert the desired shaft gauge pin into the assembly through the exposed hole on the backside of the Test Section Flange. Use the tweezers to position the shaft inside the collet. Finally, tighten the Collet Holder Nut with the Hook Collet. The final configuration of the Shaft-Seal Sub-Assembly is shown in Figure 3.47.

Figure 3.47 Shaft-Seal Sub-Assembly

Test Section Final Assembly

The final step in the test section assembly procedure is detailed in Figure 3.48. Note that the Pressure Vessel Shroud is fixed to the actual test facility. Copper gaskets are used to seal the enclosure together noted in the figure as Cu Gasket A and B. Grade 9 bolts are used in the facility detailed as Bolts C and D. A High Pressure Inlet Cap allows the Test Section Flange to interface with standard Swagelok connections.

Perhaps the most deceptive connection of the assembly is the Type-E Thermocouple which must be fastened to the assembly last. The thermocouple fits inside one of the windows of the 5C Collet Holder illustrated in Figure 3.42. *Be sure not to tighten Bolts D without first checking that the thermocouple will mate together with the assembly.* If the thermocouple does not go in completely, rotate the Shaft-Seal Sub-Assembly about its center axis until one of the windows in the 5C Collet Holder aligns with the thermocouple. The concept is demonstrated in Figure 3.48.

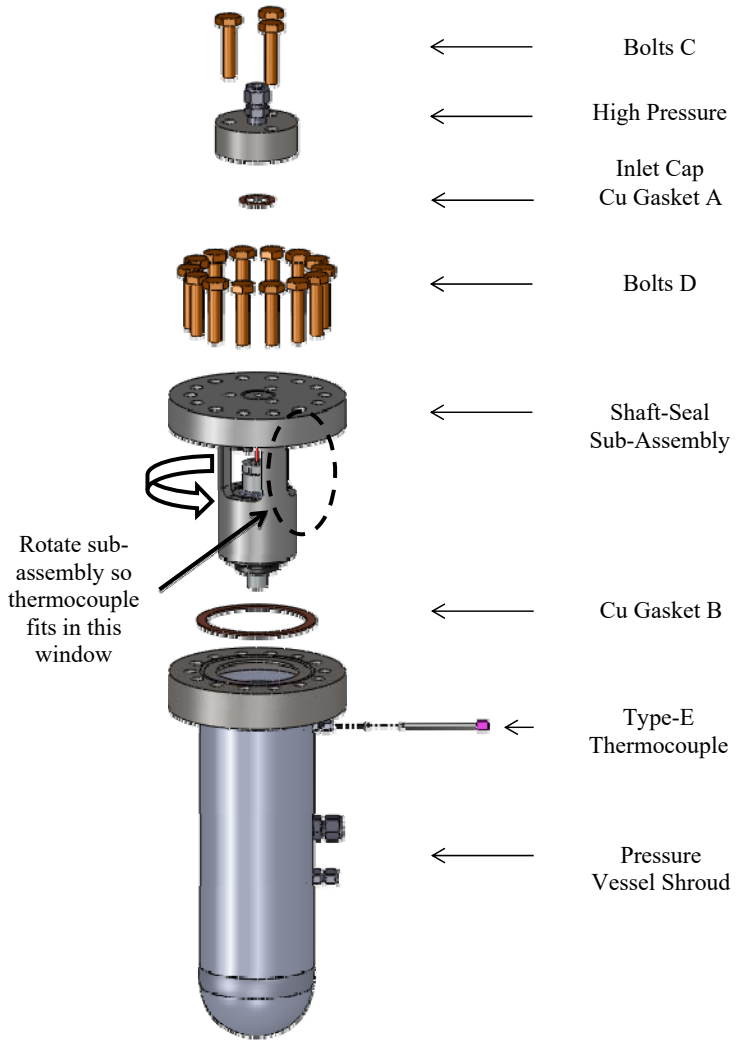

Figure 3.48 Final assembly procedure for configuring test section

The final configuration is illustrated as a section view in Figure 3.49. Again, the thermocouple must be the last item fastened to the test section during assembly and the first thing detached when disassembling. The orientation of the inlet and outlets is shown in the figure.

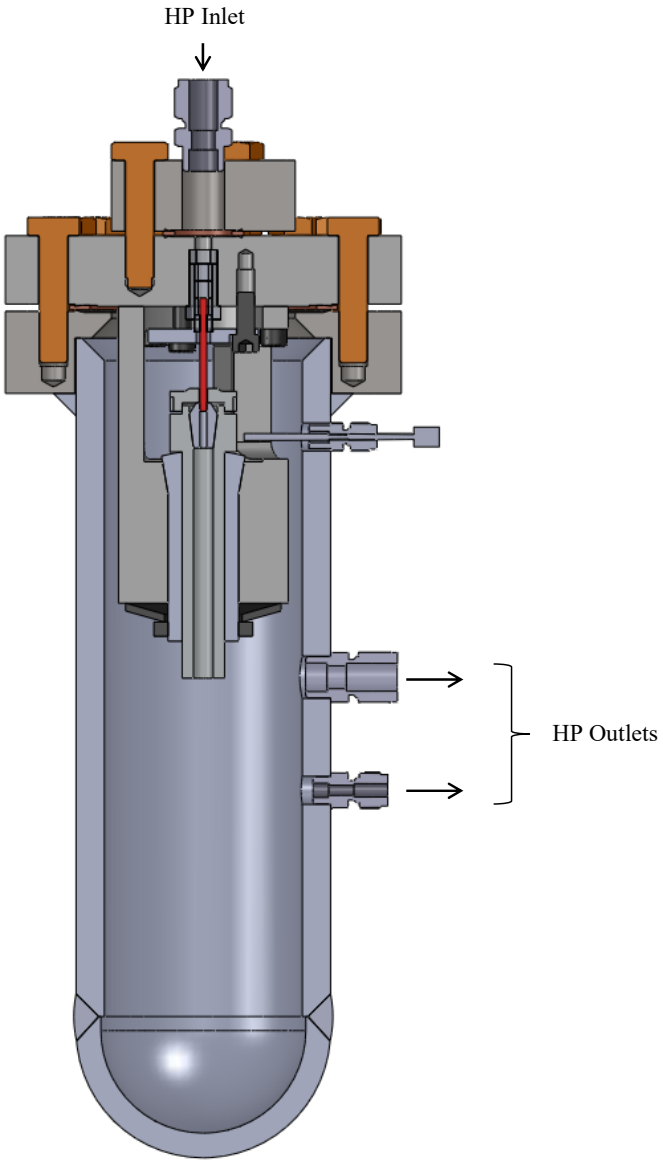

Figure 3.49 Detailed section view of test section

3.6.2 Pressure vessel design

The desired operating pressures of the test facility dictated that the test section needed to be encapsulated in a pressure vessel. The experimental test section was designed with this in mind based on the design methodology outlined in the ASME Boiler and Pressure Vessel Code explained in the *Companion Guide to the ASME Boiler and Pressure Vessel Code* (hereafter referred to as the *Companion Guide*).

The flange was designed according to the 40.6 Flange-Design Methods section of the *Companion Guide* which is based on the design-by-formula approach of the ASME code, ASME Section VIII, Division 1, Appendix 2. The design philosophy shown is for a bolted-flange connection with ring-type gaskets.

The design criteria used in the design of this flange is shown in Table 3-12. The units are specified in English units as consistent with the *Companion Guide*. It is important to note that the design specifications outlined in Pressure Vessel Engineering Ltd. have been heavily referenced in this analysis.

Materials

The first step was to determine the design strength of the materials used in the facility. The materials used to construct the test section are itemized in Table 3-11 along with the ambient

strength, design strength, and maximum temperature supported by the facility. The design strength was ascertained at the temperature specified in equation (3.67).

$$T_{design} = 350^{\circ} F \tag{3.67}$$

Table 3-11 Properties of materials used to construct pressure vessel housing

MATERIAL		AMBIENT STRENGTH (psi)	DESIGN STRENGTH (psi)	MAX TEMPERATURE (°F)
SA-312 304L	Sms. and Weld Pipe	16700	16250	1200
SA-240 316	Plate	20000	19650	1500

A linear interpolation between the ASME pressure vessel values at 300°F and 400°F was used for both materials.

Shell Housing

The shell housing was specified according to the parameters itemized in Table 3-12. The objective was to minimize the cost by minimizing the material required to construct the test section. A 4" nominal pipe size cylinder was used to create the shell of the pressure vessel. A detailed analysis is provided below.

Table 3-12 Straight shell design parameters

DESIGN PARAMETERS	VARIABLE	VALUE
STRAIGHT PIPE SHELL		
Nominal pipe size		4 in nps sch 160
Pipe material		SA-312 304L
Temperature		350°F
Pressure	P	3000 psi
Outside diameter	Do	4.5 in

Nominal wall thickness	t	0.531
Pipe length	L	12 in
Corrosion allowance	Corr	0.005 in
Allowable stress at design temp (350°F)	S_f	16250 psi
Long seam efficiency (hoop stress)	E_{long}	0.85
Circum. seam efficiency (long stress)	E_{circum}	0.70
Undertolerance allowance	UTP	12.5%

An undertolerance allowance *UTP* of 12.5% was specified to account for deviations in wall thickness which may occur during the extrusion process as shown in equation (3.68). The nominal thickness was then determined accounting for both the undertolerance as well as the corrosion allowance as demonstrated in equation (3.69). The corrected radius was determined from equation (3.70).

$$UT = t \cdot UTP \quad undertolerance\,allowance \tag{3.68}$$

$$nt = t - Corr - UT \quad nominal\,thickness \tag{3.69}$$

$$R_{inner} = \frac{D_o}{2} - nt \quad inner\,radius\,corrected\ \ for\,allowances \tag{3.70}$$

The required thickness based on the hoop stress and longitudinal stress as required by ASME is determined in equation (3.71).

Required thickness parameters

$$ta = \frac{P \cdot R_{inner}}{S \cdot E_{long} - 0.6 \cdot P} \quad \textit{Required longitudinal thickness} \tag{3.71}$$

$$tb = \frac{P \cdot R_{inner}}{2 \cdot S \cdot E_{circum} + 0.4 \cdot P} \quad \textit{Required circumferential thickness}$$

The thickness determined in equation (3.69) must be greater than both the longitudinal and circumferential thickness as shown in equations (3.72) and (3.73).

$$T_{required} = \max(ta, tb) + Corr \tag{3.72}$$

$$nt \geq T_{required} \quad \textit{Thickness requirement} \tag{3.73}$$

The internal pressure supported longitudinally and circumferentially by the shell is demonstrated in equation (3.74).

Maximum pressure

$$P_{long,internal} = \frac{S \cdot E_{long} \cdot nt}{R_{inner} + 0.6 \cdot nt} \tag{3.74}$$

$$P_{circum,internal} = \frac{2 \cdot S \cdot E_{circum} \cdot nt}{R_{inner} - 0.4 \cdot nt}$$

The maximum internal pressure is determined by equation (3.75) where the design pressure must be lower than the maximum pressure as in (3.76).

$$P_{\max} = \min\left(P_{long,internal}, P_{circum,internal}\right) \tag{3.75}$$

$$P_{max} \geq P \tag{3.76}$$

Weld-cap

The test section weld-cap was evaluated as an elliptical head to be conservative. The ideal shape for a head is a hemisphere which divides the pressure across the surface of the head equally. It is more common, however, to find elliptical heads available for purchase as this shape is oftentimes more economical. The elliptical head incurs a reduction in overall capacity as the radius of curvature is now a function rather than a fixed value.

The actual cap resembles a hemisphere more than an ellipse so the values listed here are purely conservative. Note that the test section cap was the least concerning aspect of this design from a maximum allowable working pressure point of view because the weld-cap could stand up to 2 or 3 times the factor of safety already built-in to the ASME Pressure Vessel Code.

Table 3-13 Elliptical head design parameters

DESIGN PARAMETERS	VARIABLE	VALUE
ELLIPTICAL HEAD		
Nominal pipe size		4 in nps sch 160
Pipe material		SA-312 304L
Temperature		350°F
Pressure	P	3000 psi
Outside diameter	Do	4.5 in
Thickness before forming	tb	0.531 in
Corrosion allowance	Corr	0.005 in
Straight skirt length	Skirt	1 in
Allowable stress at design temp (350°F)	S_f	16250 psi
Head longitudinal efficiency	E_{head}	0.85

The parameters used to evaluate the test section cap are listed in Table 3-13. A detailed analysis is provided in this section consistent with ASME specifications.

The thickness after forming was evaluated based on equation (3.77). The value obtained notes the thickness that can be expected once the metal has been stretched over a mold.

$$tf = \left\{ \begin{array}{l} tb - \frac{5}{8} in \rightarrow tb \leq \frac{9}{16} in \\ 0.85 \cdot tb \rightarrow tb \leq \frac{9}{16} in \end{array} \right\} \tag{3.77}$$

The nominal thickness is determined as a function of the form thickness minus the corrosion allowance by equation (3.78). The inner diameter is corrected based on the nominal thickness as demonstrated in equation (3.79).

$$nt = tf - Corr \quad nominal\,thickness \tag{3.78}$$

$$D = D_o - 2 \cdot nt \quad inner\,diameter\,corrected\ \ for\,allowances \tag{3.79}$$

The inside crown height is determined based on the corrected diameter as in (3.80). The outer crown height is determined from the bottom equation reported in (3.80).

$$\begin{array}{l} h = \frac{D}{4} \qquad inner\,crown\,height \\ h_o = h + nt \quad outer\,crown\,height \end{array} \tag{3.80}$$

These values obtained from equations (3.79) and (3.80) are used in equation (3.81) based on the reference tables listed for each equation as they have been reported by PV Engineering Ltd. EES was used to generate polynomial curve fits based on the lookup values as is demonstrated in Figure 3.50 and Figure 3.51. The polynomial curve fits are reported here in equation (3.82) through (3.84). Notice the similarity between equations (3.83) and (3.84).

$$\begin{aligned} K &= K\left(\frac{D}{2h}\right) \quad \textit{Table } 1-4.1 \\ K_1 &= K_1\left(\frac{D}{2h}\right) \quad \textit{Table UG}-37 \\ K_0 &= K_0\left(\frac{D_o}{2h_o}\right) \quad \textit{Table UG}-33.1 \end{aligned} \tag{3.81}$$

$$K = 0.337 - 0.0112\left(\frac{D}{2h}\right) + 0.174\left(\frac{D}{2h}\right)^2 - 0.00127\left(\frac{D}{2h}\right)^3 \tag{3.82}$$

$$K_1 = 0.253 + 0.140\left(\frac{D}{2h}\right) + 0.122\left(\frac{D}{2h}\right)^2 - 0.0153\left(\frac{D}{2h}\right)^3 \tag{3.83}$$

$$K_0 = 0.253 + 0.140\left(\frac{D_0}{2h_0}\right) + 0.122\left(\frac{D_0}{2h_0}\right)^2 - 0.0153\left(\frac{D_0}{2h_0}\right)^3 \tag{3.84}$$

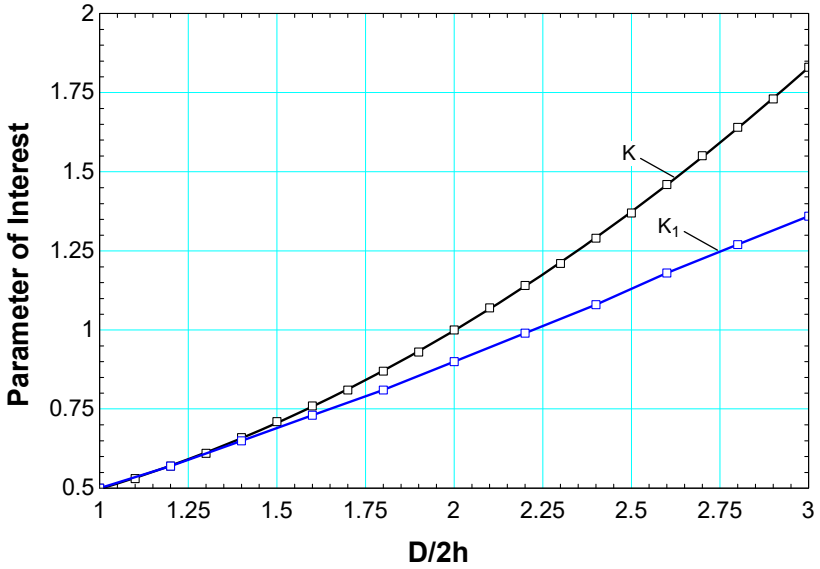

Figure 3.50 Parameters used to determine inner crown efficiency

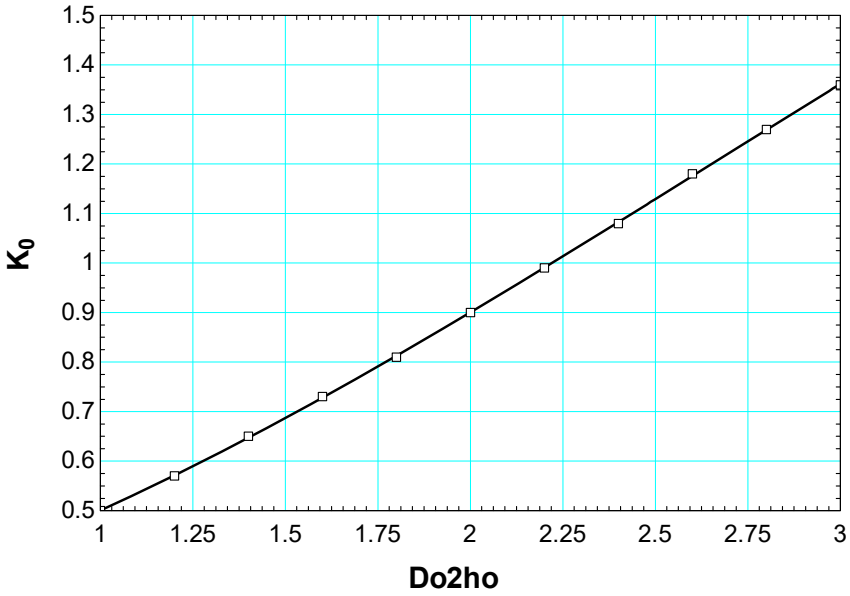

Figure 3.51 Parameters used to determine outer crown capacity

The parameters K, K_1, and K_0 are effectively form factors that accommodate the deviations from the ideal hemispherical head. Elliptical "stunting" of the cap results in non-linear stress distributions which are a function of the cap's radius of curvature profile.

An effective outer radius is determined based on the outer crown parameter K_0 as demonstrated in equation (3.85).

$$R_o = K_0 D_o \tag{3.85}$$

An analysis calculation is required if the parameter listed in equation (3.86) falls within the bounds specified in the first line. This is essentially a ratio of the forming thickness to the inner diameter multiplied by the inner crown parameter K_1. It is desirable to maintain as large of curvature as possible so that stress risers do not become excessive. In this case, the worse possible configuration corresponds to a flat surface.

$$App_{1-4}: \begin{array}{l} 0.0005 \le \dfrac{tf}{K_1 D} < 0.002 \rightarrow Calculation\ required \\ \dfrac{tf}{K_1 D} > 0.002 \rightarrow Calculation\ not\ required \end{array} \tag{3.86}$$

Calculation of this parameter was not required in the design of this pressure vessel as equation (3.86) was found to lie in acceptable bounds even in this conservative analysis.

The required thickness was determined based on equation (3.87) where the formed thickness was found to be larger than that required as noted in equation (3.88).

$$t_{required} = \frac{P \cdot D \cdot K}{2 \cdot S \cdot E - 0.2 \cdot P} + Corr \tag{3.87}$$

$$tf \geq t_{required} \tag{3.88}$$

The max pressure was determined based on equation (3.89) where the design pressure is much less as shown in equation (3.90).

$$P_{\max} = \frac{2 \cdot S \cdot E \cdot nt}{K \cdot D + 0.2 \cdot nt} \tag{3.89}$$

$$P_{\max} \geq P \tag{3.90}$$

Again, the test section cap was by no means the limiting constraint in this test section design.

Flange Construction

The flange design was optimized to incorporate the test section as well as use the least amount of material as possible. The final configuration called for 6 kg loose-flange mated to a 9.5 kg blind flange. To put things into perspective, comparable standard class 1500 ASME flanges of this nature would have resulted in at 28.5 kg and 33.8 kg respective assembly. Standard ASME

flanges are expensive and not easily modified. A graph of ASME flange specifications of pressure as a function of temperature has been provided in Figure 3.52. The minimum flange that meets the criteria for this test facility is highlighted as a class 1500 flange where the cost for a single class 1500 flange made of 316 stainless steel was determined to be in the thousands of dollars

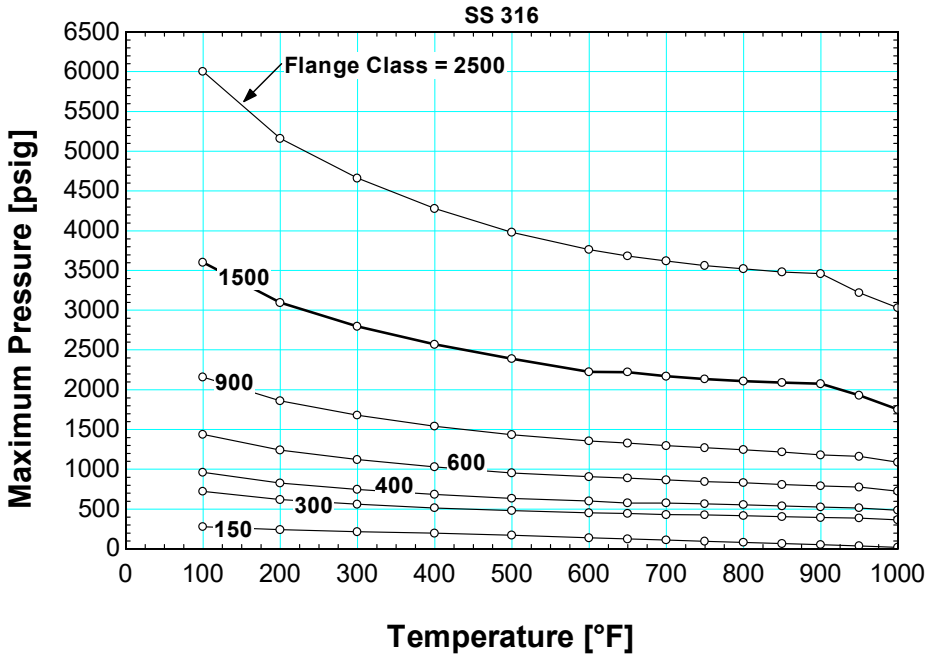

Figure 3.52 ASME SS 316 flange rating for different flange classes based on temperature

A list of the parameters used to design the flange for this pressure vessel is provided in Table 3-14. The flange analysis is for a loose-type flange without hubs. Notice that the parameters listed in Table 3-14 document the flange, which was welded to the shell housing only.

The parameters listed in Table 3-14 note a reduction in the desired operation pressure from $3000\,psi$ to $2600\,psi$. This reduction was necessary as the machine shop hired to construct this test section misread a print and did not include a knife-edge in the final product. The parts came back with an o-ring indentation and not a conflate-type surface. A reduction in the final working pressure was required to accommodate this change.

Table 3-14 Parameters used for loose type flange welded to accumulator tank

DESIGN PARAMETERS	VARIABLE	VALUE
FLANGE		
Flange material		SA-240 316
Temperature		350°F
Pressure	P	2600 psi
Outside diameter	A	7 in
Inside diameter	B	3.25 in
Flange thickness	t	1.48 in
Hubs	h	0.5 in
Allowable stress at assembly temp (70°F)	S_{fa}	20000 psi
Allowable stress at design temp (350°F)	S_{fo}	19600 psi
BOLTS		
Bolt material		SA 193 b7
Bolt size		½-13
Conservative torque bolt diameter	$D_{bolt,torque}$	0.5 in
Effective bolt area	$A_{bolt,eff}$	0.126 in^2
Tensile bolt area	A_t	0.142 in^2
Bolt circle	C	5.4 in
Number of bolts	Nbolts	14
Allowable stress at assembly temp (70°F)	S_a	80000 psi
Allowable stress at design temp (350°F)	S_b	80000 psi
Copper frictional bolt lubricant	k_{fric}	0.2
Number of threads per inch	n_{thread}	13
GASKET		
Gasket material		Soft copper
Gasket factor	m	4.75
Design seating stress	y	13000 psi
Outer diameter	$Gasket_{OD}$	4.743 in
Inner diameter	$Gasket_{ID}$	4.006 in
Knife-edge diameter	$D_{knife-edge}$	4.6 in

Gasket load reaction diameter	G	4.6 in
Effective seating width (estimated)	b	0.1 in

The methodology used in the final configuration met the design criteria by following the general rules of thumb shown below:

- Reduce the outer diameter to a form factor which is governed by the size of the bolt head and the outside diameter of the nominal pipe size.
- Limit the effective gasket seating width by incorporating a knife-edge.
- Increase the inner diameter to a value that is constrained by the inner pipe diameter.
- Use several smaller bolts instead of fewer larger bolts to limit the size of the bolt head.
- Constrain the gasket load reaction diameter with a knife-edge as close to the bolts as possible to maximize gasket seating stress to limit assembly stress.
- Use higher grade bolts to accommodate the larger stress concentrations which are observed with smaller bolts.

An illustration is shown here from Bickford and Nassar (1998) that demonstrates the critical parameters evaluated in this analysis. The definitions for each parameter identified in this section are largely expounded upon from the definitions provided by Bickford and Nassar (1998).

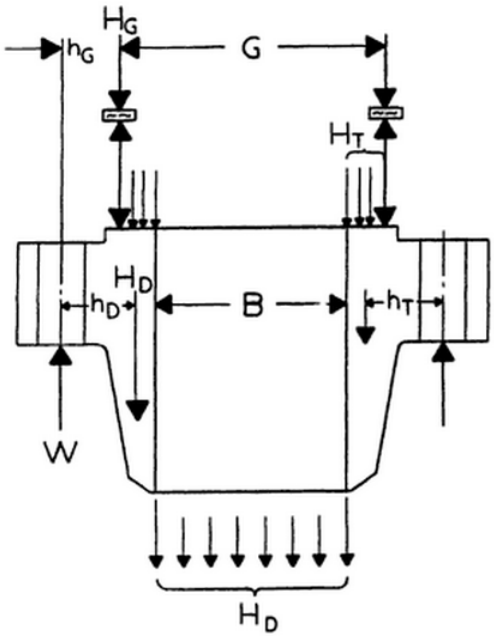

Figure 3.53 Illustration of critical parameters used to evaluate flanges by Bickford and Nassar (1998)

The *Companion Guide* requires the basic gasket contact width to be determined. This is just the radial displacement from the inner to the outer diameter of the gasket as demonstrated in equation (3.91). The result is used to calculate the basic gasket seating width which is assumed to be half the basic gasket contact width as shown in equation (3.92).

$$N = \frac{1}{2}\left(Gasket_{OD} - Gasket_{ID}\right) \quad Basic\ gasket\ contact\ width \tag{3.91}$$

$$b_o = \frac{N}{2} \qquad \textit{Basic gasket seating width} \qquad (3.92)$$

The result of equation (3.92) is used to determine the effective gasket seating width shown here as equation (3.93). The results are plotted as a function of the basic gasket contact width N in Figure 3.7.

$$b = \begin{Bmatrix} b_o \rightarrow b_o \leq 0.25in \\ \frac{1}{2}\sqrt{b_o} \rightarrow b_o > 0.25in \end{Bmatrix} \quad \textit{Effective gasket seating width} \qquad (3.93)$$

The problem with the definition of the effective gasket seating width demonstrated in equation (3.93) is that gaskets made of materials with higher yield strengths will not seat properly during assembly. The problem must then be overcome by using larger bolts to sustain the larger clamping forces required to properly seat the gasket. The form factor of the entire assembly will effectively double if not triple in size if this seemingly simple concept is not kept in check.

Gaskets are typically made of polymer materials in order to avoid this issue. Polymer materials were avoided in this design in order to avoid solvent issues associated with S-CO_2. Kruizenga (2010) noted that Viton seals used to hold his test section together would show appreciable size deformation after each use.

Copper seals were incorporated into the design of this test facility as is commonly used to create exceptional sealing in vacuum technology. A conflate-type knife-edge was used to seat the

gasket and an estimate of the effective gasket seating width was evaluated based on equation (3.94). The results from this estimate are also plotted in Figure 3.54.

$$b = \begin{Bmatrix} b_o \rightarrow b_o \le 0.1in \\ 0.10in > 0.10in \end{Bmatrix} \quad Knife-edge\ effective\ gasket\ seating\ width \tag{3.94}$$

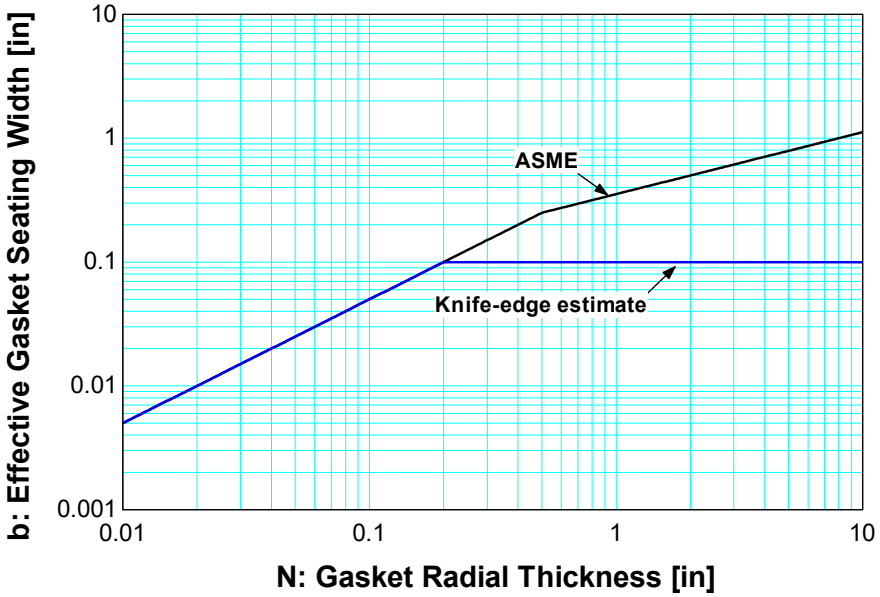

Figure 3.54 Effective gasket seating width based on ASME specification and new design shown with knife-edge estimate

The effective gasket load reaction location was another parameter that needed to be controlled. The definition based on ASME specification is shown in equation (3.95). The results are plotted as a function of

$$G = \left\{ \begin{array}{c} \frac{1}{2}\left(Gasket_{OD} + Gasket_{ID}\right) \rightarrow b_o \leq 0.25in \\ Gasket_{OD} - 2b \rightarrow b_o > 0.25in \end{array} \right\} Gasket\ load\ reaction\ location \qquad (3.95)$$

The problem with this approach is that as the difference between the inner and outer diameter increases, the gasket load reaction location moves farther away from the bolt circle diameter. As the gasket load reaction moves away from the bolt circle, the clamping force generated by the bolts becomes less effective at seating the gasket. The objective is to position the gasket load reaction location as close to bolts as possible.

The position of the knife-edge was fixed as close to the bolt-circle as possible and is set at a fixed value of 4.6 inches by equation (3.96). Copper gaskets from Nor-Cal were purchased for the facility. Note that the diameter of knife-edge was bounded by the dimensions of the gaskets available from Nor-Cal fixed at 4.743 inches and 4.006 inches.

$$G = D_{knife-edge} \qquad (3.96)$$

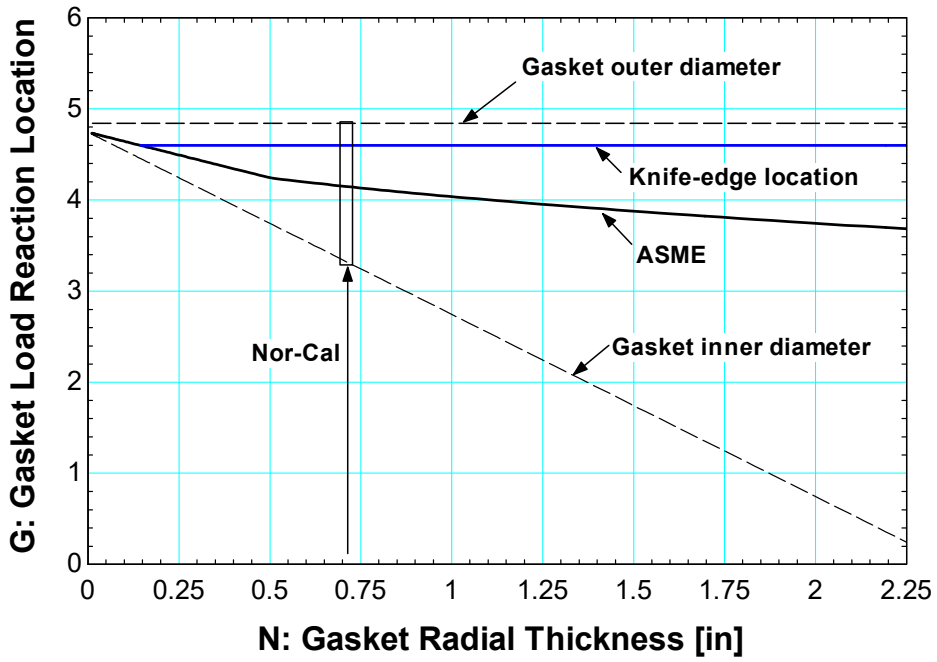

Figure 3.55 ASME equation-specified gasket load reaction location as a function of gasket thickness. Outer diameter of copper seal used in facility is specified with all other parameters varying according to the gasket thickness

Figure 3.55 demonstrates the importance of using a knife-edge with gaskets that have a larger radial thickness. If this location is not properly controlled, the effective gasket load reaction moves farther away from the outer diameter of the gasket and decreases the effectiveness of the clamping force generated by the bolts during assembly. Most polymer seals are very thin and the gasket load reaction occurs very close to the outside diameter of the gasket. For this reason, polymer seals can be located very close to the bolt-circle diameter where the clamping force generated by the bolts will be most effective.

There are benefits and consequences to positioning the gasket load reaction location so close to the gasket outer diameter. On one level, the hydrostatic load is increased as the cross-sectional area exposed to pressure is increased. This has the unfortunate consequence of increasing the normal stress that the bolts need to overcome and attributes to the requirement for larger bolts. The benefit of course is that the load reactions get closer to the bolt-circle diameter which has the potential to lower the bending stresses throughout the pressure vessel. This concept is conceptually explained in the assessment that follows.

The total hydrostatic load is evaluated according to equation (3.97). Note that the cross-sectional area shown here represents the total area exposed to pressure.

$$H = \underbrace{\frac{\pi}{4}G^2}_{A_e} P \quad Total\ hydrostatic\ load \tag{3.97}$$

Note that a larger gasket load reaction location will lead to higher load concentration for H and H_T during operation as the effective area exposed to pressure increases as demonstrated in equation (3.97) and equation (3.99). This is an unfortunate byproduct of placing the gasket load reaction location as close to the bolt-circle diameter as possible. This issue also has drawbacks on the assembly stress however as is demonstrated in equation (3.98). The problem is mitigated however, as the effective gasket seating width b determined from equation (3.94) for a knife-edge is much smaller than that determined based on ASME specifications as was demonstrated in Figure 3.54. The variable m in this case notes the gasket factor which is

relatively large for harder materials – i.e. copper has a gasket factor of $m = 4.75$ as was noted in Table 3-14.

$$H_P = 2m \underbrace{\pi b G}_{A_{gasket}} P \quad Required\ gasket\ load \tag{3.98}$$

The difference between the total hydrostatic end force and the hydrostatic end force acting on the area inside the flange is calculated from equation (3.99).

$$\begin{aligned} H_D &= \frac{\pi}{4} B^2 P \\ H_T &= \underbrace{\frac{\pi}{4}\left(G^2 - B^2\right)}_{A_{flange}} P = H - H_D \end{aligned} \tag{3.99}$$

The minimum required bolt load during operation and assembly is calculated from equation (3.100). The gasket seating width b is also important here to limit the required seating area. The variable y is the design seating stress and has a required value of $y = 13000\,psi$ for copper.

$$\begin{aligned} W_{m1} &= H + H_p \quad Minimum\ required\ bolt\ load\ during\ operation \\ W_{m2} &= \underbrace{\pi b G}_{A_{gasket}} y \quad Minimum\ required\ bolt\ load\ \ for\ gasket\ seating \end{aligned} \tag{3.100}$$

The minimum area required during operation and assembly are calculated from equation (3.101). The required bolt area is determined to be the greater of the two requirements as noted in equation (3.102).

$$A_{m1} = \frac{W_{m1}}{S_b} \quad Required\ bolt\ area\ during\ operation$$
$$A_{m2} = \frac{W_{m2}}{S_a} \quad Required\ bolt\ area\ \ for\ gasket\ seating \tag{3.101}$$

$$A_m = \max\left(A_{m1}, A_{m2}\right) \quad Required\ bolt\ area \tag{3.102}$$

The actual bolt area is determined based on the effective area of the bolts as found from ASME specifications and calculated from equation (3.103).

$$A_b = N_{bolts} A_{bolt,eff} \qquad Actual\ bolt\ area \tag{3.103}$$

Note that the effective area is a reduced quantity from the nominal area of a standard bolt. The value published here is based on that shown in the *Companion Guide.* The idea is expressed in equation (3.104).

$$A_{bolt,eff}\left(bolt = \frac{1}{2} - 13\right) \neq A_{nom-bolt}\left(bolt = \frac{1}{2} - 13\right)$$
$$A_{nom-bolt} = \frac{\pi}{4}\left(\frac{1}{2}\right)^2 = 0.196 in^2 \tag{3.104}$$
$$A_{bolt,eff} = 0.126 in^2$$

Finally, the criteria shown in equation (3.105) must be satisfied.

$$A_b \geq A_m \tag{3.105}$$

The required bolt load are demonstrated here in equation (3.106) is defined as the maximum of the operational and assembly bolt loads previously calculated in equation (3.100). The maximum available bolt load is taken as an average of the actual and required bolt areas multiplied by the allowable stress $S_a = 80000\,psi$ of the bolts at the assembly temperature of 70°F. Note that the values published in Table 3-14 correspond to a standard grade 8 bolt rated at the proof load. The proof load of a bolt is a value which is marginally smaller than the yield strength of that bolt.

$$\begin{aligned} W_{required} &= \max\left(W_{m1}, W_{m2}\right) \qquad Minimum\,bolt\,load\,required \\ W_{possible} &= \frac{1}{2}\left(A_m + A_b\right) S_a \qquad Maximum\,actual\,bolt\,load \end{aligned} \tag{3.106}$$

The requirement of course is that the bolt will not fail as demonstrated in equation (3.107).

$$W_{possible} > W_{required} \tag{3.107}$$

The bolts actually used in this facility were grade 9 rated to a proof load of $120000\,psi$ and were only slightly more expensive than bolts designated as grade 8. Nevertheless, the calculations were conservatively based on grade 8.

The load reaction locations are obtained from the definitions found in equation (3.108). Note that these definitions are only to be applied for loose-type flanges. Integral flanges require different definitions based on ASME specifications.

$$\begin{aligned}
&\textit{Load locations relative to bolt} - \textit{circle} \\
&h_D = \frac{1}{2}(C - B) \qquad \textit{distance to inner flange diameter} \\
&h_G = \frac{1}{2}(C - G) \qquad \textit{distance to gasket load reaction location} \\
&h_T = \frac{1}{2}(h_D + h_G) \qquad \textit{averaged distance to load location of } H_T
\end{aligned} \tag{3.108}$$

The benefit previously mentioned regarding a reduction in bending stress is realized here as equation (3.109) where the increase in G always results in a reduction of the generated moment incurred during assembly. In contrast, the moment generated during operation may increase or decrease depending on the situation as is demonstrated for this pressure vessel illustrated in

$$\begin{aligned}
&M_{o,assembly} = \frac{1}{2} W_{m2} (C - G) \qquad \textit{Moment generated during assembly} \\
&M_{o,operating} = h_D H_D + h_T H_T + h_G H_G \quad \textit{Moment generated during operation}
\end{aligned} \tag{3.109}$$

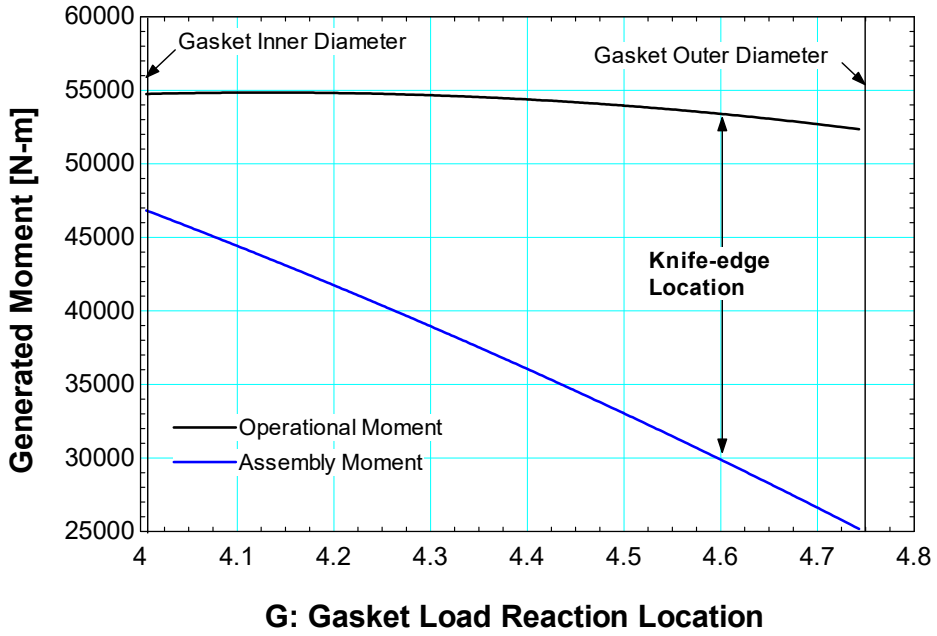

Figure 3.56 Assembly and operational moments generated as a function of gasket load reaction for the parameters listed in Table 3-14.

Curve-fit parameters have been developed to accommodate for other flange effects not expressly accounted for by the moments and normal forces previously expressed. The equations for the curve fit parameters $T, U, Y, \text{and } Z$ are based on the factor K which is effectively a ratio of the flange outer diameter $A = 7in$ to the flange inner diameter $B = 3.25in$ as identified in Table 3-14.

Parameters for flanges

$$K = \frac{A}{B}$$

$$T = \frac{K^2\left(1 + 8.55246\log_{10} K\right) - 1}{\left(1.04720 + 1.9448K^2\right)\left(K - 1\right)}$$

$$U = \frac{K^2\left(1 + 8.55246\log_{10} K\right) - 1}{1.36136\left(K^2 - 1\right)\left(K - 1\right)} \tag{3.110}$$

$$Y = \frac{1}{K - 1}\left(0.66845 + 5.7169\left(\frac{K^2\log_{10} K}{K^2 - 1}\right)\right)$$

$$Z = \frac{K^2 + 1}{K^2 - 1}$$

The factor h_o is calculated from equation (3.111) where B is the flange inner diameter and g_o is the hub thickness. The hub thickness is effectively the stub height that adjoins the flange to the pipe wall. Note that this analysis considers a loose-type flange with no hubs, which is a conservative estimate that effectively assumes all bending stress acts through the flange itself and the pipe wall is not load bearing. The assumption is not the case as the pipe wall is 0.53 in thick 304L stainless steel.

$$h_o = \sqrt{B\,g_o} \tag{3.111}$$

More flange factors for loose-type flanges are identified in equation (3.112) and (3.113). The factors identified by equation (3.112) were read from figures in the *Companion Guide*.

$$
\begin{aligned}
&Loose-type\ flange\ factors \\
&F_L = F_L\left(\frac{g_1}{g_o}, \frac{h}{\sqrt{B\,g_o}}\right)\ Fig.2-7.4 \\
&V_L = V_L\left(\frac{g_1}{g_o}, \frac{h}{\sqrt{B\,g_o}}\right)\ Fig.\ 2-7.3
\end{aligned}
\tag{3.112}
$$

Note that $t = 1.48in$ notes the flange thickness in equation (3.113).

$$
\begin{aligned}
&Loose-type\ flange\ factors\ 2 \\
&d = \frac{U}{V_L} h_o g_o^2 \\
&e = \frac{F_L}{h_o} \\
&L = \frac{te+1}{T} + \frac{t^3}{d}
\end{aligned}
\tag{3.113}
$$

Finally, the flange stresses are calculated as demonstrated in equation (3.114). Again, this analysis considers the conservative estimate for a loose-type flange with no hubs.

$$
\begin{aligned}
&Loose\ flange\ without\ Hubs \\
&S_T = \frac{YM_o}{t^2 B} \\
&S_R = 0 \\
&S_H = 0
\end{aligned}
\tag{3.114}
$$

Two stress values are determined from the top line in equation (3.114). The operating and assembly stresses are calculated based on equation (3.115) respectively.

$$S_{T,operating} = \frac{YM_{o,operation}}{t^2 B} \quad Operating\ stress$$
$$S_{T,assembly} = \frac{YM_{o,assembly}}{t^2 B} \quad Assembly\ stress \tag{3.115}$$

Finally, the requirements identified in equation (3.116) must be met. That is, the operating stress must be less than the allowable stress at the design temperature of 350°F and the assembly stress must be less than the allowable stress at the assembly temperature of 70°F. The final results are illustrated in Figure 3.57. Notice that even at the de-rated sustainable pressure of $2600\,psi$, the max operational stress is slightly exceeded based on the location of the knife-edge built into this facility.

$$S_{fo} \geq S_{T,operating}$$
$$S_{fa} \geq S_{T,assembly} \tag{3.116}$$

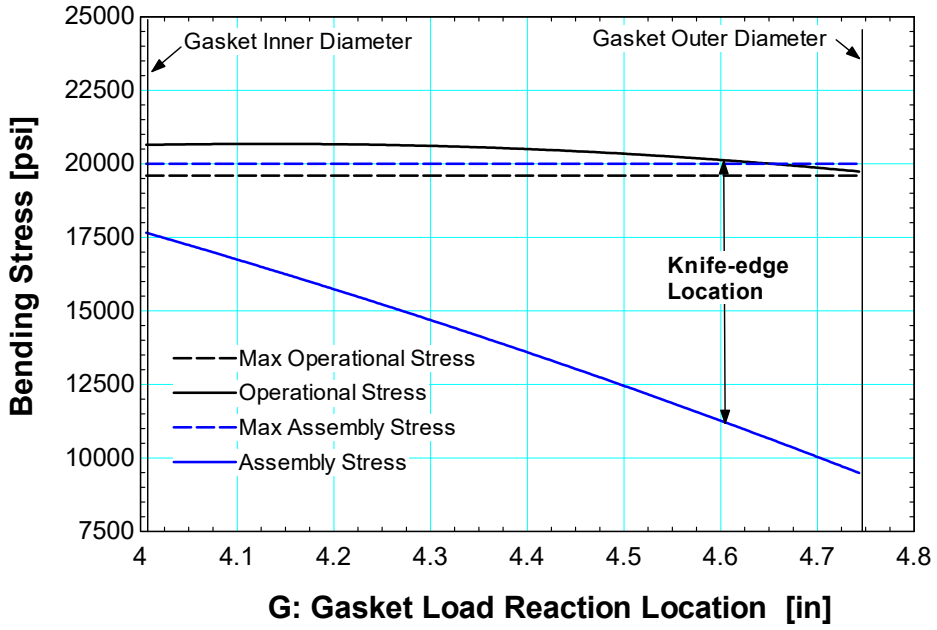

Figure 3.57 Assembly and operational stress as a function of gasket load reaction for the parameters listed in Table 3-14.

The proper preload for the assembly was determined based on equation (3.117) shown below. Effectively, the total of the hydrostatic load and the gasket load is divided among the bolts to determine the minimum required clamping force per bolt.

$$F_k = \frac{\overbrace{H}^{hydrostatic\ load} + mP\overbrace{\left(\pi G b\right)}^{A_{gasket}}}{N_{bolts}}^{gasket\ load} \quad Minimum\ required\ clamping\ \ force\ per\ bolt \qquad (3.117)$$

The minimum required bolt torque is calculated as demonstrated in equation (3.118). Notice that a lubricant frictional coefficient k_{fric} is necessary to prevent galling. The lubricant used is a

copper-based paste rated at $k_{fric} = 0.2$ by the manufacturer. Furthermore, the bolt diameter $D_{bolt,torque} = 0.5in$ was evaluated conservatively so that the minimum required torque would generate more and not less clamping force than that required by (3.117). The required torque was determined to be about $\Gamma = 35lb - ft$.

$$\Gamma = k_{fric} D_{bolt,torque} F_k \quad Minimum\ required\ torque\ per\ bolt \tag{3.118}$$

The assembly was hydrostatically tested to 2600 psi in July 2010.

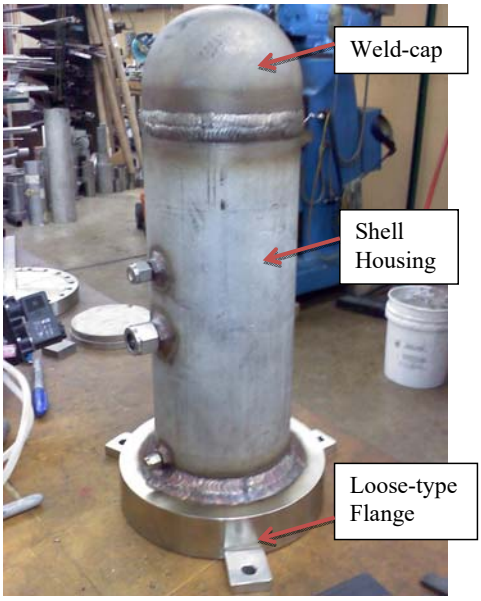

Figure 3.58 Final assembly of pressure vessel based on this analysis

The following analysis was calculated post-construction and concerns thread engagements. The analysis shows that the actual thread engagement is slightly lower than that determined by this design by formula methodology detailed here as equation (3.119) through (3.121).

The screw needs to fail before the threads strip. This is an especially critical parameter to calculate when the screw and hole are made of different materials as is the case in this facility. The shear area of the threaded feature is required to be 2 times the tensile stress area of the bolt as demonstrated in equation (3.119).

$$L_{engagement} = \frac{2A_t}{\frac{\pi}{2}\left[D_{major} - 0.64952\left(\frac{1}{n_{threads}}\right)\right]} \tag{3.119}$$

The thread engagement calculated from (3.119) is supplemented by a ratio of the tensile strength of the bolt compared the tensile strength of the hole. In this case, it was desirable that neither the screw nor the hole yield. A ratio of the bolt proof load was divided by the allowable operation stress as demonstrated here as equation (3.120) to approximate the parameter J.

$$J = \frac{\sigma_{tensile}(screw)}{\sigma_{tensile}(hole)} \rightarrow \frac{S_b}{S_{fo}} = \frac{80000\,psi}{19600\,psi} \tag{3.120}$$

The final length of engagement for this facility was determined to be about $1.6\,in$ based on equation (3.121). Unfortunately, the actual thread engagement is slightly lower at $1.3\,in$; the

typical thread engagement methodology of 2.5 times thread diameter of engagement was used in the initial construction as detailed in equation (3.122).

$$L_{engagement,\,final} = \max\left(L_{engagement}, J \cdot L_{engagement}\right) \tag{3.121}$$

$$L_{engagement,rough} = 2.5 \cdot D_{major} \tag{3.122}$$

3.6.3 Two-phase downstream recovery system

The fluid exiting the test section requires that the test facility accommodate a two-phase downstream recovery system. The fluid cavitates as it incurs the drastic pressure drops inherent in this test facility. The problem was mitigated by implementing a buffer tank after the test section which allows the two-phase exhaust to separate into liquid and gas components. Carbon dioxide as a saturated vapor is then pulled from the top of the tank into the compressor. The concept is demonstrated in Figure 3.59.

Figure 3.59-A shows that the fluid from the test section enters the tank as a two-phase mixture which is then exhausted through a long tube that runs all the way to the bottom of the gas cylinder shown in Figure 3.59-B. From there, the fluids separate into liquid and vapor counterparts in order to fill the volume of the gas cylinder entirely. An annular region which is slightly larger than the diameter of the inlet tube is used to extract carbon dioxide as a saturated vapor through the same entry hole in the gas cylinder. The vapor is then extracted through a pipe-tee so that it can be cycled through the compressor.

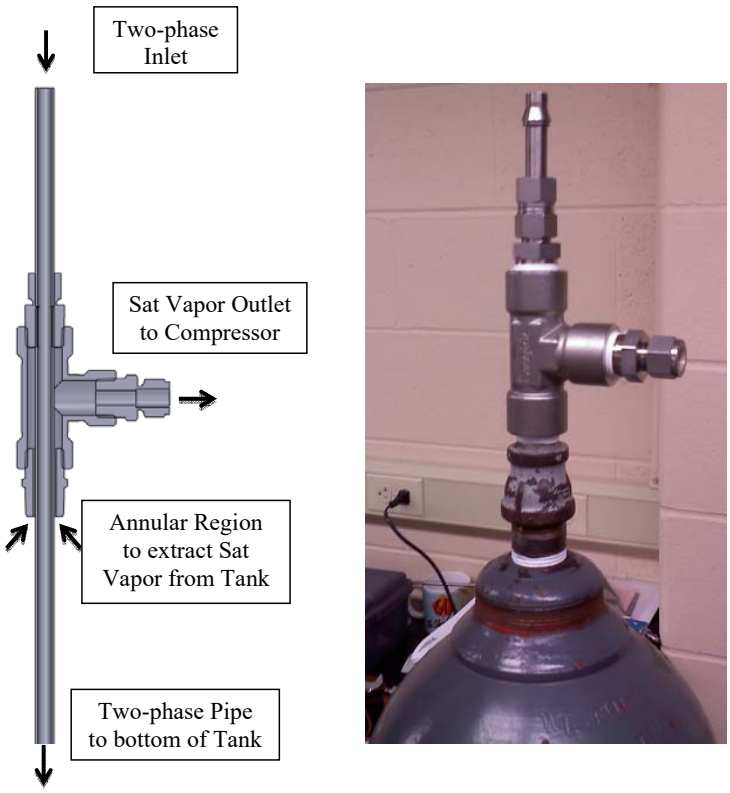

A **B**

Figure 3.59 Two-phase downstream recovery system; A – Two-phase separation system cross-section; B – As configured in actual test section

3.7 Test Facility Construction

A preliminary design was developed in SolidWorks and is shown in Figure 3.60. This initial model was used to design the facility base structure in order to integrate the test section, support equipment, and data acquisition system onto a single assembly. The secondary objective of this

initial design was to determine the instrumentation layout as well as the number of high pressure fittings which would be required.

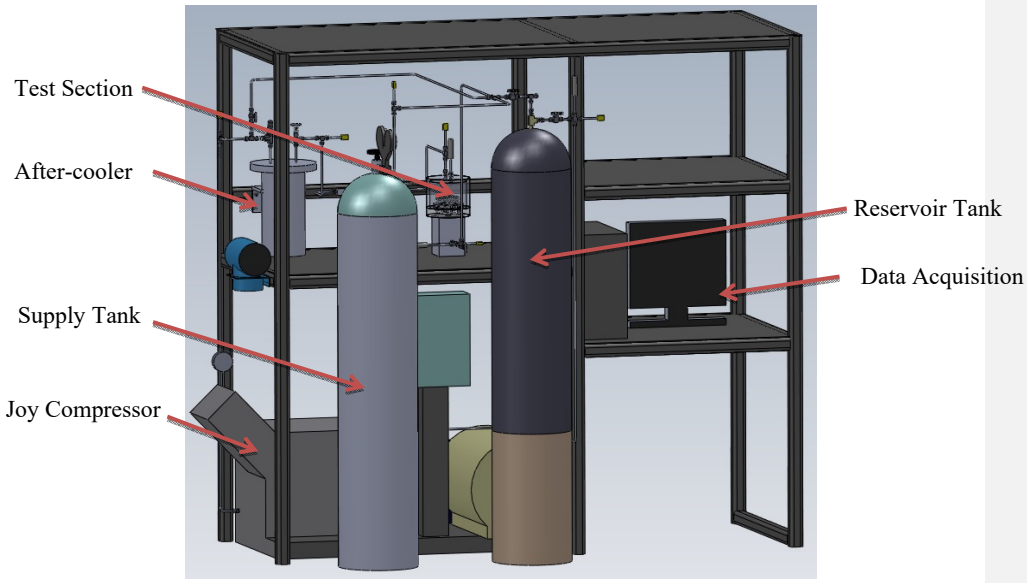

Figure 3.60 Initial SolidWorks representation of UW-Compression Loop facility

The components used in this initial rendering have since been heavily modified as is evident in the latest photographs of the facility illustrated in Figure 3.61~~Figure 3.61~~ and Figure 3.62~~Figure 3.62~~. Notice that the compressor and tanks have been rotated 90° from the original orientation shown in Figure 3.60~~Figure 3.60~~ to allow less restrictive access to the test section.

Formatted: Font: Not Bold
Formatted: Font: Not Bold
Formatted: Font: Not Bold

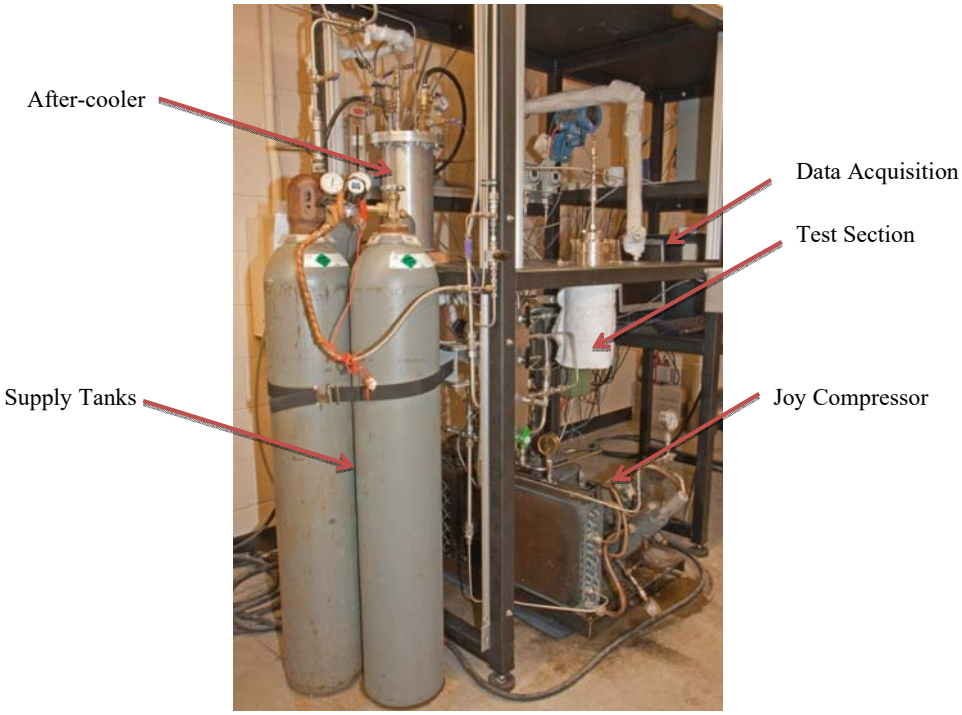

Figure 3.61 UW-Compression Loop facility (side view)

Figure 3.61~~Figure 3.61~~ shows a side view of the test facility at the University of Wisconsin – Madison. The facility requires several supply tanks to charge the facility with sufficient working fluid as the facility is quite large. The Joy compressor shown at the bottom of the figure is a four stage air compressor with intercooling which has been modified to support carbon dioxide through the top two high pressure stages. The bottom stages cycle air from the environment. The exhaust from these two stages exits the compressor as a mixture of the inlet air plus some residual carbon dioxide which has leaked from the top two stages into the bottom stages. This

exhaust is then evacuated to a building exhaust line on the opposite side of the room to prevent asphyxiation during testing.

The major problem with the current configuration is the Joy compressor. It was designed to leak to the environment and it has been particularly challenging to overcome this issue. When the facility is working, testing time is limited to about 15mins total.

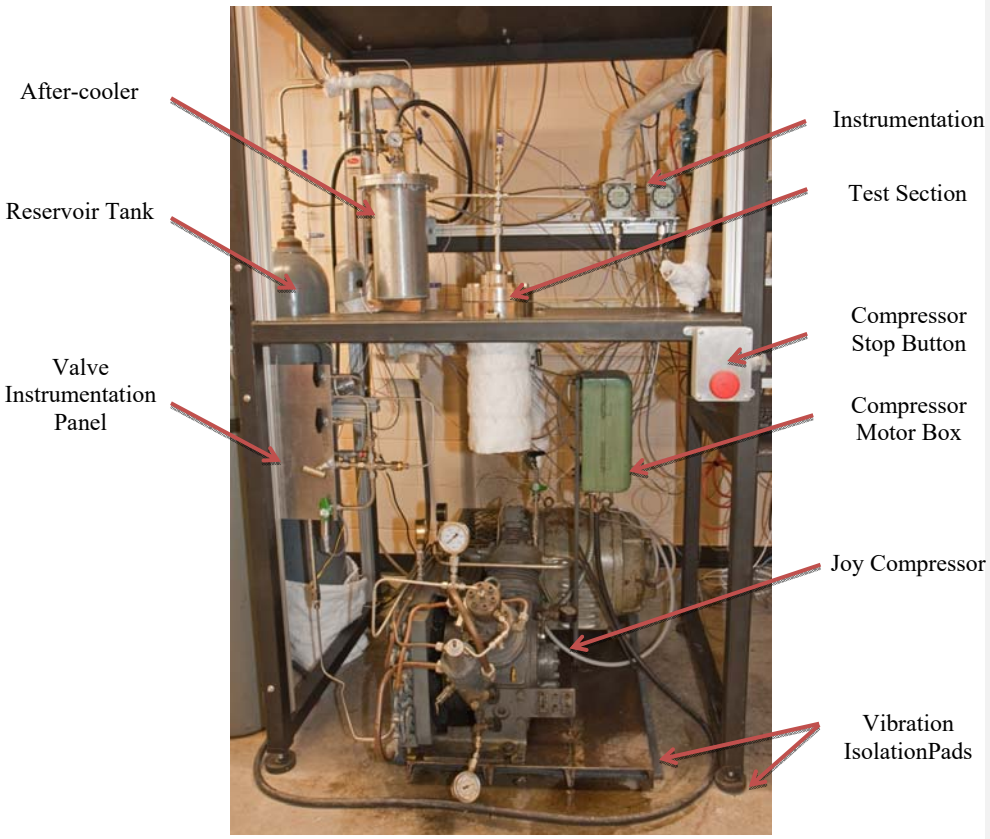

Figure 3.62 UW Compression-Loop facility (front view)

Figure 3.62 shows a front view of the UW Compression-Loop facility without the data acquisition system which is located further to the right. The valve instrument panel is located on the left hand side of the facility and centralizes system control. An emergency compressor stop button is also shown on the right hand side of the photograph.

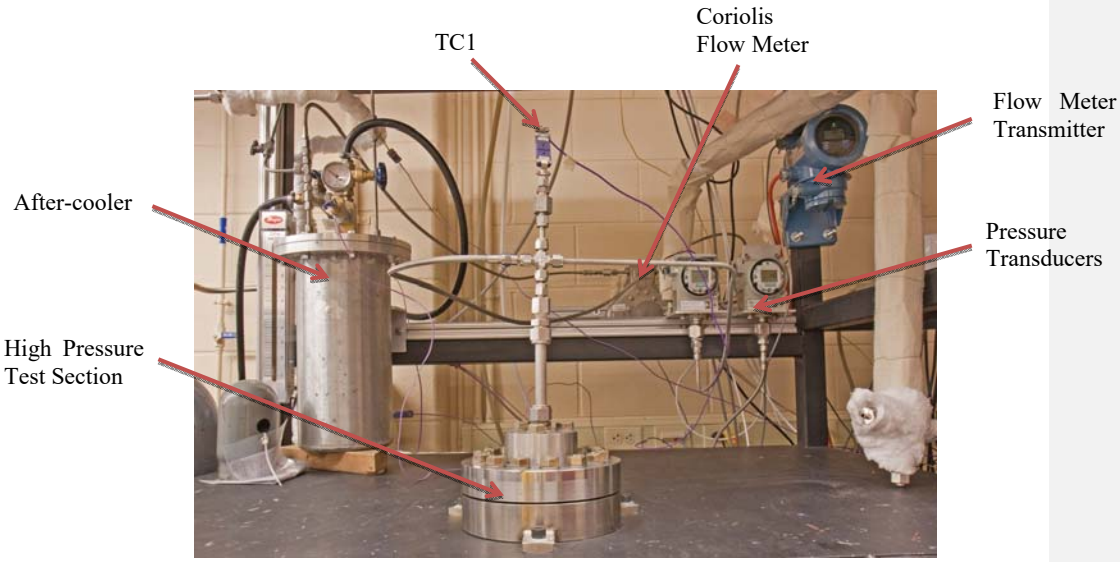

Figure 3.63 High pressure test section along with primary instrumentation

The pressure transducers, coriolis flow meter transmitter, and test section were integrated into the test stand as shown in Figure 3.63. Integration of the test section into the test housing was necessary in order to apply the necessary preload to the bolts used to fasten the test section together.

Notice that the Coriolis flow meter shown in Figure 3.63 was moved away from the test facility. It was discovered that the compressor would vibrate with sufficient energy that the entire facility would shake despite the isolation pads placed at the base of the structure as well as a large vibration pad which was placed underneath the compressor – shown in Figure 3.62. The Coriolis flow meter was then mounted to the wall with additional vibration isolation equipment to overcome this issue.

References

Bickford, J.H. and Nassar, S., 1998, *Handbook of Bolts and Bolted Joints*, Marcel Dekker, Inc. New York.

Gamal, A.M., 2007, Ph.D. thesis. “Leakage and Rotordynamic Effects of Pocket Damper Seals and See-Through Labyrinth Seals.

Go Regulators, www.goreg.com 5 Mar. 2010.

Kruizenga, A., 2010, Ph.D. dissertation. “Heat Transfer and Pressure Drop Measurements in Prototypic Heat Exchangers for the Supercritical Carbon Dioxide Brayton Power Cycles”.

Piercy, N.A., Hooper, M.S., and Winny, H.F., 1933, “Viscous Flow through Pipes with Cores”, Philosophical magazine, Vol. 15, pp 647-676.

Pressure Vessel Engineering, 2010 www.pveng.com 6 Feb. 2010.

Rao, K.R., editor, 2002, *Companion Guide to the ASME Boiler and Pressure Vessel Code*, Vol 2. ASME Press: New York.

Swagelok Cv Flow Coefficient “Valve Sizing: Swagelok CV Flow Coefficient” Dec. 2007, R4 MS-06-84-E.

Tao, L.N., and Donovan, W.F., 1955, “Through-Flow in Concentric and Eccentric Annuli of Fine Clearance With and Without Relative Motion of the Boundaries”, Transactions of the ASME, Vol 77, pp. 1291-1299.

White, F.M., 2006, *Fluid Mechanics*. McGraw-Hill.

Wright et al. (2009)

4 Air Data Experimental Verification

The objective of this chapter is to provide a summary of tests conducted to provide validation of the instrumentation and capability of the supporting equipment. The focus of the study was to quantify the expected performance of the facility and establish a baseline to compare with carbon dioxide.

A series of air data tests were conducted to provide validation of the test facility. Tests were conducted with both a standard knife-edge orifice as well as through an annular region simulating a shaft-seal interface. Air flow through an orifice is a well-documented phenomenon with available literature and was presented in great detail in Chapter 2. Flow through an annular region represents a more complex flow scenario for which there is very little data, but the ideas expressed in this chapter seem to represent the data well.

4.1 Data taken through a Circular Orifice

Measurements were obtained with air as the working fluid at different inlet pressures to ensure that the facility was properly calibrated. A knife-edge orifice was used in order to compare the measurements to available literature summarized in Linfield (2000) and Ward-Smith (1979) as well as the manufacturer's suggested flow coefficient C_v. The results are presented here in Figure 4.1 and Figure 4.2. Notice the larger uncertainty in the pressure ratio measurements for

Figure 4.1 compared to Figure 4.2 is due to the relatively lower pressures measured during testing; the pressure transducers were selected based on their full scale and impose a larger relative uncertainty on the measurements obtained when operating at lower pressures.

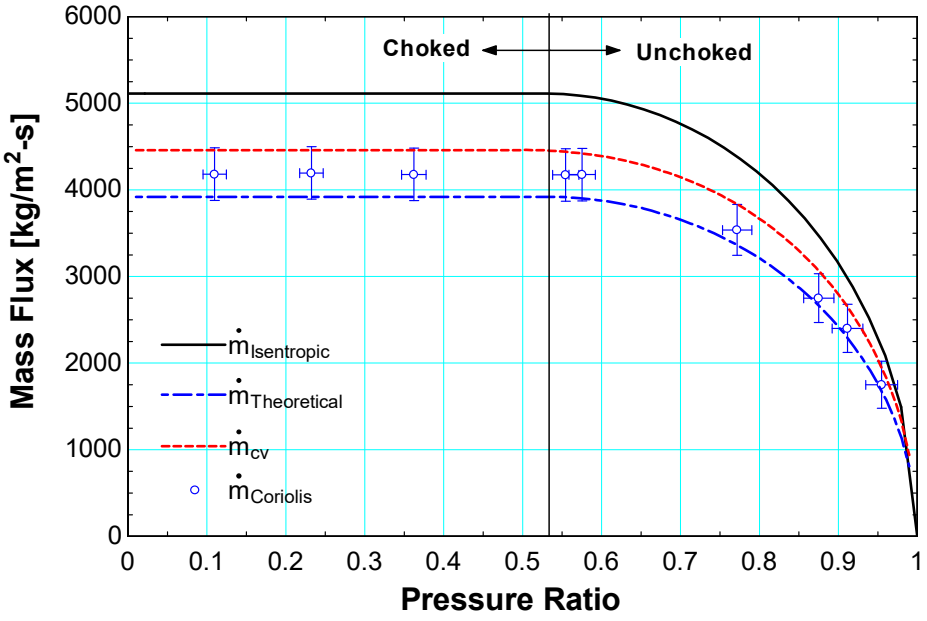

Figure 4.1 Measurements obtained with a knife-edge orifice at P_{inlet} = 2.068 MPa and ρ_{inlet} = 24 kg/m^3. Discharge coefficient evaluated at Cd = 0.84 for the data shown.

The measurements illustrated in Figure 4.1 were taken with air at an upstream pressure of 2.068 MPa. Inlet density variation was negligible as density is a weak function of temperature at these conditions. Three models are illustrated in the figure. The top black-line depicts the isentropic model with a discharge coefficient C_d set to unity and serves as an upper bound on the flow. The next line shown in red depicts the manufacturer's suggested flow coefficient for this particular

orifice; two values were quoted as illustrated in equation (4.1). The flow coefficient quoted for air was used to construct the red line in the figure.

$$\begin{aligned} Flow\big|_{air}^{\Delta P=40\ psi} &= 0.568\ scfm \rightarrow C_v\big|_{air} = 0.0170 \\ Flow\big|_{water}^{\Delta P=40\ psi} &= 0.114\ gpm \rightarrow C_v\big|_{water} = 0.0180 \end{aligned} \tag{4.1}$$

The final blue line represents the isentropic model modified with a discharge coefficient of C_d = 0.84 as was nominally chosen based on the data presented in Ward-Smith (1979). The models presented in Chapter 2 reported in Linfield (2000) suggest a similar scenario where equation (4.2) summarizes the data presented in Table 2-3.

$$C_d\big|_{choked} :\ 0.81 < C_d\big|_{choked} < 0.86 \tag{4.2}$$

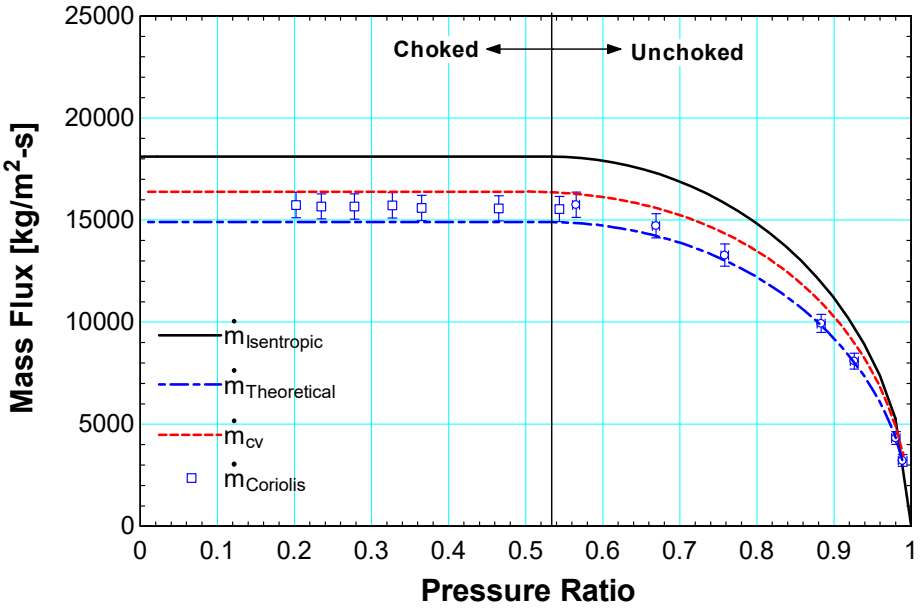

Figure 4.2 Measurements obtained with a knife-edge orifice at P_{inlet} = 7.67 MPa and ρ_{inlet} = 92 kg/m^3. Discharge coefficient evaluated at Cd = 0.84 for the data shown.

Figure 4.2 shows a similar trend to that developed in Figure 4.1 with the exception that the measurements shown were taken at test section pressures and are less susceptible to minor deviations in the pressure ratio. A summary of both figures is shown below in Figure 4.3 which illustrates the effect on the discharge coefficient as a function of pressure ratio for the measurements obtained with the facility.

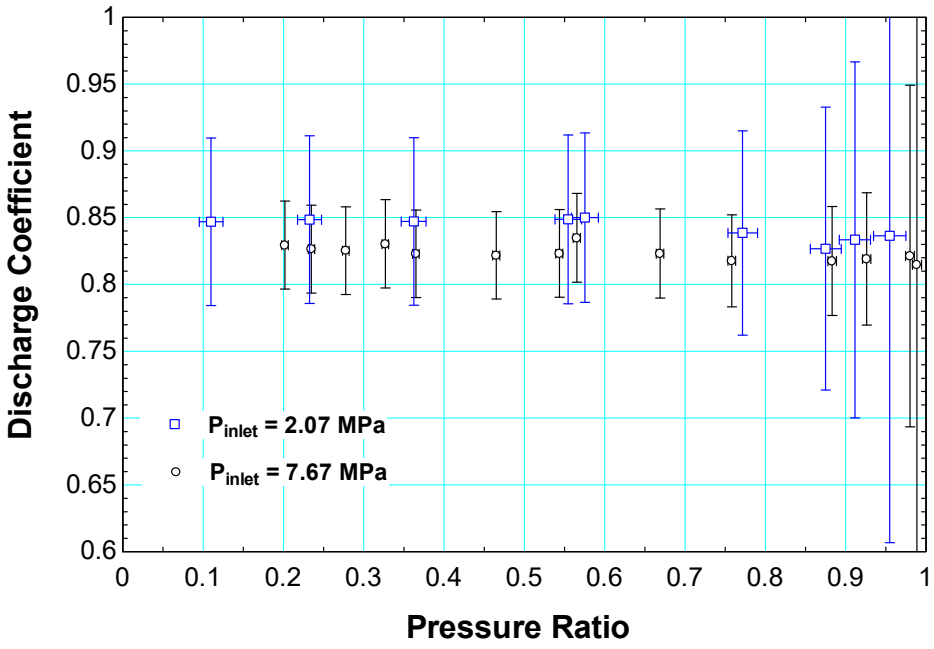

Figure 4.3 Discharge coefficient for measurements taken with an orifice at P_{inlet} = 2.07 MPa and P_{inlet} 7.67

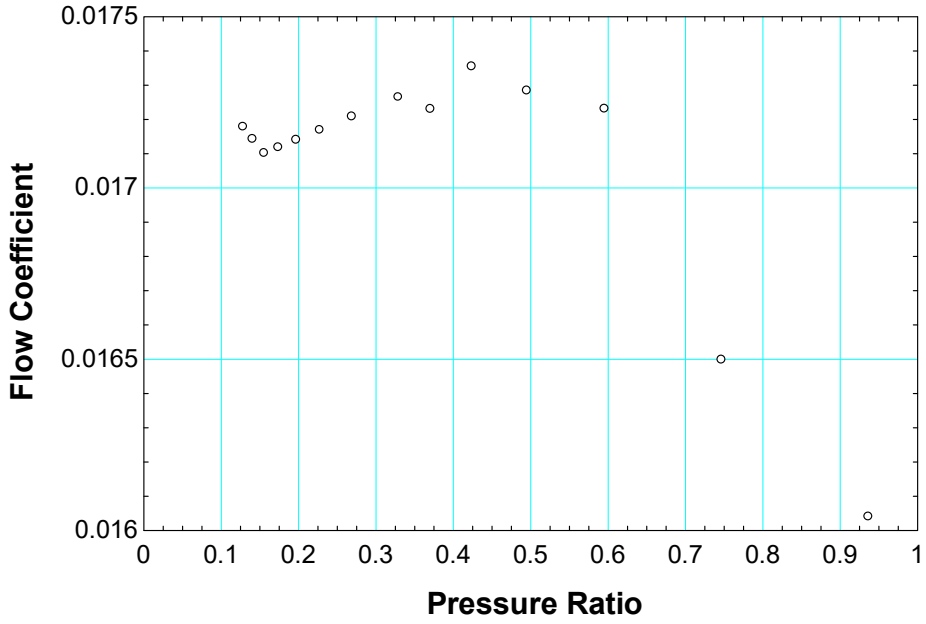

Figure 4.4 Manufacturer's Flow Coefficient Data – O'Keefe Controls Co. (www.okcc.com)

Data published on the O'Keefe's Controls Co. website was used to construct Figure 4.4. The figure shows that the actual flow coefficient varies with pressure ratio for pressure ratios greater than the critical pressure ratio. The flow coefficient then approaches a constant value of approximately $C_v \approx 0.01725$. This data was used to construct Figure 4.5 which shows that the discharge coefficient nominally approaches a fixed value of $C_d \approx 0.91$ for $PR < 0.6$. The other major piece of information which can be extracted from Figure 4.5 is that the discharge coefficient is particularly sensitive to even minor deviations in the available flow area at the conditions desired.

Commented [GFN1]: maybe refer the reader back to Chapter 3 where you talked about how the flow coefficient is defined

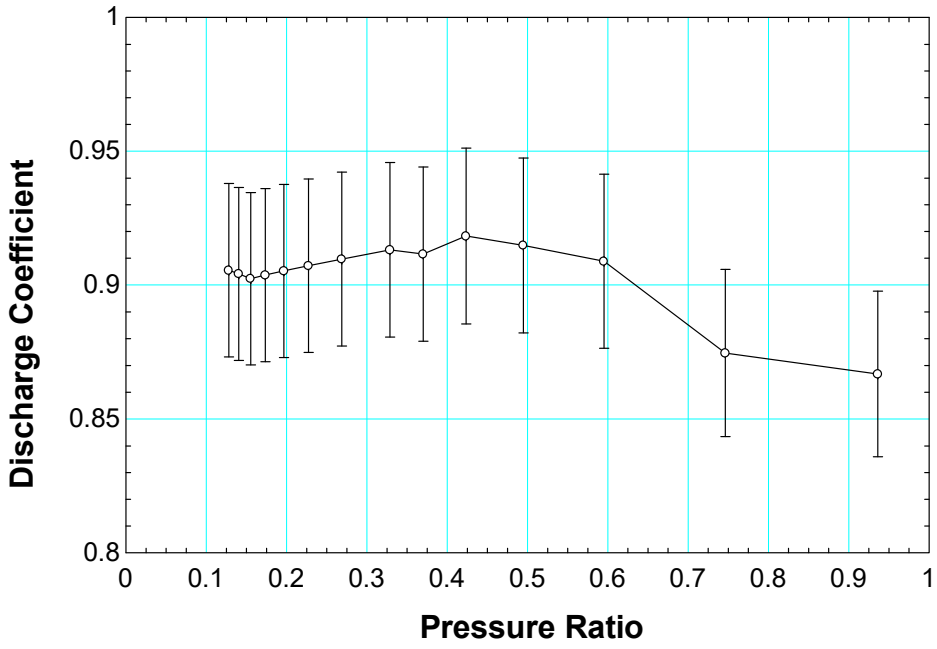

Figure 4.5 Manufacturer's Flow Coefficient Data expressed in terms of Discharge Coefficient

It is important to note that the uncertainty in Figure 4.5 was ~~constructed~~ estimated strictly based on the manufacturer's tolerance of the available flow area, as demonstrated below in Figure 4.6. In general, the discharge coefficient for an orifice is a function of the flow area, the upstream and downstream pressures, inlet temperature, and flow rate; the latter information was not published so the uncertainty represented in the discharge coefficient shown in Figure 4.5 should be considered a lower bound on the actual uncertainty. Nevertheless, the limited information obtained from the manufacturer does seem to match the data obtained with the facility.

Variable±Uncertainty	Partial derivative	% of uncertainty
Cdcheck = 0.9068±0.03239 [-]		
Deng = 0.028±0.0005 [in]	∂Cdcheck /∂ Deng = -64.78	100.00 %

Figure 4.6 Uncertainty in Discharge Coefficient strictly based on orifice diameter

4.2 Data taken through an Annular Orifice

Data taken through an annular orifice was more difficult to verify. Measurements were obtained with air as the working fluid at different inlet pressures. Essential geometrical information about this test series is summarized in Table 4-1. Measurements were compared to an empirical correlation of the incompressible discharge coefficient provided by Suryanarayanan (2009) who extended the work of Gamal et al. (2006, 2008). Two shafts were installed in the test facility for this test series. The results are presented in Figure 4.7 prove to be consistent with the validation correlation in the limit that the pressure ratio approaches 1 – i.e. the flow ~~is~~ approaches incompressible. This limiting condition is illustrated in Figure 4.9 and Figure 4.10. Eccentricity effects also appear to be limited in this test facility as the results are consistent with literature that assumes centered shafts.

Table 4-1 Geometrical parameters used in annular orifice test series

PARAMETER	VARIABLE	VALUE	UNCERTAINTY
SEAL			
Diameter	D_{seal}	3.1814 mm	±3.81 µm
Length	L_{seal}	7.62 mm	±2.54 µm
Max seal roughness	e_{seal}	0.305 µm	
SHAFT			
Diameter 1	D_{shaft}	3.1021 mm	±0.762 µm
Diameter 2	D_{shaft}	3.1123 mm	±0.762 µm
Length	L_{shaft}	50.8 mm	

Max shaft roughness	E_{shaft}	0.051 µm	

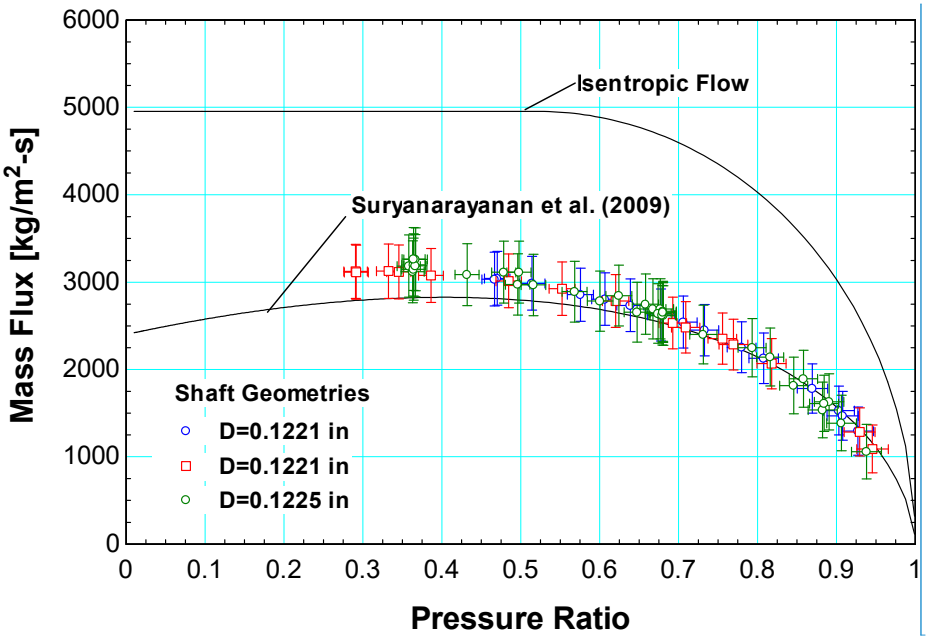

Figure 4.7 Measurements obtained through an annular orifice at P_{inlet} = 2.065 MPa and ρ_{inlet} = 24 kg/m^3. Mass flux is conserved as a function of pressure ratio for the geometry and working fluid conditions shown.

Commented [GFN2]: why doesn't mass flux vary with diameter?

The two shafts installed in the facility had a diametrical clearance of $D^1_{clear} = 79.3\,\mu m\,(0.00312\,in)$ and $D^2_{clear} = 69.1\,\mu m\,(0.00272\,in)$ respectively with the mass flow rates measured for the two cases differing by about 20% at lower pressure ratios. Again, the uncertainty of the Coriolis mass flow meter is $0.000015\frac{kg}{s}$ so the difference between the two mass flow rates should be significant enough for the flow meter to distinguish as demonstrated in equation (4.3).

$$\frac{\dot{m}_{0.1225}(PR \approx 0.5) - \dot{m}_{0.1221}(PR \approx 0.5)}{\dot{m}_{error}} = \frac{0.0012 - 0.001}{0.000015} = \frac{0.0002}{0.000015} = 13.3 \qquad (4.3)$$

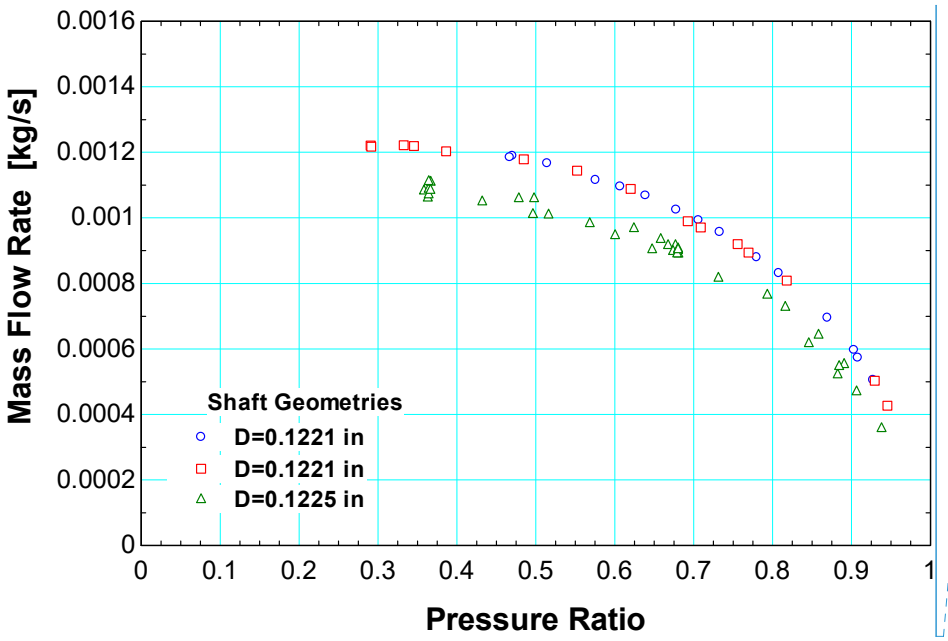

Commented [GFN3]: is this inconsistent with the previous figure?

Figure 4.8 Raw data of measurements obtained with test facility at P_{inlet} = 2.065 MPa and ρ_{inlet} = 24 kg/m^3. Offset in mass flow rate clearly apparent for 10 µm difference in shaft diameter.

Figure 4.9 and Figure 4.10 plot the discharge coefficient versus Reynolds number for the different geometrical inputs specified in Table 4-1. Figure 4.9 illustrates the output of the empirical correlation by Suryanarayanan (2009) as a function of the Reynolds numbers encountered in this test facility. A word of caution must be interjected regarding the output from the correlation provided by Suryanarayanan (2009). Suryanarayanan (2009) states a dependency

of his correlation of the variable $\frac{L}{c} = \frac{Length\,of\ seal}{Radial\,clearance}$. However, any and all attempts to plot the data obtained with this facility as a function of this parameter yielded unrealistic results. It is not clear if the author actually correlated the data from Gamal et al. (2008) as a function of $\frac{L}{D_h} = \frac{L}{2c} = \frac{Length\,of\ seal}{Hydraulic\,Diameter}$. However, if the correlation does applies to $\frac{L}{D_h}$ instead of $\frac{L}{c}$, the following information is applicable.

Suryanarayanan (2009) specifies that the correlation is applicable to flows with $\mathrm{Re}_{D_h} < 15000$ at pressure ratios $PR \to 1$ but it is demonstrated here that the critical Reynolds number is also sensitive to the ratio of the labyrinth tooth thickness to the hydraulic diameter of the annulus, $\frac{L}{D_h}$. Figure 4.9 and Figure 4.10 illustrate that the applicability of the correlation drops from about 80% to 67% of the critical Reynolds number identified by Suryanarayanan (2009) for $\frac{L}{D_h}$ equal to 96.2 and 110.3 respectively. Again, the correlation has been highly tuned to predict discharge coefficients for incompressible flow. Discharge coefficient predictions where the correlation loses applicability are circled in Figure 4.9 and Figure 4.10; in both cases, the correlation loses applicability for pressure ratios less than about $PR < 0.6$. This result was expected but it was also reassuring to verify that the facility was performing according to published trends in the limit that $PR \to 1$.

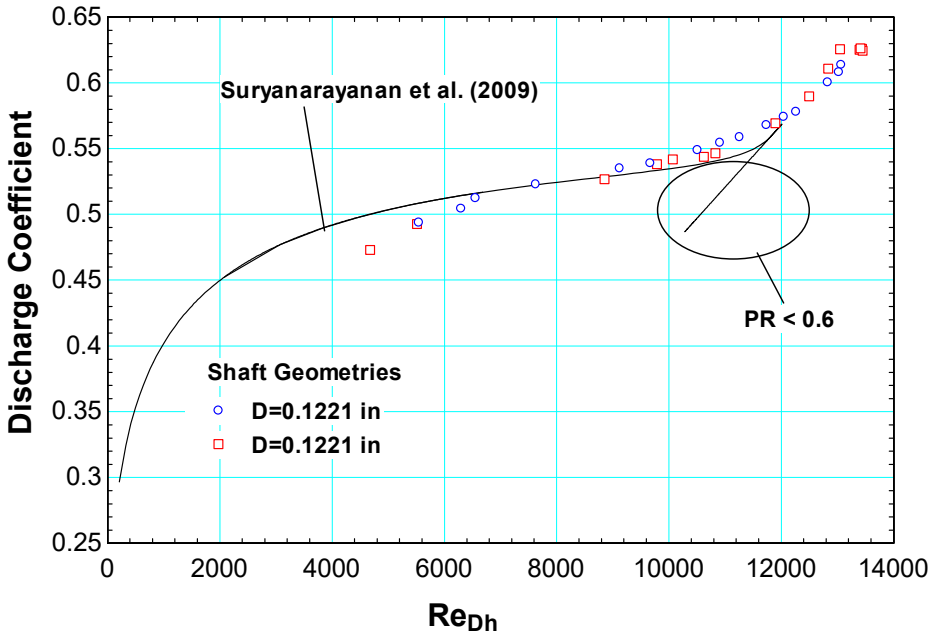

Figure 4.9 Discharge coefficient as a function of Re_D with compressibility effects included. Measurements demonstrated to deviate from empirical model at pressure ratios less than PR = 0.6 for length to hydraulic diameter ratios $L/D_h = 96.2$.

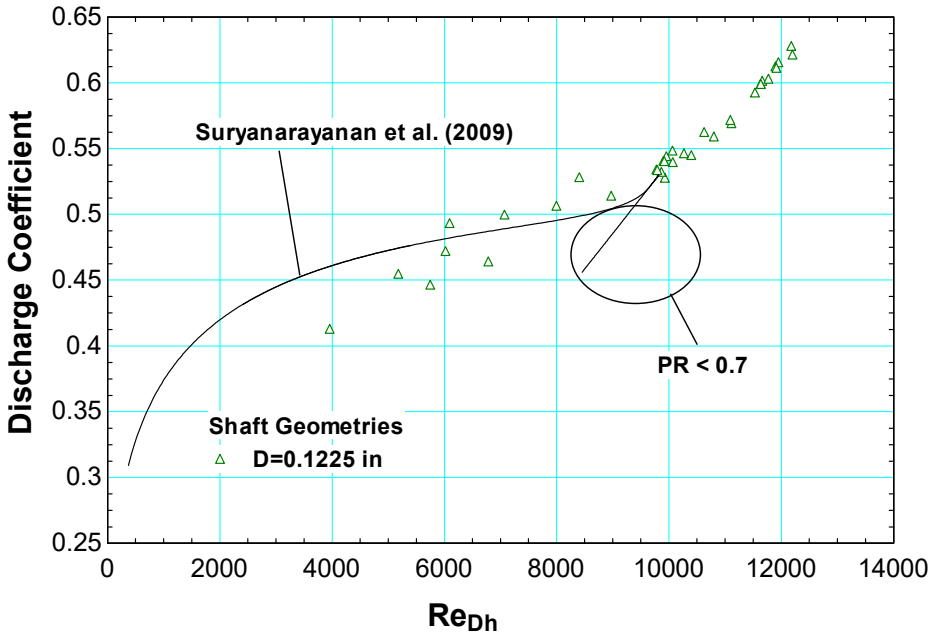

Figure 4.10 Discharge coefficient as a function of Re_D with compressibility effects included. Measurements demonstrated to deviate from empirical model at pressure ratios less than PR = 0.7 for length to hydraulic diameter ratios L/D_h = 110.3.

References

Gamal, A.M., Ertas, B.H., and Vance, J.M., High-pressure pocket damper seals: leakage rates and cavity pressures. Proceedings of GT2006 ASME Turbo Expo 2006: Power for Land, Sea, and Air, May 8-11, 2006, Barcelona, Spain.

Gamal, A.M., 2007, Ph.D. thesis. “Leakage and Rotordynamic Effects of Pocket Damper Seals and See-Through Labyrinth Seals”, Texas A&M University, College Station.

Linfield, K.W., 2000, Ph.D. thesis, “A Study of the Discharge Coefficient of Jets from Angled Slots and Conical Orifices”

O’Keefe’s Controls Co., 2000, www.okcc.com, 2 Oct, 2011.

Suryanarayanan, S., 2009, M.S. thesis, “Labyrinth Seal Leakage Equation”, Texas A&M University, College Station.

Ward-Smith, A.J., 1979, “Critical Flowmetering: The Characteristics of Cylindrical Nozzles with Sharp Upstream Edges”, Int. J. Heat & Fluid Flow, Vol. 1 No. 3 pp. 123-132.

5 Supercritical Carbon Dioxide Preliminary Results

This chapter presents data obtained with the test facility using carbon dioxide as the working fluid. The working fluid was regulated on both the inlet and outlet states during data collection in an effort to obtain comparative results.

The most difficult aspect of the project was controlling the inlet state. Fluid properties vary dramatically in the vicinity of the critical point and even minor deviations in temperature on the order of ±0.8°C can lead to unacceptable differences in density on the order of ±230 kg/m^3 as was demonstrated in Section 3.1 and illustrated in Figure 3.2.

5.1 Data taken through a Circular Orifice

Data was taken with the same orifice used to conduct the test series outlined in Chapter 4 where air was used as the working fluid. The data shown in that test series illustrated that the measurements taken were consistent with previous results as well as within the experimental uncertainty detailed in Chapter 3.

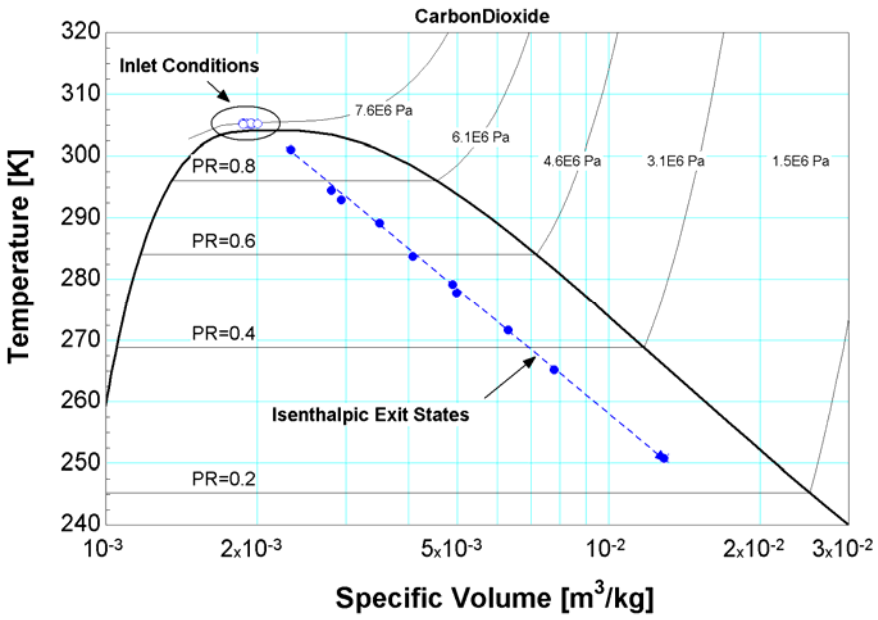

Figure 5.1 T-v diagram of data obtained with a sharp-lip orifice taken at P_{inlet}=7.6 MPa and ρ_{inlet} = 500 kg/m^3; isenthalpic reference points are provided to note the large pressure ratios achievable with the test facility.

Figure 5.1 shows a T-v diagram of a test series conducted at an inlet state of 7.6 MPa and 500 kg/m^3. For each measurement shown, the inlet state was fixed to within the capability of the facility while the exit pressure was continuously adjusted to different pressure ratios denoted in the figure as *PR*. The figure shows that the facility is capable of achieving pressure ratios of 0.3 to 0.9 relative to the 7.6 MPa inlet condition. In each case, the facility was allowed to reach steady state so that the inlet and exhaust pressures, inlet density, and mass flow rate stabilized over a period of about 20 seconds. The results were then time-averaged over that period to evaluate the mass flow rate at a given pressure ratio where the concept is demonstrated by equation (5.1).

$$\dot{m}_{coriolis} = f\left(\overline{P_{inlet}(t)}\Big|_{20s}, \overline{\rho_{inlet}(t)}\Big|_{20s}, \overline{P_{outlet}(t)}\Big|_{20s}, geometry\right) \tag{5.1}$$

Figure 5.2 provides a close up view of the inlet conditions of the data set illustrated in Figure 5.1. Figure 5.2 demonstrates the difficulty of maintaining an inlet condition in this region where density is a strong function of temperature along an isobar. Notice that the measurement uncertainty at test conditions is mostly due to the pressure transducers which have a relatively low uncertainty of about 0.075% with a full scale of 40 MPa. The density measurement has an uncertainty of about ±0.2 kg/m^3 and it was not possible to regulate the facility at this level of precision given that the temperature difference required would be on the order of ±0.0004°C.

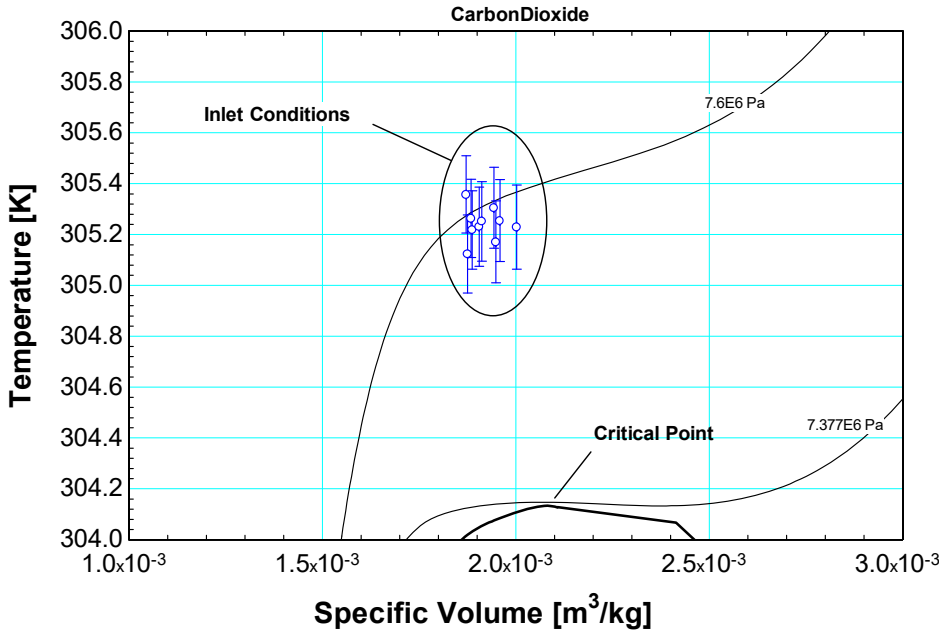

Figure 5.2 Measurement uncertainty of inlet conditions of data taken at P_{inlet}=7.58 MPa and ρ_{inlet} = 500 kg/m^3

Figure 5.3 demonstrates the extent of the problem outlined in Figure 5.2. Notice that if a Type-K thermocouple is used at these test conditions, the instrumentation error would account for a 46% error in inlet density and would render the data useless.

Variable±Uncertainty	Partial derivative	% of uncertainty
ρ = 500.8±230 [kg/m^3]		
P = 7.577E+06±30000 [Pa]	∂ρ/∂ P = 0.002664	12.07 %
T = 32.09±0.8 [C]	∂ρ/∂ T = -269.6	87.93 %

No unit problems were detected.

Figure 5.3 Measurement uncertainty using Type-K thermocouples facilitates the use of a coriolis flow meter at test conditions

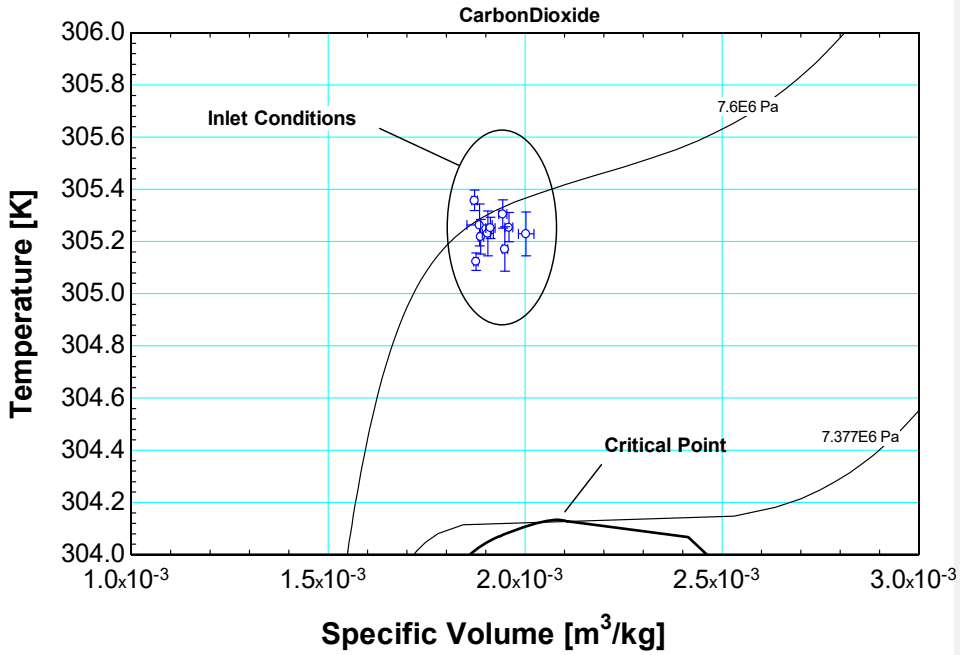

Figure 5.4 Standard deviation of measurements taken at P_{inlet}=7.58 MPa and ρ_{inlet} = 500 kg/m^3

Figure 5.4 shows the standard deviation in inlet thermodynamic state for each steady state point taken at these conditions. Notice that the temperature deviation shown on the y-axis is much smaller than the y-axis measurement uncertainty illustrated in Figure 5.2; this effectively shows that the inlet pressure was controlled to within the uncertainty of the pressure transducers. The pressure transducers were regulated to within ±25 kPa. Again, it was not possible to regulate the density within the uncertainty of the coriolis flow meter. At quasi-steady state, the density fluctuated about ±25 kg/m^3 from each nominal condition measured. This was considered acceptable based on the difficulty in obtaining these flow conditions and measurements.

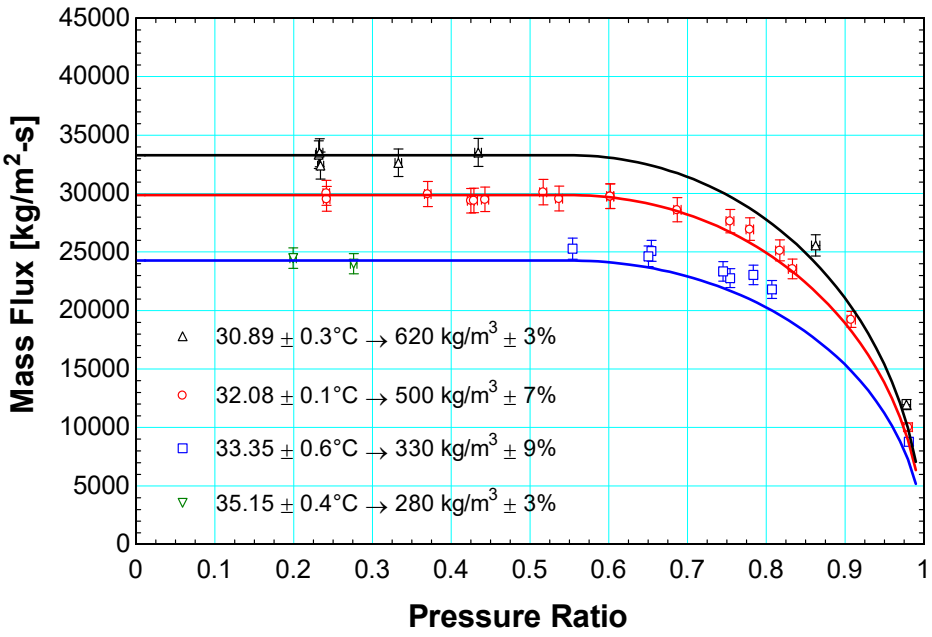

Figure 5.5 Mass flux versus pressure ratio for measurements taken at P_{inlet}=7.58 MPa and different inlet densities. Discharge coefficient of 0.75 fit to data.

Figure 5.5 shows the mass flux versus pressure ratio for data taken at an upstream pressure of 7.58 MPa and several inlet densities. A discharge coefficient of $C_d = 0.75$ was fit to the data for the measurements obtained using a modified version of the isentropic model from Chapter 2 shown here as equation (5.2). The density was held fixed to within 10% of the nominal value desired for all data illustrated in the graph. The data shown in red corresponding to 500 kg/m^3 is representative of the data elaborated upon in Figure 5.1, Figure 5.2 and Figure 5.4.

$$\frac{\dot{m}}{A_c} = C_d \sqrt{\frac{P_{in}\rho_{in}\left(\frac{2k_{ideal}}{k_{ideal}-1}\right)\left[(PR)^{\frac{2}{k_{ideal}}} - (PR)^{\frac{k_{ideal}+1}{k_{ideal}}}\right]}{1-\left\{(AR)^2 (PR)^{\frac{2}{k_{ideal}}}\right\}}} \qquad (5.2)$$

$$PR = \frac{\max(P_{out}, P_{crit})}{P_{in}};\ AR = \frac{A_{c,out}}{A_{c,in}};\ C_d\big|_{data-fit} = 0.75$$

The flow through an orifice is well studied and the general trends which apply in ideal gas flow seem to hold true for the present situation with the exception of the flow oscillations observed during testing. The large pressure gradients and relative location to the vapor dome dictate that the flow will cavitate through the restriction imposed by the orifice. Inside this restriction, the flow will separate into liquid and vapor components. The oscillatory motion with identifiable amplitude and frequency observed during testing is postulated to occur as a byproduct of a process where the liquid and vapor phases continuously exchange occupancy of the core of the flow.

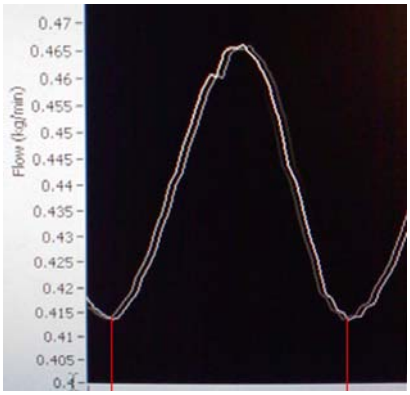

Figure 5.6 Oscillatory motion of the flow observed during testing

6 Conclusions and Future Work

This study was conducted to gain a better understanding of flow through seal geometry subject to supercritical inlet conditions and two-phase outlet conditions. An experimental test facility was constructed to quantify the mass flux of carbon dioxide near its critical point. Tests were executed with both orifices and rotor-stator configurations. A detailed uncertainty analysis was applied to the investigation to identify parameters which could be modified in the future to create a more effective sealing mechanism.

This preliminary investigation focuses on the development of the test facility constructed to aid in this study. A continuous system capable of cycling supercritical carbon dioxide was constructed at the University of Wisconsin – Madison. The system is expandable and supports multiple seal-shaft configurations.

6.1 Conclusions

6.1.1 Experimental Facility

The experimental test facility was designed to withstand system pressures as high as 14 MPa and produce pressure drops on the order of 12 MPa. The facility supports densities from 100 kg/m^3 to 1000 kg/m^3. The compressor is currently undersized for the experiment but is capable of continuous duty at about 7.6 MPa. The test section supports multiple seal configurations with limited uncertainty in the eccentricity.

The experimental facility was verified by comparing the measurements taken to the manufacturer's data as well as literature available from Ward-Smith (1979) and Linfield (2000).

6.1.2 Flow near the critical point through a knife-edge orifice

Test conducted with carbon dioxide at 7.58 MPa showed that the isentropic model of flow through an orifice provided a good baseline in capturing the physics of the flow. A knife-edge orifice was used for in this preliminary testing in order to avoid reattachment of the flow inside the orifice. The measurements obtained showed that the flow would choke at pressure ratios of about $PR = 0.6$. Measurements collapsed nicely in the unchoked region to the isentropic model when using a discharge coefficient of about $C_d = 0.75$ and an ideal gas specific heat ratio at the fluid temperatures provided $k = \frac{C_p\left(T_{inlet}\right)}{C_v\left(T_{inlet}\right)}$.

An oscillatory motion of the flow was observed to occur during testing when the downstream pressure was regulated inside the vapor dome. This phenomenon is believed to be cavitation driven with the two-phase separation occurring inside the very narrow opening. The oscillatory motion is not random but periodic with identifiable amplitude and frequency. One explanation which is offered to account for this unexpected result was presented in Chapter 5.

6.2 Future Work

The test facility is prone to appreciable leaking through the compressor and severely limits the amount of testing time at the large pressure drops desired. A new compressor is shown in Figure 6.1 and will be installed in the fall of 2010. The new compressor is a 40hp driven assembly capable of delivering 107 scfm at inlet pressures between 200-1500 psi and outlet pressures of 2400 psi as shown in the instruction manual – Hydro-Pac (2011).

The new compressor will allow larger more prototypical shaft geometries to be tested. The compressor also allows the speed to be regulated which will be incorporated into a PID control system implemented in LabView to compliment the current automated valve detailed in Section 3.5.

Figure 6.1 Hydro-Pac compressor to be installed Fall 2011

The other major design change will be to implement a recuperator in the system as detailed in Figure 6.2. The recuperator will provide the additional heating and cooling to allow the loop to operate at steady state with the larger compressor. Additional facility regulation will be accomplished by using the bypass valve shown at the top of the figure to divert the inlet flow into two streams according to the desired inlet density. Mixing will occur in the vicinity of thermocouple 4 labeled accordingly in the figure.

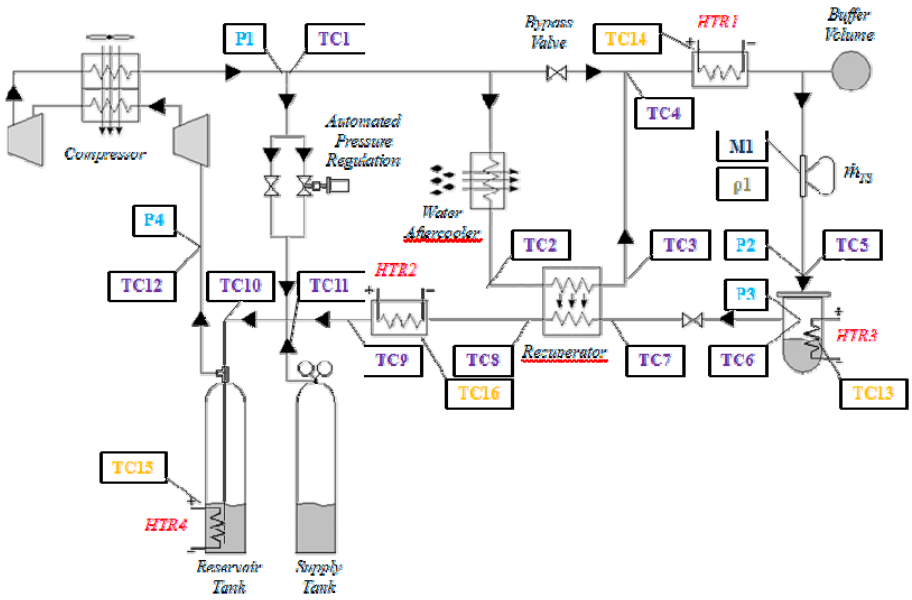

Figure 6.2 New test loop proposed to accommodate Hydro-pac compressor; the recuperator will provide the additional heating and cooling to make the facility operational.

Reference List

Hydropac (2011)

Appendix A: MATLAB Image Filtering Program

Image Input

```
I1=imread('mrodarte_shaft_LHS_1.tiff');   %reads image from graphics file
```

Image Processing

```
%   Preliminary historgram smoothing to enhance contrast
I1_adj=histeq(I1);              %histogram smoothing to enhance contrast

%   Special digital filtering
f1=fspecial('average');         %averaging convolution filter
cf=filter2(f1,I1_adj);          %applies 2-D digital averaging filter
cf2=double(I1_adj)-cf/1.5;      %highlights features in contrasted image

%   Subtracts zero-frequency components
af=fftshift(fft2(I1_adj));      %shifts zero-frequency components to center
[x,y]=meshgrid(-695:696,-519:520);  %creates 2-D mesh grid for filtering
z=sqrt(x.^2+y.^2);              %creates circular mesh z
c=(z>4);                        %creates circular filter
cfh=af.*c;                      %deletes frequency components
cfli1=ifft2(ifftshift(cfh));     %reconstructs image with deleted frequency

%   Adds frequency deleted image to averaged digitally filtered image
cfli2=(double(real(cfli1)))+(0.4*abs(double(cf)));

%   Applies digital averaging filter to processed image
cfli3=filter2(f1,cfli2);        %final processed image file
```

Image Outputs

```
figure,imshow(I1)               %original image
figure,imshow(I1_adj)           %histogram smoothed image
figure,imshow(cf2)              %averaged digital filter applied
figure,imshow(cfli1)            %zero-frequency components removed
figure,imshow(cfli2)            %addition of two image matrices
figure,imshow(cfli3)            %final image - digital averaging applied
```

Appendix B: Test Section Drawings

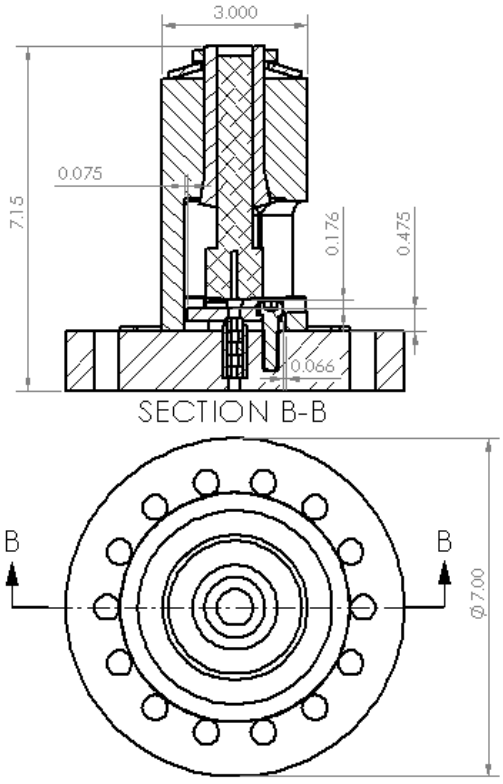

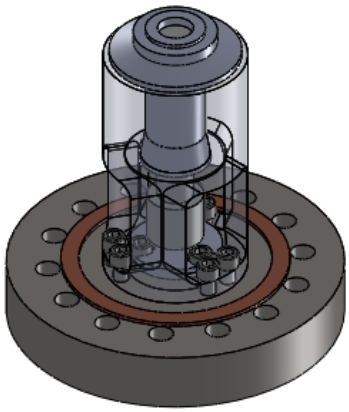

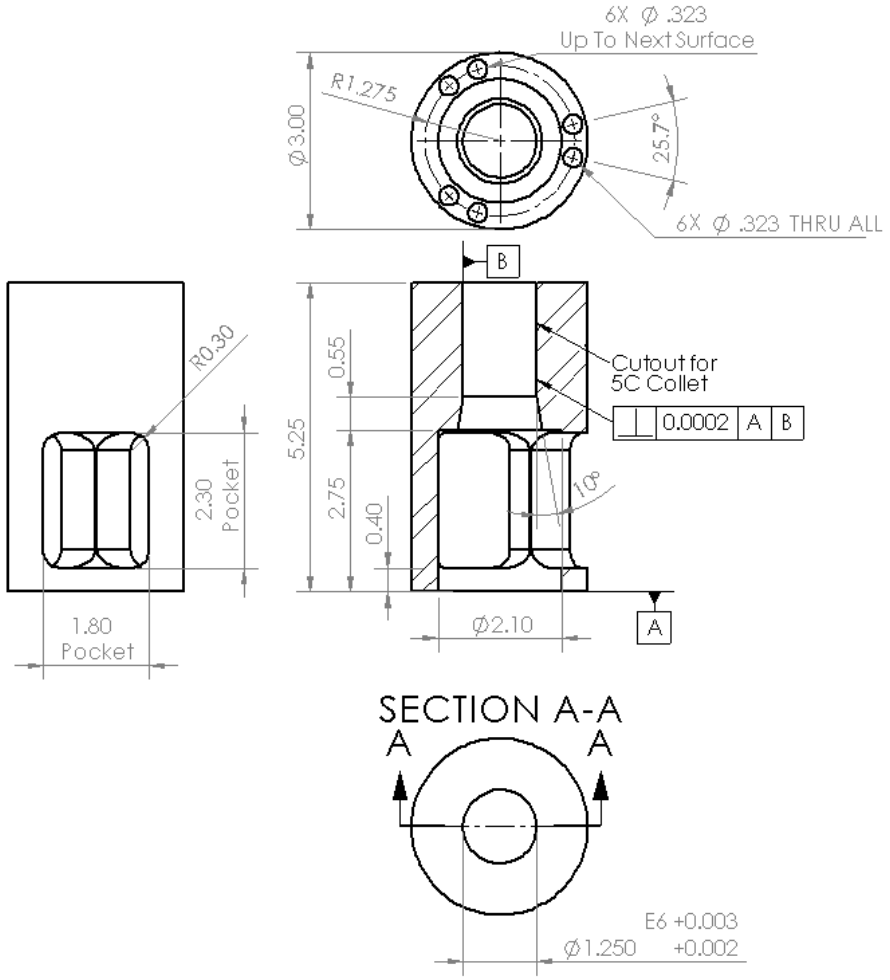
6X ⌀ .323
Up To Next Surface
R1.275
⌀3.00
25.7°
6X ⌀ .323 THRU ALL
B
R0.30
0.55
Cutout for
5C Collet
0.0002 A B
5.25
2.30
Pocket
2.75
0.40
10°
1.80
Pocket
⌀2.10
A
SECTION A-A
A A
E6 +0.003
⌀1.250 +0.002

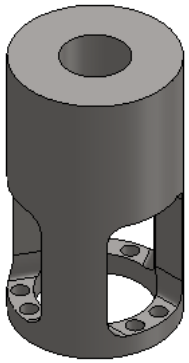

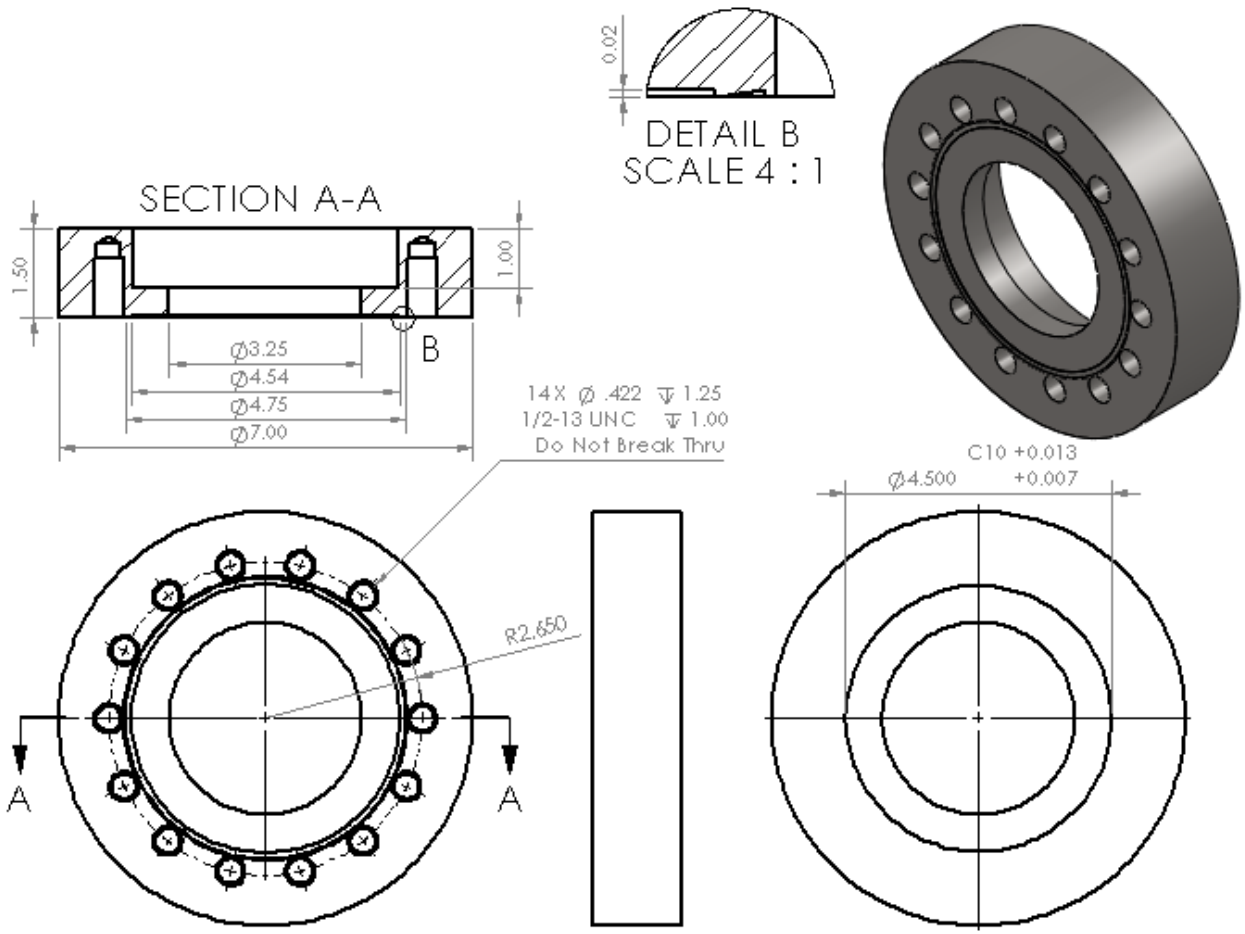
0.02
DETAIL B
SCALE 4 : 1
SECTION A-A
1.50
1.00
B
Ø3.25
Ø4.54
Ø4.75
Ø7.00
14 X Ø .422 ⩛ 1.25
1/2-13 UNC ⩛ 1.00
Do Not Break Thru
R2.650
A
A
C10 +0.013
Ø4.500 +0.007

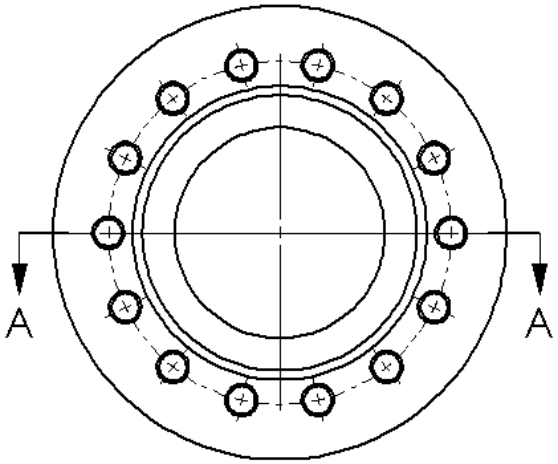

SECTION A-A

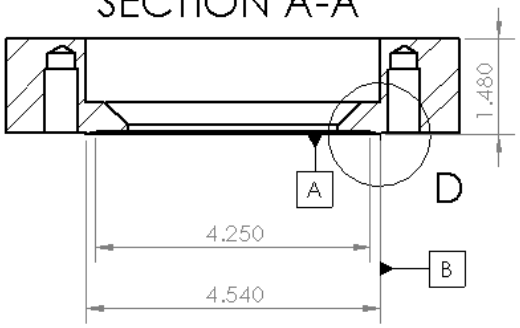

DETAIL D
SCALE 3 : 1

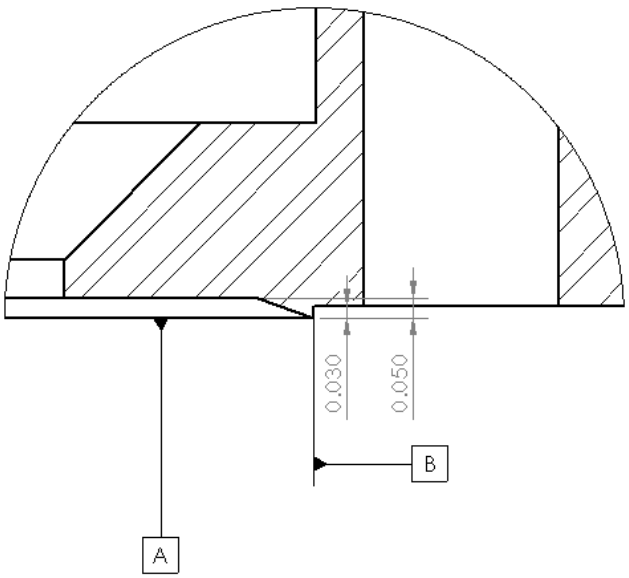

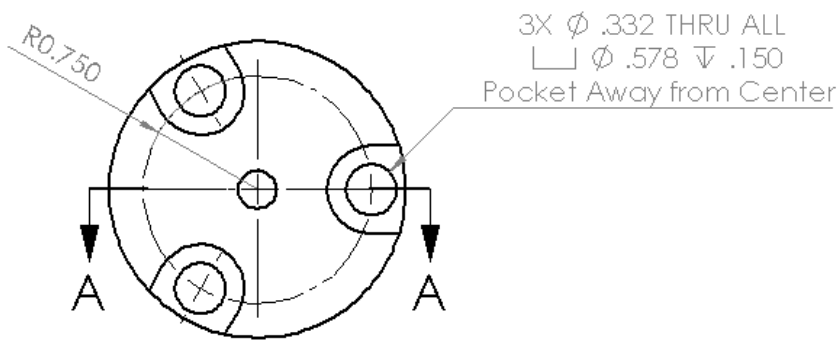
R0.750
3X ⌀ .332 THRU ALL
⌴ ⌀ .578 ↧ .150
Pocket Away from Center
A
A

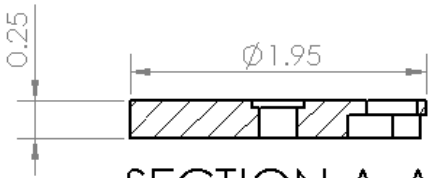
0.25
⌀1.95

SECTION A-A

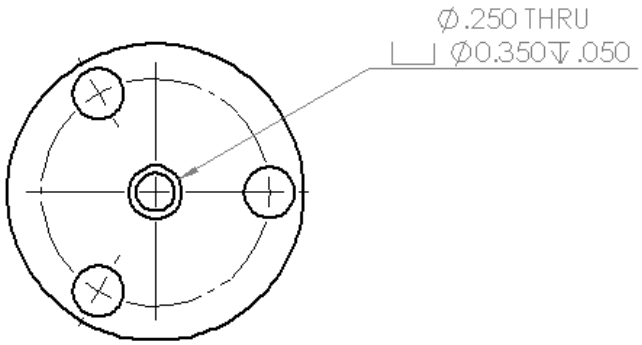
⌀.250 THRU
⌴ ⌀0.350↧.050

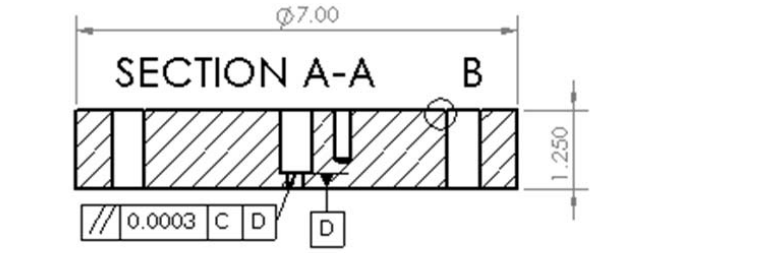

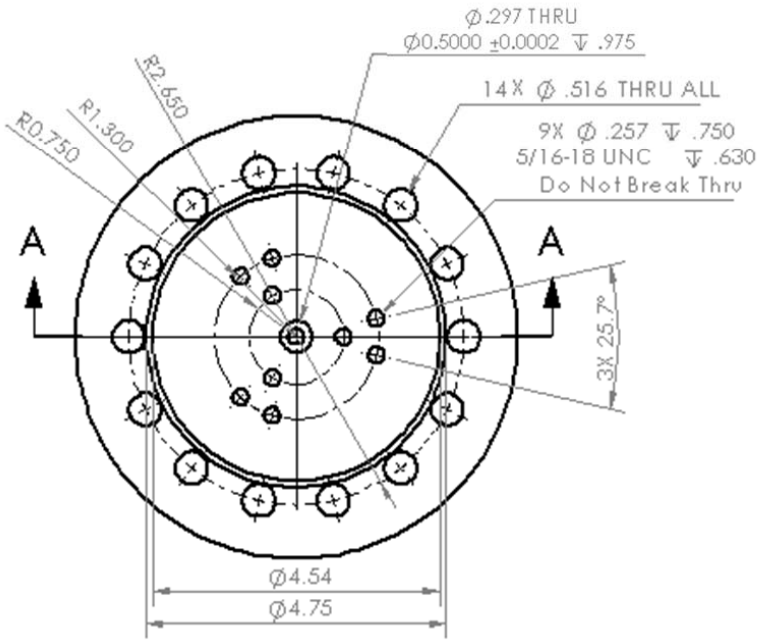

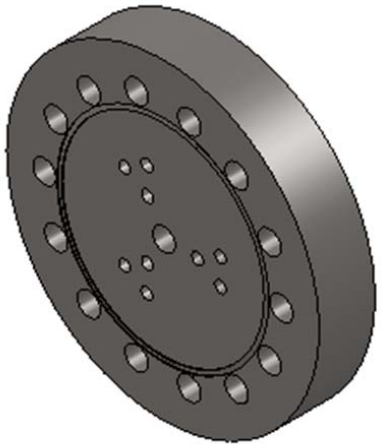

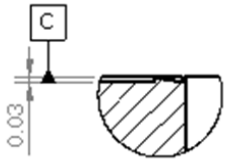

DETAIL B
SCALE 2 : 1

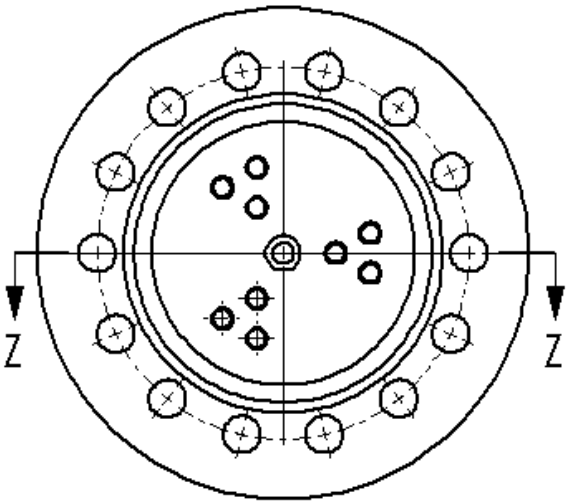

SECTION Z-Z

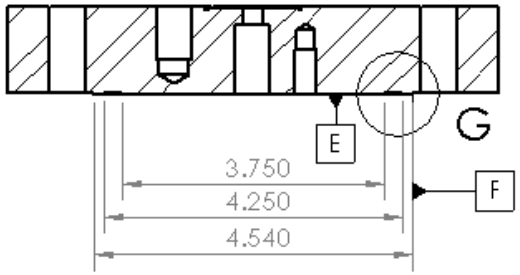

DETAIL G
SCALE 4 : 1

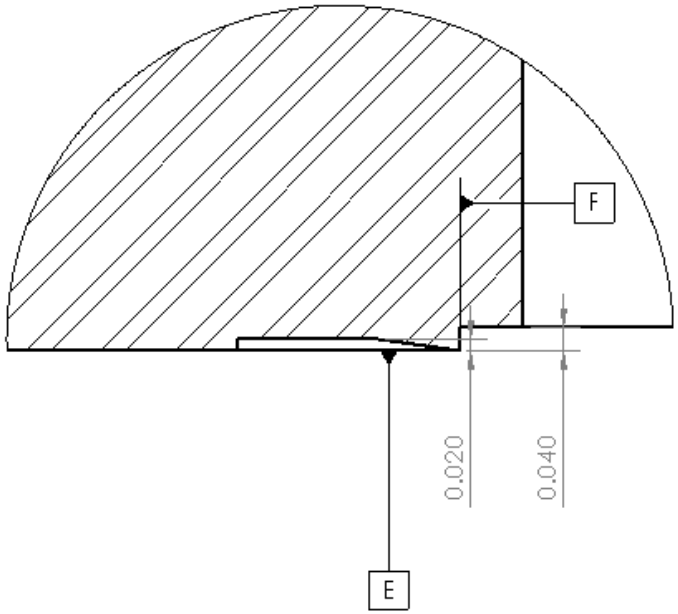

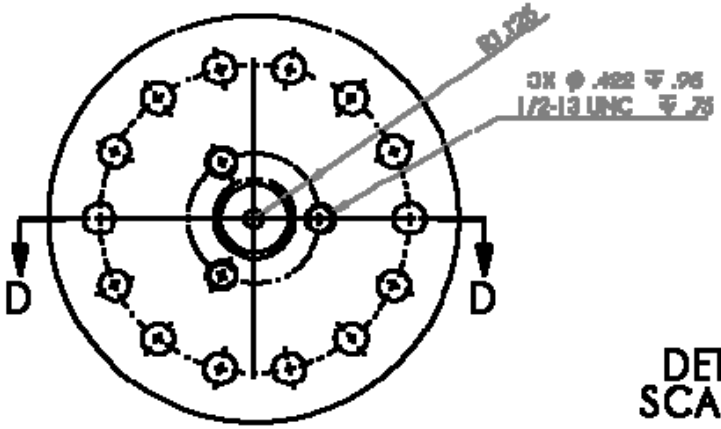

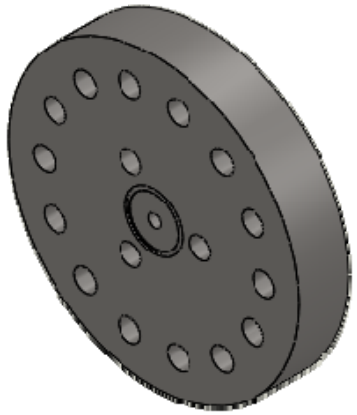

DETAIL K
SCALE 4 : 1

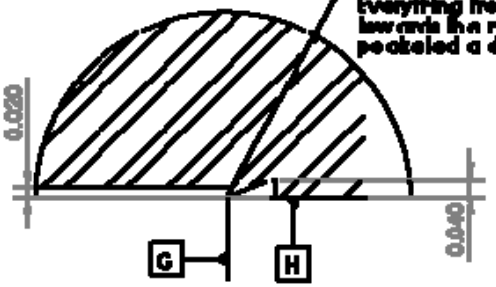

SECTION D-D

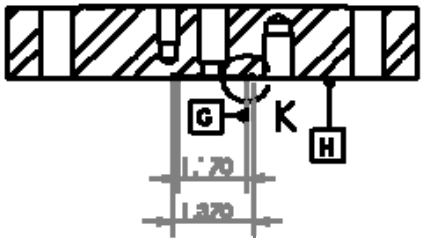

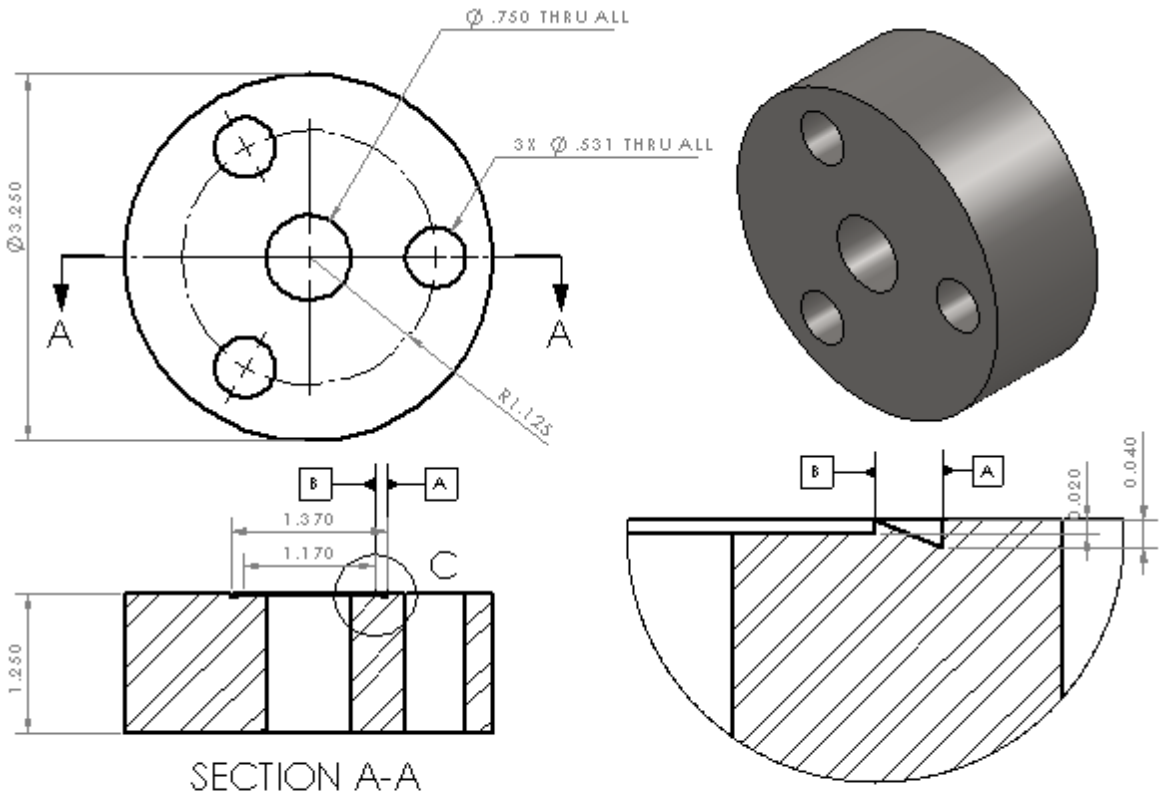
Ø .750 THRU ALL
3X Ø .531 THRU ALL
Ø3.250
A
A
R1.125
B
A
1.370
1.170
C
1.250
SECTION A-A
B
A
0.020
0.040
DETAIL C
SCALE 6 : 1

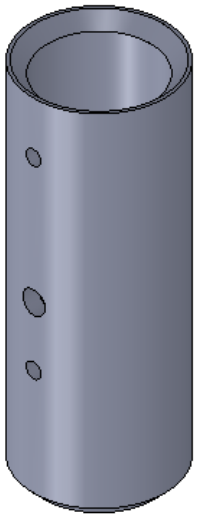

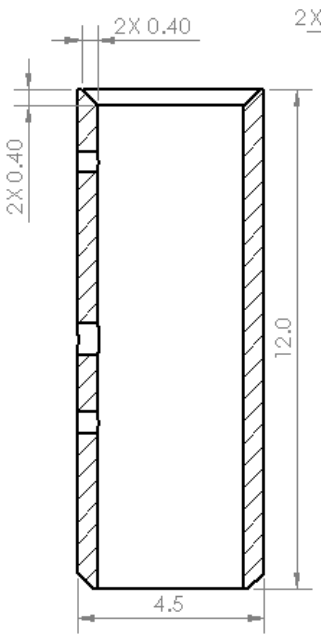
2X 0.40
2X 0.40
12.0
4.5

SECTION A-A

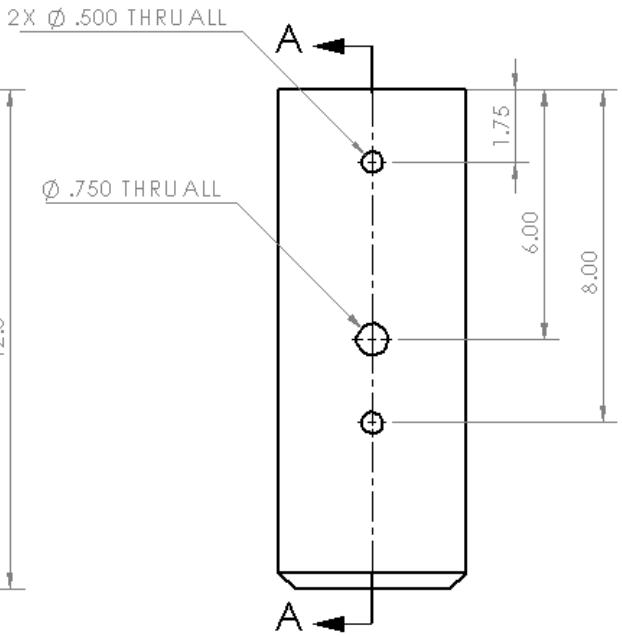
2X Ø .500 THRU ALL
A
Ø .750 THRU ALL
1.75
6.00
8.00
A

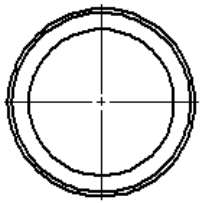

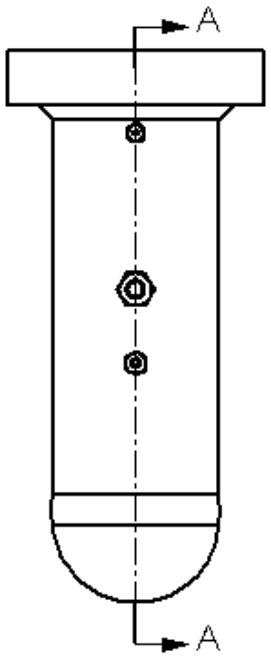

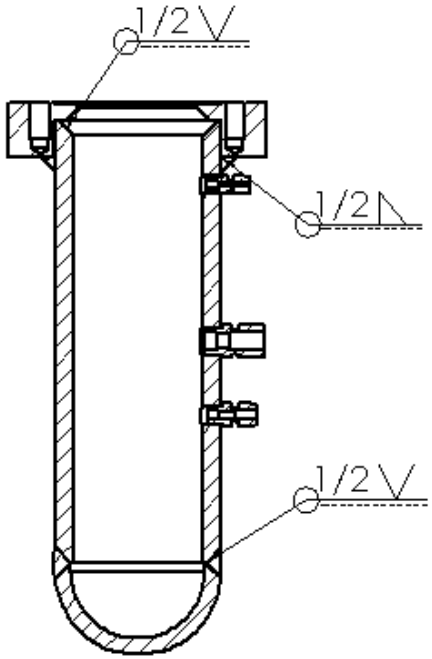

SECTION A-A